

**DEVELOPMENT OF RADIO FREQUENCY INTERFERENCE DETECTION  
ALGORITHMS FOR PASSIVE MICROWAVE REMOTE SENSING**

by

**Sidharth Misra**

**A dissertation submitted in partial fulfillment  
of the requirements for the degree of  
Doctor of Philosophy  
(Atmospheric and Space Sciences)  
in The University of Michigan  
2011**

Doctoral Committee:

Professor Christopher S. Ruf, Chair  
Professor Anthony W. England  
Professor Mahta Moghaddam  
Asst. Res. Scientist. Roger Dean De Roo  
Professor Niels Skou, Technical University of Denmark

**© Sidharth Misra**

---

**All rights reserved**

**2011**

**To  
My Family**

## Acknowledgement

I was fortunate enough to have a few very good mentors, who were patient enough to tolerate me and my questions. I would like to thank Prof. Ruf for not employing a judo *sankaku-jime* whenever I messed up, Roger De Roo for getting excited about some tiny theoretical problem that only the two of us really cared about, Steve Gross for pretty much building almost everything that this thesis is based on and Darren McKague for always being ready with a mop and a bucket to clean up after any of my professional breakdowns.

The main reason this thesis had any chance was due to an amazingly proficient support staff. I would like to thank Sandra Pytlinski for catering to my weirdest reimbursement questions, Linda Chadwick for being the sole reason I have a NASA fellowship in the first place, Bryan White for fixing all of my IT related stuff immediately when I'd run into his office panicking and then putting in a ticket for me afterwards, Margaret Reid for fixing all of my departmental related panic sessions and Marti Moon for her Monday morning baked goodies.

My lab-mates had to suffer me for years, and I them. I would like to thank Boon for being a curmudgeonly and bitter old lab-mate that everyone aspired to be, Jinzheng for being the politest Chinese assassin around, John Puckett for always telling me to "*Man up princess!!*", Amanda for being my best recruit and a protégé molded after myself – only better, Rachael for being the happiest robot anyone has seen – cheerfully besting me

in every single game we've played, Shannon for being a one person sitcom mixed in with a soap-opera and Dave for bouncing the red ball.

Then there is this medley of friends to thank, without whom I probably would've gotten this thesis finished faster, but it wouldn't have been as much fun. I would like to thank Catherine for listening to me whine and complain for the past 2 and a half years and refraining from punching me in the face, Rahul for being ready with the most inappropriate comments whenever needed, Awlok for dripping with sarcasm whenever I needed a boost, Johri for blaming me every time anything went wrong, Babu for conjuring up grand plans that failed every time, Sharath for being 'Commander', Raj for being my co-producer on many yet to be made blockbuster hits, Andy for being there whenever I wanted to make fun of Indiana, Tzeno for laughing every time he saw my face and Kim for being awesome. I would also like to thank my AOSS graduate student friends like Ahmed for being the only other student to get excited by soil moisture, Kevin for Being A Michigan Fan, Dan for all the hugs, Paul for always being five moves ahead, Jacob for the best steaks and burgers, Kristen for all the cake balls, Matt for being *baby crusher*.

Then there are those friends who are far away but had something to do with me starting this thesis, like Sumit who used little scientific facts I gave him as successful pick up lines, Abhikesh and Arun for joining me in giving the Nirma Profs a hard time, John Peter Boncori Merryman for his amazing chapter 4, Sara for understanding my movie references, Cecilia and Enrica for doing their best to listen to me when I spoke Gibberish.

Finally, I would like to thank my family. I would like to thank my sister-in-law for getting more excited about my papers and conferences than I was, my Dad for always asking me when I will get a real job, my brother for coming up with ridiculously complicated math problems when I was in school and enjoy watching me squirm when trying to solve them, and my Mom for being the one reason I ever decided to pay attention in school and pursue a Ph.D.

## Table of Contents

Dedication.....	ii
Acknowledgement .....	iii
List of Figures.....	ix
List of Appendices .....	xvi
Glossary of Variables and Constants .....	xvii
Abstract.....	xviii
Chapter 1 Introduction .....	1
1.1 Planck’s Law and Earth.....	1
1.2 Microwave Remote Sensing.....	5
1.3 Nature of thermal emissions and interference.....	12
1.3.1 Statistical nature of thermal emissions .....	12
1.3.2 Man-made interference .....	13
1.4 Detection and Mitigation algorithms.....	17
1.5 Structure of thesis.....	21
1.6 Personal Contributions .....	24
Chapter 2 Detection of Radio-Frequency Interference for the Aquarius Radiometer ....	32
2.1 Introduction .....	32
2.2 RFI Detection Algorithm .....	34
2.3 Ground Truth and FAR .....	37
2.4 Performance of the algorithm.....	42
2.5 Summary and Discussion .....	48
Chapter 3 Microwave radiometer Radio Frequency Interference detection algorithms: A comparative study .....	52
3.1 Introduction .....	52
3.2 RFI Detection Algorithms.....	54
3.2.1 Kurtosis Detection Algorithm.....	54

3.2.2	Pulse Detection Algorithm.....	58
3.3	Performance Comparison of RFI Detection Algorithms.....	59
3.3.1	RFI Model and Area Under Curve (AUC) parameter .....	59
3.3.2	Comparison with pulse detection algorithm under optimum resolution.....	65
3.3.3	Algorithm comparison under varying RFI conditions .....	69
3.4	Summary and Discussion .....	72
Chapter 4 An Improved Radio Frequency Interference model: Reevaluation of the		
kurtosis detection algorithm performance under central limit conditions .....		
4.1	Introduction .....	76
4.2	Kurtosis Algorithm and Issues .....	77
4.3	Multiple Source RFI model.....	78
4.3.1	Probability distribution of Gaussian noise plus multiple pulsed-sinusoidal waveforms .....	82
4.4	Kurtosis Performance .....	85
4.5	Experimental verification.....	88
4.6	Conclusion.....	92
Chapter 5 Analysis of Radio Frequency Interference Detection Algorithms in the		
Angular Domain for SMOS .....		
5.1	Introduction .....	93
5.2	SMOS RFI Detection Domains.....	94
5.2.1	Visibilities Domain .....	95
5.2.2	Spatial Domain.....	96
5.2.3	Angular Domain.....	97
5.3	Domain Comparison .....	101
5.3.1	Visibility Domain versus Spatial Domain .....	101
5.3.2	Angular Domain versus Spatial Domain .....	106
5.4	Angular Domain Results .....	109
5.4.1	RFI Detection.....	109
5.4.2	False-Alarm Sensitivity .....	112
5.4.3	Negatively Biased RFI.....	114
5.4.4	RFI snapshot .....	115
5.4.5	Algorithm Performance .....	117

5.5	Summary and Discussion.....	118
Chapter 6	Conclusions .....	122
6.1	Brief Review .....	122
6.2	Contributions.....	123
6.3	Future Work .....	125
6.3.1	Optimal RFI detection algorithm.....	125
6.3.2	SMOS Angular domain algorithm improvement.....	127
6.3.3	SMOS RFI second-order effects.....	128
6.3.4	Alternative RFI detection techniques.....	128
6.3.5	On-board RFI processing.....	130
6.3.6	Aquarius RFI detection algorithm parameter determination .....	131
Appendices	.....	133
References	.....	153

## List of Figures

Fig. 1.1: Black-body radiance of the Sun at 5800K. The peak wavelength is around 450-500nm, which is in the middle of the visible spectrum. ....	2
Fig. 1.2: Black-body radiance of the Earth at an effective physical temperature of 255K. The peak wavelength is around 10 $\mu$ m, which is in the infrared (IR) spectrum.....	3
Fig. 1.3: Solar irradiance curve for a 50cm-1 spectral interval at the top of the atmosphere and at the surface for a solar zenith angle of 60 <sup>o</sup> in an atmosphere without aerosols or clouds. ( <i>courtesy [4]</i> ).....	4
Fig. 1.4: Theoretical Planck radiance curves for a number of the earth's atmospheric temperatures as a function of wavenumber. Also shown is a thermal infrared emission spectrum observed from the Nimbus 4 satellite indicating radiance at the top of the atmosphere. ( <i>courtesy [4]</i> ).....	5
Fig. 1.5: Depiction of various upwelling radiance components of microwave remote sensing measurements at TOA.....	7
Fig. 1.6: Percentage transmission through the earth's atmosphere, along the vertical direction, under clear sky conditions. ( <i>courtesy [7]</i> ).....	10
Fig. 1.7: Examples of pre-detection signals. On the left are time-domain representations of the signals, and their pdfs are shown on the right. The top plot represents Gaussian distributed geophysical signals/receiver noise and the bottom plot represents a sinusoid, a presumed typical non-Gaussian RFI noise. ( <i>courtesy [31]</i> ).....	14
Fig. 1.8 Venn diagram illustrating five separate RFI detection principles and their possible combinations for implementation purposes. ....	19

Fig. 1.9: Flowchart of dissertation topic .....	22
Fig. 2.1: FAR of the kurtosis detection algorithm for various thresholds calculated from normally distributed simulated data (dashed line) and RFI-free PALS-ADD data sample (solid line) .....	39
Fig. 2.2: Effect of mean-threshold magnitude, $T_m$ on the FAR of the second moment detection algorithm for the detection-threshold magnitude, $T_{det}$ values (from upper right to lower left): $T_{det} = 2.5, 2.8, 3.1, 3.4, 3.7, 4.0$ .....	41
Fig. 2.3: Effect of detection-threshold magnitude, $T_{det}$ on the FAR of the second moment detection algorithm for the mean-threshold magnitude, $T_m$ values (from upper right to lower left): $T_m = 0.5, 0.8, 1.1, 1.4, 1.7, 2.0, 2.3$ .....	42
Fig. 2.4: RFI detection of PALS-ADD L-Band radiometer measurements of nadir sky view with strong RFI present: (top) 2 <sup>nd</sup> moment time series; (center) kurtosis of signal; (bottom) Aquarius RFI detection algorithm. ....	44
Fig. 2.5: PALS-ADD L-Band radiometer measurements during transition from nadir sky view to BB absorber. (top) 2 <sup>nd</sup> moment time series; (center) kurtosis of signal; (bottom) Aquarius RFI detection algorithm .....	45
Fig. 2.6: Similar to Fig. 2.5 but with a single RFI event artificially added at the point of maximum time-rate-of-change of $T_b$ during simulated coastal crossing. (top) 2 <sup>nd</sup> moment time series; (center) kurtosis of signal; (bottom) Aquarius RFI detection algorithm. ....	46
Fig. 2.7: PALS-ADD L-Band radiometer measurements of nadir sky view with BB absorber placed in front of the antenna for a while. (top) 2 <sup>nd</sup> moment time series; (center) kurtosis of signal; (bottom) Aquarius RFI detection algorithm .....	47
Fig. 3.1: Images of 6.0 GHz horizontally polarized brightness temperature (top) and kurtosis (bottom) during an overpass of the Gulf coast near Galveston, TX. The bottom plot of kurtosis has a blue coastal map added over it showing the insensitivity of kurtosis to brightness temperature changes. ....	58

Fig. 3.2: Plot of the ROC curves for three RFI detection schemes (Pulse-detection algorithm, Fullband kurtosis detection algorithm, Sub-sampled kurtosis algorithm) for a 0.33% duty-cycle pulsed-sinusoid RFI with a 0.5 NE $\Delta$ T power level. .... 64

Fig. 3.3: (a) Plot comparing the ROC area for the kurtosis algorithm as a function of relative data rate and number of sub-bands with the matched pulse detection algorithm (star) (b) Magnified plot indicating ROC area of the kurtosis algorithm near matched pulsed detection algorithm (star) (RFI power = 0.5NE $\Delta$ T). The relative data rate is with respect to the ideally matched pulse detector. Heavy blue lines represent data rate and ROC area values for the matched pulse detector. .... 66

Fig. 3.4: Same as Fig. 3.3 except (RFI power = 1.5NE $\Delta$ T)..... 69

Fig. 3.5: Plot indicating difference between AUC of the pulse detection algorithm and kurtosis detection algorithm (16 sub-bands and 4 sub-sampling periods) for different RFI pulse widths and duty cycles (Blank areas indicate detection performance of both algorithms is poor, yellow to red areas indicate better performance by the kurtosis detection algorithm and light blue to dark blue areas indicate better performance by the pulse detection algorithm and green areas indicate similar performance by both algorithms) ..... 70

Fig. 3.6: Same as Fig. 3.5 except that the kurtosis detection algorithm has 16 sub-bands and 2 sub-sampling period..... 71

Fig. 4.1: Brightness temperature values over (a) New York – 10ms samples and (b) Central Europe – 8ms samples (*courtesy N.Skou*) indicating RFI (blue-unmitigated Tb, red-RFI mitigated Tb using full-band kurtosis) ..... 78

Fig. 4.2: Exponential pdf applied for amplitude of individual RFI sources, the mean of the exponential pdf is a scalable parameter based on required output power. The above plot has a mean of 1V. .... 80

Fig. 4.3: Bimodal pdf applied for duty-cycle of individual RFI sources, the fraction of low duty-cycle to high duty-cycle is a variable parameter with the above plot indicating 50% of sources with low duty-cycle..... 82

Fig. 4.4: Probability density function of RFI with thermal noise, blue curve represents a single RFI source and purple curve represents multiple sources (50% sources, 100% low duty-cycle) ..... 84

Fig. 4.5: Mean value of kurtosis as a function of number of sources and fraction of low duty-cycle sources. The overall power remains the same as the number of sources increases. (Orange  $\rightarrow$  Kurtosis = 3)..... 86

Fig. 4.6: Mean value of kurtosis vs. RFI power (in NE $\Delta$ T) for 200 sources (Region between black dashed lines – Undetectable RFI by kurtosis or oversampled pulse detect, Red rectangle – Undetectable problematic RFI)..... 87

Fig. 4.7: Block-diagram of Multi-source RFI experimental setup..... 88

Fig. 4.8: Experimental results indicating excess kurtosis versus excess RFI  $T_b$ s in Kelvin (scaled assuming RFI-free thermal emission of 300K). The dashed lines represent the  $\pm 4 * NE\Delta K$  of kurtosis. The colors represent any RFI corruption due to different numbers of sources. (Legend: Red=1src, Cyan=3srcs, Purple=5srcs, Green=7srcs, Blue=9srcs, Black=11srcs) ..... 90

Fig. 4.9: Curves indicating kurtosis variation versus the number of RFI sources for different power levels. The solid lines represent mean kurtosis calculated from experimental data, the dashed curve is fit from the experimental data at 1350K antenna  $T_b$  with a 300K background. .... 91

Fig. 5.1: SMOS semi-orbit map indicating the number of multiple measurements made at a single grid-location over various incidence angles ..... 99

Fig. 5.2: Illustration of (a) Sinusoidal wave in time domain (b) Gaussian noise in time domain (c) combined signals in time domain, representing an indistinguishable noisy sinusoidal wave, and (d) combined signals in frequency domain, with clear peaks distinguishable from the noise floor. .... 102

Fig. 5.3: Two SMOS snapshots contaminated by single point source RFIs (a) RFI  $T_b$  = 1500K (b) RFI  $T_b$  = 150K ..... 105

Fig. 5.4: Correlation statistics between an angular domain sample and its neighboring pixels based on two SMOS half-orbits. The blue-curve represents correlation between a sample under test at 25° incidence angle and the red-curve represents a sample under test at 35° incidence angle. The dashed line represents land statistics and solid line represents sea statistics..... 107

Fig. 5.5: Correlation statistics between a spatial domain sample and its neighboring pixels based on two SMOS half-orbits. The dashed line represents land statistics and solid line represents sea statistics. .... 108

Fig. 5.6: (a) SMOS H-pol Tb snapshot with a clear RFI spot at 450K (bright red) (b) Angular domain representation of the same RFI pixel with flagged RFI Tbs (red), RFI-free Tbs (blue) and cubic fit (green). The circled sample in (b) is the same pixel as the red hot spot in (a) ..... 110

Fig. 5.7: (a) SMOS H-pol Tb snapshot with an indistinct RFI spot within the circle (b) Angular domain representation of the same RFI pixel with flagged RFI Tb (red), RFI-free Tbs (blue) and cubic fit (green). .... 111

Fig. 5.8: (a) SMOS H-pol Tb snapshot with a low Tb lake surrounded by high Tb land; (b) Angular domain representation of the same lake pixel with flagged RFI Tbs (red), RFI-free Tbs (blue) and cubic fit (green)..... 113

Fig. 5.9: (a) SMOS H-pol Tb snapshot with a negatively biased RFI region (circle) (b) Angular domain representation of one of the pixels in cold RFI region with flagged RFI Tbs (red), RFI-free Tbs (blue) and cubic fit (green). .... 114

Fig. 5.10: (a) SMOS H-pol Tb snapshot over the eastern United States at 10:50:36 UTC on 8<sup>th</sup> July, 2010 (b) SMOS RFI snapshot at the same time over eastern United States. (red = RFI present, green = RFI free) ..... 116

Fig. 5.11: Histogram of Tb values over a single half orbit, sweeping from the south to north pole between 17°W and 95°W approximately, measured on 8<sup>th</sup> July, 2010 from 10:10 to 11:05 UTC. (Blue = All Tb data, Green = RFI free Tb data, Red = RFI corrupted Tb data)..... 117

Fig. 5.12: Determinant of a covariance matrix with elements of the row represented as a Gaussian distribution with the mean around the diagonal matrix element.....	121
Fig. 6.1: Simplified Block diagram indicating implementation of a digital lag correlator .....	130
Fig. I.1: CCDF of brightness temperature contribution of all types of RFI detected using the kurtosis and peak detection algorithms.....	138
Fig. I.2: CCDF of brightness temperature contribution of continuous wave RFI detected using the kurtosis detection algorithm .....	138
Fig. I.3: CCDF of brightness temperature contribution of pulsed type RFI detected using the kurtosis detection algorithm.....	139
Fig. I.4: CCDF of brightness temperature contribution of blind RFI, i.e. RFI detected using the peak detection algorithm but not detected by Kurtosis .....	140
Fig. I.5: CCDF of residual RFI detected using only the peak detection algorithm .....	141
Fig. I.6: CCDF of detected and residual types of RFI brightness temperature contribution for a 11min integration period .....	142
Fig. II.1: Plot indicating change in kurtosis as a function of the RFI magnitude for pulsed-sinusoid interference with a 0.01% duty cycle. The dashed line indicates the kurtosis $3\sigma$ detection threshold.....	146
Fig. II.2: Frequency scheme of IEEE 802.15.4 communication standard [86] .....	147
Fig. II.3: (a) Normalized histogram of the signal received by ADD for a clean sample (solid line), RFI corrupted sample with power $S_1$ (dash-cross) and RFI corrupted sample with power $S_2$ (dashed) ( $S_1 > S_2$ ) (b) Histogram tail (zoomed) showing “bump” of RFI corrupted sample.....	149

Fig. II.4: Plot indicating change in kurtosis as a function of the RFI magnitude for spread spectrum interference. The dashed line indicates the kurtosis  $3\sigma$  detection threshold.. 150

Fig. II.5: Kurtosis values when the spread spectrum signal is offset in frequency from the center of sub-band 4 of ADD. The straight line represents the kurtosis detection threshold..... 151

## **List of Appendices**

Appendix I Characterization of L-band RFI across the continental USA using a kurtosis detector.....	133
Appendix II Detectability of Radio Frequency Interference due to Spread Spectrum Communication Signals using the Kurtosis Algorithm .....	144

## Glossary of Variables and Constants

$\lambda$	Wavelength	cm
$f$	Frequency	Hz
$T$	Temperature	K
$\varepsilon$	Emissivity	-
$B_f$	Spectral radiance at frequency $f$	W/ m <sup>2</sup> .sr.Hz
$B_\lambda$	Spectral radiance at wavelength $\lambda$	W/ m <sup>2</sup> .sr.cm
$A_r$	Effective antenna aperture	m <sup>2</sup>
$B$	Bandwidth	Hz
$Tb$	Brightness temperature	K
$\alpha$	Attenuation constant	Np m <sup>-1</sup>
$\theta$	Incidence angle of nadir	deg
$R$	Reflectivity	-
$r$	Fresnel reflection coefficient	-
$e$	Dielectric constant	-
$\sigma$	Standard deviation of distribution	-
$\mu$	Mean of distribution	-
$\tau$	Radiometric integration time	sec
$W_s$	Window size	-
$W_r$	Window range	-
$T_{det}$	Detection threshold magnitude	-
$T_m$	Mean threshold magnitude	-
$m_n$	$n$ th central moment	-
$\kappa$	Kurtosis ratio	-
$A$	Amplitude of pulsed-sinusoidal wave	-
$\lambda_{nc}$	Chi-squared non-centrality parameter	-
$w$	Pulse width	sec
$t_0$	Center time of on pulse	sec
$\phi$	Phase shift	deg
$\nu$	Mean of exponential distribution	-
$p$	Fraction of low duty cycle	-
$b_w$	Mode of Rayleigh distribution	-
$d$	Duty cycle	-
$\sigma_{MSE}$	Fit error	K
$c_i$	Fit coefficients	K/deg <sup>i</sup>
$\sigma_\kappa$	Standard deviation of kurtosis	-
$h=6.626e-13$	Planck's constant	Jsec
$k=1.3806e-23$	Boltzmann's constant	J/K
$c=3e8$	Speed of light	m/s

## **Abstract**

Radio Frequency Interference (RFI) signals are man-made sources that are increasingly plaguing passive microwave remote sensing measurements. RFI is of insidious nature, with some signals low power enough to go undetected but large enough to impact science measurements and their results. With the launch of the European Space Agency (ESA) Soil Moisture and Ocean Salinity (SMOS) satellite in November 2009 and the upcoming launches of the new NASA sea-surface salinity measuring Aquarius mission in June 2011 and soil-moisture measuring Soil Moisture Active Passive (SMAP) mission around 2015, active steps are being taken to detect and mitigate RFI at L-band.

An RFI detection algorithm was designed for the Aquarius mission. The algorithm performance was analyzed using kurtosis based RFI ground-truth. The algorithm has been developed with several adjustable parameters to control the detection statistics (false-alarm rate and probability of detection). The parameters are allowed to be location dependant to adjust the algorithm based on amount of RFI expected.

The kurtosis statistical detection algorithm has been compared with the Aquarius pulse detection method based on the detection of pulsed-sinusoidal type RFI. The comparative study determines the feasibility of the kurtosis detector for the SMAP radiometer, as a primary RFI detection algorithm in terms of detectability and data bandwidth. The kurtosis algorithm has superior detection capabilities for low duty-cycle radar like pulses, which are more prevalent according to analysis of field campaign data. The kurtosis

algorithm can also detect spread-spectrum type communication signals, although at a somewhat reduced sensitivity.

Most RFI algorithms developed have generally been optimized for performance with individual pulsed-sinusoidal RFI sources. A new RFI detection model is developed as a result of observations of anomalous behavior by the kurtosis detection algorithm during an RFI flight campaign. The new model takes into account multiple RFI sources within an antenna footprint. The performance of the kurtosis detection algorithm under such central-limit conditions is evaluated.

The SMOS mission has a unique hardware system, and conventional RFI detection techniques cannot be directly applied. Instead, an RFI detection algorithm for SMOS is developed and applied in the angular domain. This algorithm compares brightness temperature values at various incidence angles for a particular grid location. This algorithm is compared and contrasted with other algorithms in the visibility domain of SMOS, as well as the spatial domain. Initial results indicate that the SMOS RFI detection algorithm in the angular domain has a higher sensitivity and lower false-alarm rate than algorithms developed in the other two domains.

# Chapter 1

## Introduction

### 1.1 Planck's Law and Earth

Planck's blackbody radiation law forms the fundamental basis for the science of passive remote sensing. A blackbody, as defined by [1], is a material which has the property of allowing incident rays at all frequencies to be absorbed without surface reflection. The blackbody also acts as a perfect emitter to maintain thermal equilibrium based on Kirchhoff's law [2]. The Planck equation describes the spectral radiance emitted by such an idealized body at a certain wavelength and physical temperature in thermodynamic equilibrium.

Planck's equation, which describes the spectral brightness radiated by a blackbody at frequency  $f$  (or wavelength  $\lambda$ ) and absolute temperature  $T$  uniformly in all directions, is given by

$$B_f(T) = \frac{2hf^3}{c^2 \left( e^{hf/kT} - 1 \right)} \frac{\text{W}}{\text{m}^2 \cdot \text{sr} \cdot \text{Hz}}$$
$$B_\lambda(T) = \frac{2hc^2}{\lambda^5 \left( e^{hc/k\lambda T} - 1 \right)} \frac{\text{Wm}^{-2}}{\text{m}^2 \cdot \text{sr} \cdot \text{cm}} \quad (1.1)$$

where  $h=6.626\text{e-}13$  J-s is Planck's constant,  $k=1.3806\text{e-}23$  J/K is Boltzmann's constant and  $c=3\text{e}8\text{m/s}$  is the speed of light. The two separate equations shown above represent

Planck's curve (or energy flux per unit steradian) measured in terms of unit frequency or unit wavelength. The unit area underneath both curves represents equal amount of energy flux. A perfect blackbody has an electromagnetic emission spectrum that is a function of its physical temperature, as shown by Fig. 1.1. The figure indicates the radiance at 5800K, the physical surface temperature of the sun. As noted by the relative intensities at each wavelength, the sun emits most in the visible wavelength region.

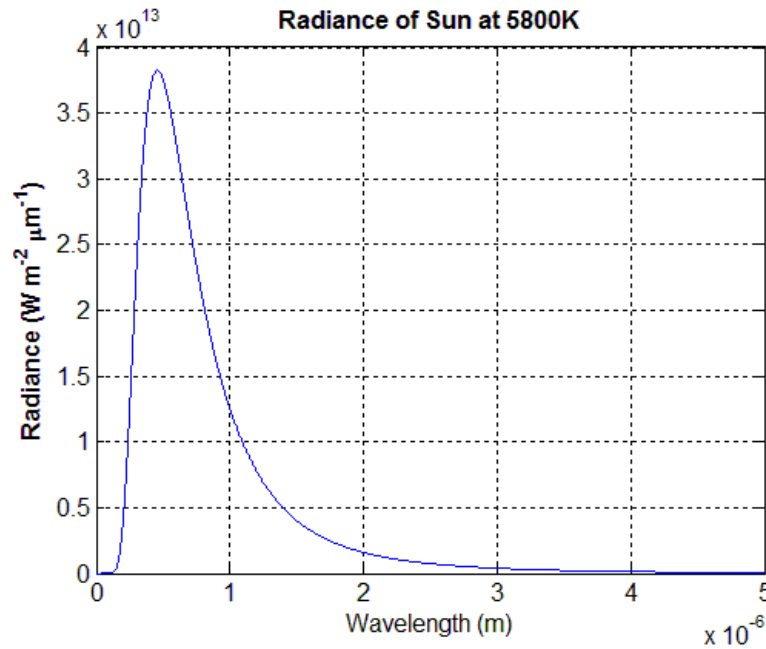


Fig. 1.1: Black-body radiance of the Sun at 5800K. The peak wavelength is around 450-500nm, which is in the middle of the visible spectrum.

Similarly, the Earth has an effective physical temperature of 255K [3], which would mean that most of its electromagnetic emission is in the infra-red region as shown by the Fig. 1.2. The Earth itself however does not behave like a blackbody at all wavelengths. At certain wavelengths the Earth behaves as a greybody, where it emits (and absorbs) less than an idealized perfect absorber/emitter blackbody.

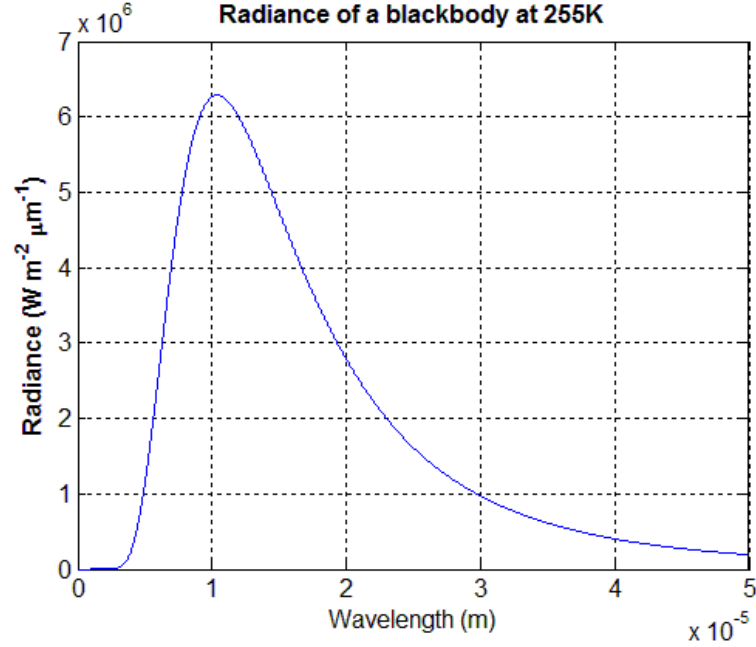


Fig. 1.2: Black-body radiance of the Earth at an effective physical temperature of 255K. The peak wavelength is around 10μm, which is in the infrared (IR) spectrum.

The greybody emits less than a blackbody and also has directional preferences for radiation and reflection. The greybody is defined by its emissivity, which is the ratio of greybody’s radiation to that of a blackbody at the same physical temperature. A greybody has an emissivity that is less than 1.

$$\varepsilon(\theta, \varphi, \lambda, T, p) = \frac{B_e(\theta, \varphi, \lambda, T, p)}{B_{bb}(\theta, \varphi, \lambda, T, p)} \quad (1.2)$$

where  $B_e$  represents the emitting intensity of the body,  $B_{bb}$  is Planck’s brightness function for a blackbody,  $\lambda$  is the emitting wavelength,  $T$  is the physical temperature of the body,  $p$  represents the wave polarization and  $\theta, \phi$  indicate the elevation and azimuthal directions of emission. A blackbody emits all the radiation it absorbs; the maximum emissivity possible is 1. The Earth is not a perfect black body. The actual solar irradiance spectrum at the top of Earth’s atmosphere is shown and compared to irradiance

at the surface of the Earth in Fig. 1.3. These window regions and opaque regions are due to the fact that various constituents in the Earth's atmosphere and surface (shown in the figure) have different absorption/emission properties at different wavelengths. Fig. 1.4 shows similar properties of the atmosphere by comparing the Earth's radiance at the top of the atmosphere with ideal Planck radiance curves. Remote sensing takes advantage of these properties to retrieve different geophysical parameters of the atmosphere or surface.

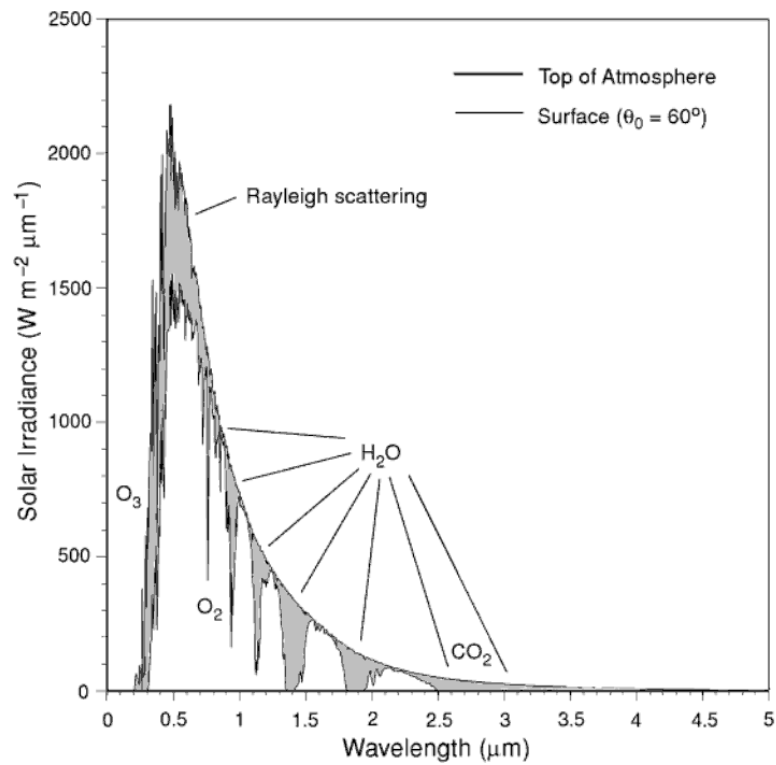


Fig. 1.3: Solar irradiance curve for a 50cm-1 spectral interval at the top of the atmosphere and at the surface for a solar zenith angle of 60° in an atmosphere without aerosols or clouds. (courtesy [4])

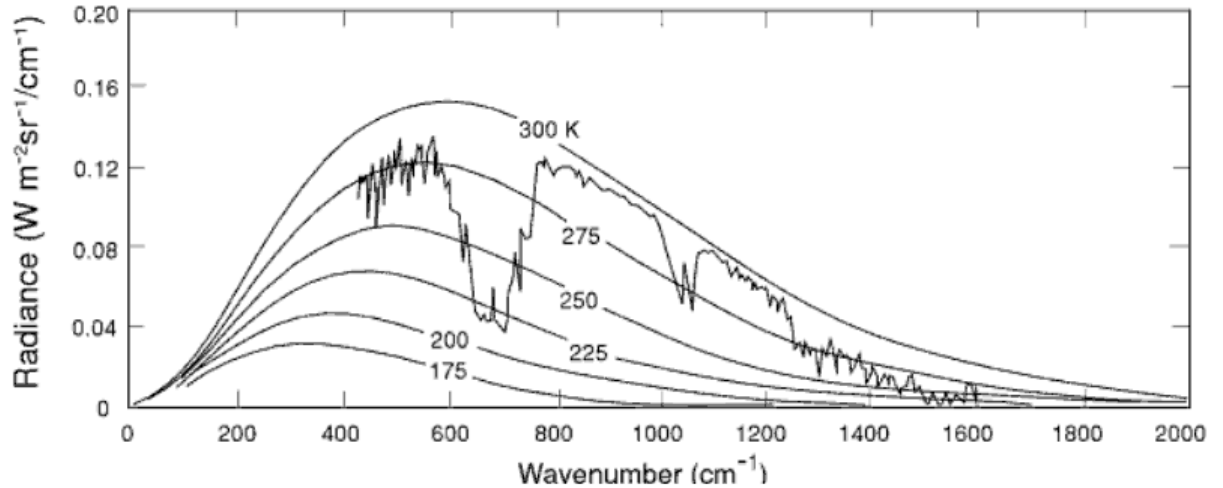


Fig. 1.4: Theoretical Planck radiance curves for a number of the earth's atmospheric temperatures as a function of wavenumber. Also shown is a thermal infrared emission spectrum (observed from the Nimbus 4 satellite indicating radiance at the top of the atmosphere. (courtesy [4])

## 1.2 Microwave Remote Sensing

The Rayleigh-Jeans law, though derived before Planck's equation was introduced by [5-6], serves as a good approximation to describe radiance in the microwave range (<300GHz). Planck's equation (1.1) reduces down to a simpler form, as shown below, when considering frequencies that satisfy the relation  $hf/kT \ll 1$ .

$$B_f = \frac{2f^2 kT}{c^2} = \frac{2kT}{\lambda^2} \quad (1.3)$$

In this frequency regime, there exists a linear relationship between brightness and temperature. The Rayleigh-Jeans approximation at 300K has a 1% error for 117GHz and 3% error for 300GHz, with respect to Planck's law [7].

For a narrow bandwidth  $B$ , if such emission were measured from an antenna within a black-body chamber (that absorbs everything and reflects nothing within) then [7-8] have

shown that the received power does not depend on the pattern of the antenna. Consider an antenna with a pattern described by  $F(\theta, \phi)$  in a black-body chamber at temperature  $T$ . Black-body emission within the chamber is essentially unpolarized, i.e. there is no correlation between the different directional components of the signal. A particular component of the power received by the antenna over some bandwidth can be described by,

$$P_{bb} = \frac{1}{2} A_r \int_f^{f+B} \int_{4\pi} B_f(\theta, \phi) F(\theta, \phi) d\Omega df \quad (1.4)$$

where,  $P_{bb}$  is the power received by the antenna,  $A_r$  is the effective antenna aperture,  $B$  is the bandwidth,  $F(\theta, \phi)$  is the antenna pattern,  $T$  is the blackbody temperature and the  $\frac{1}{2}$  factor accounts for one component of the unpolarized signal.

Substituting eqn. (1.3) into eqn. (1.4) and applying the relationship between antenna solid angle and effective aperture, we get,

$$\begin{aligned} P_{bb} &= \frac{A_r kTB}{\lambda^2} \int_{4\pi} F(\theta, \phi) d\Omega \\ &= \frac{A_r kTB}{\lambda^2} \Omega_p \\ &= kTB \end{aligned} \quad (1.5)$$

where,  $k$  is Boltzmann's constant,  $T$  is the physical temperature of the blackbody,  $B$  is the bandwidth and  $\Omega_p$  is the antenna solid angle, that cancels out wavelength and antenna effective aperture, giving the KTB relationship.

As a result of eqn. (1.5), in the microwave regime temperature is generally used instead of power to describe emissions. In the case of greybody emission,  $T$  in eqn. (1.5)

represents the blackbody equivalent temperature satisfying the equation and is known as the *brightness temperature* ( $T_b$ ). Thus in terms of emissivity, brightness temperature can be defined as

$$T_b(\theta, \phi) = \varepsilon(\theta, \phi)T \quad (1.6)$$

where  $T_b$  is brightness temperature,  $T$  is the physical temperature of the body and  $\varepsilon$  represents emissivity defined by eqn. (1.2). Contributions to passive microwave remote sensing measurements of upwelling radiance at the Top of Atmosphere (TOA) are graphically illustrated in Fig. 1.5.

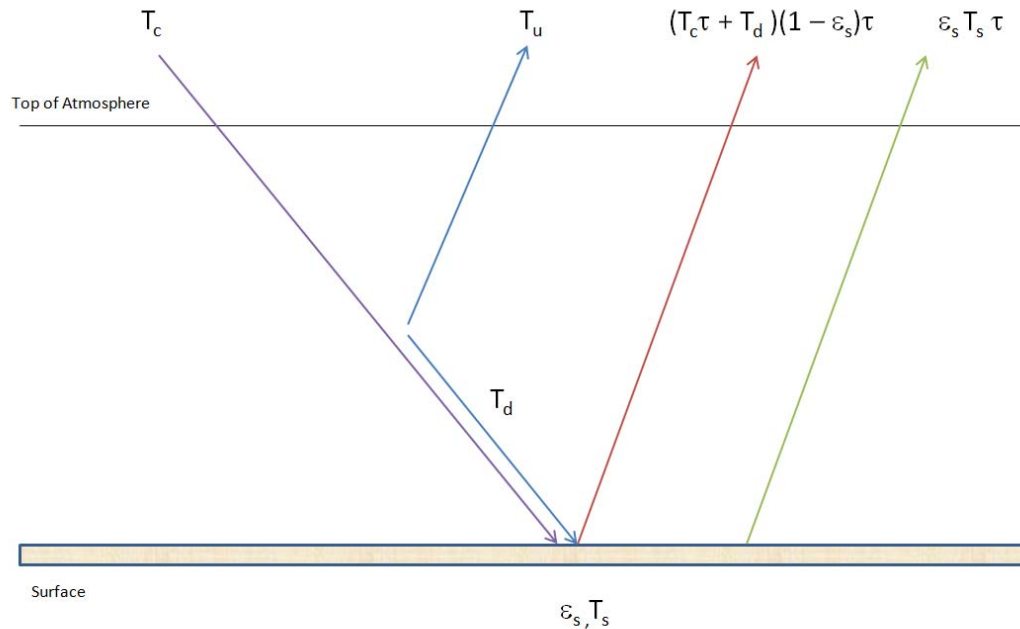


Fig. 1.5: Depiction of various upwelling radiance components of microwave remote sensing measurements at TOA

From Fig. 1.5, the microwave contributions can be broken down into the following components: (a) Upwelling atmospheric emission ( $T_u$ ); (b) Downwelling atmospheric

emission ( $T_d$ ); (c) Cosmic background brightness temperature ( $T_c$ ); and (d) Surface temperature ( $T_s$ ). The upwelling atmospheric emission represents the blackbody emission from the atmosphere above the surface towards the TOA.  $T_u$  is a combination of emissions of each individual layer of the atmosphere attenuated by the layers above it, as shown below

$$T_u(\theta) = \sec \theta \int_0^{TOA} T(z) \alpha(z) e^{-\sec \theta \int_z^{TOA} \alpha(z') dz'} dz \quad (1.7)$$

where,  $\theta$  represents the incidence angle off nadir,  $T(z)$  is the vertical temperature profile of the atmosphere,  $\alpha(z)$  is the vertical absorption profile of the different emission layers of the atmosphere. A plane-parallel atmosphere is assumed for the equation above, that is, it is assumed that the emission/absorption and thermal properties are homogenous within an atmospheric layer horizontally. Similar to upwelling atmospheric emissions,  $T_d$  represents a combination of emissions from each individual layer of the atmosphere towards the surface attenuated by the layers below it. This is shown by,

$$T_d(\theta) = \sec \theta \int_{TOA}^0 T(z) \alpha(z) e^{-\sec \theta \int_0^z \alpha(z') dz'} dz \quad (1.8)$$

where, the equation parameters are the same as eqn. (1.7), except that the direction of the integrals is reversed. Both upwelling and downwelling emissions above assume no scattering from the atmosphere. Generally, microwave emissions are free of atmospheric scattering unless it rains. The cosmic background temperature of around 2.7K, gets attenuated by the transmissivity of the atmosphere before being reflected back upwards from the surface. The amount of brightness temperature reflected back depends on the

surface emissivity  $\varepsilon_s$ , or surface reflection coefficient  $1-\varepsilon_s$ . Here we assume specular and not diffuse scattering of the downwelling brightness temperature. This reflected Tb is further affected by transmissivity of the atmosphere to give an upwelling brightness temperature contribution as shown below,

$$T_{reflected}(\theta) = [T_c\tau(\theta) + T_d(\theta)](1 - \varepsilon_s(\theta))\tau(\theta) \quad (1.9)$$

where,  $\tau$  is the transmissivity of the atmosphere,  $\theta$  represents the incidence angle off nadir and  $\varepsilon_s$  represents surface emissivity. The final contribution to the upwelling radiance component is from surface temperature  $T_s$ , which is the blackbody radiation at that temperature attenuated by the atmosphere as shown below,

$$T_{top}(\theta) = T_s\varepsilon_s(\theta)\tau(\theta) \quad (1.10)$$

where,  $T_s$  is the surface temperature,  $\tau$  is the transmissivity of the atmosphere,  $\theta$  represents the incidence angle off nadir and  $\varepsilon_s$  represents surface emissivity. The total upwelling microwave radiance can be summarized as follows,

$$T_b(\theta) = T_u(\theta) + [[T_c\tau(\theta) + T_d(\theta)](1 - \varepsilon_s(\theta)) + T_s\varepsilon_s(\theta)]\tau(\theta) \quad (1.11)$$

In addition to assuming specular scattering, no atmospheric scattering and a plane-parallel atmosphere, eqn. (1.11) is also polarization dependant. Based on brightness temperature measurements received by the radiometer, it is possible to estimate information such as temperature, absorption, or scattering by inverting eqn. (1.11). This information helps retrieve geophysical parameters such integrated atmospheric water

vapor [9], soil moisture [10], sea-surface salinity [11-12], rain-rate [13], wind-speed [14] etc.

As an example of retrieving geophysical parameters, two high profile microwave remote sensing missions, by the European Space Agency (ESA) and the National Aeronautics Space Agency (NASA), have been commissioned to measure sea-surface salinity. ESA launched an L-band sea-surface salinity measuring mission Soil Moisture Ocean Salinity (SMOS) in November 2, 2009. Similarly, NASA plans to launch their sea-surface salinity mission Aquarius, operating at the 21 cm hydrogen line, by July of 2011. Since 1.4 GHz is in the protected frequency band (to reduce Radio Frequency Interference) and brightness temperature is sensitive to changes in salinity at low frequencies, L-band was chosen.

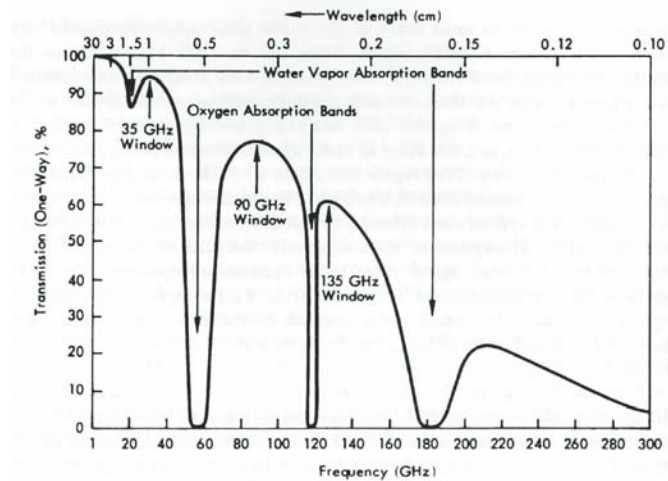


Fig. 1.6: Percentage transmission through the earth's atmosphere, along the vertical direction, under clear sky conditions. (courtesy [7])

The retrieval principle behind both missions is very simple. At L-band, most of the atmospheric emission is negligible and the atmosphere has a high transmissivity, as shown by Fig. 1.6. Effectively, the brightness temperature measured by the radiometer

will be surface emission convolved by its antenna pattern. Emissivity is a complex quantity that depends on properties of the water [15] such as salinity, temperature etc. A study by [16] discussed various possible error sources affecting the retrieval of salinity through brightness temperature. Along with sea surface temperature it is found that sea surface roughness can affect retrieved emissivity. Tbs increase by a few tenths of a Kelvin due to roughness decreasing salinity retrievals. Low frequencies are also affected by Faraday rotation due to the ionosphere that can influence Tbs up to 10K. Significant error can result from direct or reflected solar radiation as well as galactic radiation. Second order error sources arise from atmospheric water vapor and clouds. [16] concluded that these error sources can be corrected for with accurate supplemental knowledge of the parameters involved to get an accurate brightness temperature and hence emissivity measurement. By relating the emissivity to reflectivity via conservation of energy [17], we get the relationship shown below, which in turn is related to the Fresnel reflection coefficient.

$$\varepsilon(\theta) = 1 - R(\theta) = 1 - |r(\theta)|^2 \quad (1.12)$$

where  $\varepsilon$  is emissivity,  $R$  is reflectivity,  $\theta$  is the incidence angle and  $r$  is the Fresnel reflection coefficient. The above equation assumes a smooth dielectric interface. The Fresnel reflection coefficient for the H-polarization is shown below.

$$r(\theta) = -\frac{\sqrt{\{e - \sin^2(\theta)\} - \cos(\theta)}}{\sqrt{\{e - \sin^2(\theta)\} + \cos(\theta)}} \quad (1.13)$$

where  $e$  is the dielectric constant. The Fresnel reflection coefficient is a function of the dielectric constant of water, which is dependent on the salinity of the water. Thus, by

measuring the apparent brightness temperature at the radiometer it is possible to back out salinity information from the sea.

### 1.3 Nature of thermal emissions and interference

#### 1.3.1 Statistical nature of thermal emissions

Random noise generally has a normal probability distribution as shown below,

$$f(x) = \frac{1}{\sigma\sqrt{2\pi}} e^{-\frac{(x-\mu)^2}{2\sigma^2}} \quad (1.14)$$

where,  $x$  is the random variable,  $\sigma$  is the standard deviation of the signal and  $\mu$  is the mean. Such noise is called Gaussian noise since it has a Gaussian probability density function. Blackbody radiation has the same stochastic properties as pure Gaussian noise [18]. The Gaussian nature of blackbody emission is a result of the law of large numbers (i.e. the central-limit theorem). The emitted radiation field can be considered to be composed of contributions from a very large number of statistically independent vibrating atomic sources [19]. The nature of the emission has been investigated in classical terms by [20] and discussed by authors such as Einstein (1915) and Von Laue(1915) [21-23].

Blackbody radiation in thermal equilibrium can be considered as “*chaotic electromagnetic radiation*”[24]. As discussed in [24], the electric field strength of every independent thermal contribution can be represented by

$$a_f(t) = a_c \cos(2\pi ft) + a_s \sin(2\pi ft) \quad (1.15)$$

where  $a_c$  and  $a_s$  are independent random variables. Based on the central limit theorem [25], the asymptotic probability distribution of resultant contribution from infinitely many of these *arbitrary* distributions approaches normality [24].

In passive microwave remote sensing, a radiometer is responsible for detecting the power in a specific spectral band associated with naturally occurring thermal emissions, which is proportional to  $T_b$ . A radiometer receives these signals in the form of an electromagnetic wave captured by its antenna. Thus, effectively the variance of the incoming Gaussian noise signal is equivalent to  $T_b$ . Measurement of the variance requires that the signal be first squared and then averaged in time. Based on the type of radiometer, the incoming signal is squared in different manners. Radiometers such as the Total power radiometer, Dicke radiometer, Noise-injection radiometer, etc., typically employ an analog square-law detector to measure power [26]. Recent advances in radiometry have seen the installation of digital back-ends replacing the square-law detector for performing power measurements in the digital domain[27-30].

### **1.3.2 Man-made interference**

A radiometer passively measures the power of every source that presents itself at the antenna and does not distinguish between the nature of sources. As a result, a microwave radiometer measures not only the power (brightness) of natural microwave emissions, but also active man-made signal sources. Such man-made sources are known as Radio-Frequency Interference (RFI).

### 1.3.2.1 Statistical nature of RFI

The statistical nature of such RFI sources is typically very different than natural emission sources. [31] show that the typical form of RFI is sinusoidal, with an amplitude distribution illustrated in Fig. 1.7. The top and bottom plots show examples of the difference in probability distribution between natural and RFI source amplitudes.

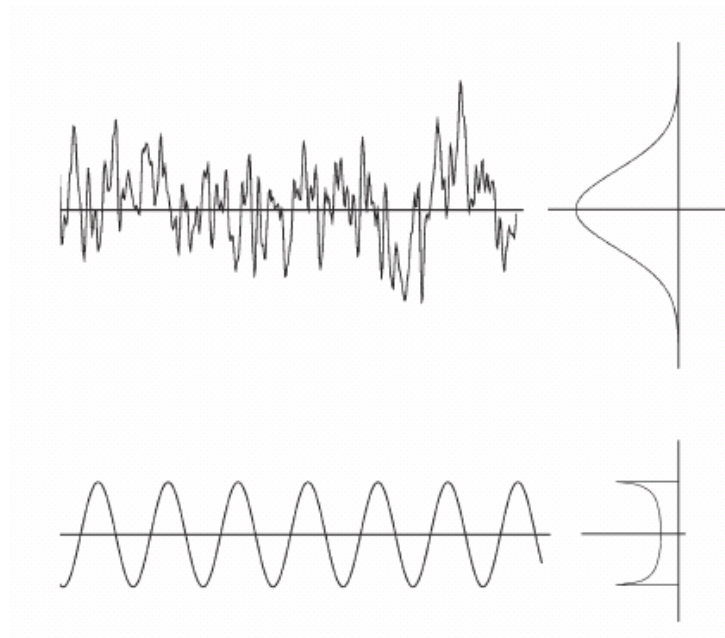


Fig. 1.7: Examples of pre-detection signals. On the left are time-domain representations of the signals, and their pdfs are shown on the right. The top plot represents Gaussian distributed geophysical signals/receiver noise and the bottom plot represents a sinusoid, a presumed typical non-Gaussian RFI noise. (courtesy [31])

### 1.3.2.2 Impact of RFI

In spite of significant statistical differences, RFI sources can easily be mistaken for natural thermal emission when their power is measured by radiometers. The most blatant instances of RFI manifest themselves as nonphysical bright “hot spots” in images of microwave brightness temperature. Their impact on the measurements can, in some cases, be mitigated if it is possible to isolate them, either temporally or spectrally, from

other RFI-free measurements. Much more prevalent (and insidious) than nonphysical hot spots is low-level RFI, which impacts the measurements in similar ways as the expected natural variability in the brightness temperature. Failure to detect such RFI sources can adversely affect the quality of retrieved science measurements. As mentioned in [32], RFI always introduces a positive bias to Tb measurement and doesn't "*average down*" over time like other sources of error. An exception to this would be for cases such as SMOS, which is an interferometric radiometer. Due to its interferometric nature, RFI can present itself as a positive as well as negative bias. Details can be found in Chapter 5. Undetected RFI in soil-moisture measurements can incorrectly make the soil appear drier (positively-biased RFI) than it actually is, which can in turn cause an underestimation of flooding events, or can result in influencing cloud production forecasting, or latent heat transfer due to surface heating, or even impact long-term climatological measurements [32].

### **1.3.2.3 Prevalence of RFI**

The microwave portion of the thermal emission spectrum is often best suited for remote sensing purpose because of its sensitivity to a particular property of interest or because it suffers less attenuation by the intervening atmosphere between the source of surface emission and the sensor. Unfortunately, the relative insensitivity of the microwave region to atmospheric effects also makes it an extremely attractive spectral range for wireless communication and for radars. There has been explosive growth recently in satellite telecommunication, in high-bandwidth point-to-point terrestrial wireless communication links, in wireless routers, and in personal wireless devices like cell phones and Bluetooth

devices. Almost all of these users operate in the microwave portion of the spectrum, in or near the bands that are most commonly used for passive microwave remote sensing. As a result, extremely pervasive low levels of radio-frequency interference (RFI) have begun to be observed by a number of spaceborne microwave radiometers, for example in the C- and X-band portions of the spectrum near 6–7 and 10–11 GHz, respectively by AMSR-E and WindSat satellites [33-37]. With the launch of the European Space Agency's (ESA) Soil Moisture and Ocean Salinity (SMOS) mission, there is ample evidence of RFI in and near the protected 21 cm hydrogen band (L-band) [38], also seen in airborne missions such as [39-41]. There has also been evidence of RFI in the K-band as seen by [42-43].

#### **1.3.2.4 Types of RFI**

As mentioned above, RFI is generally modeled as a sinusoidal wave. Such a sinusoidal wave can further be separated into two categories: Pulsed and continuous-wave (CW). Based on analysis done [44], it had been found that air-defense and air-traffic control radars would be the primary source of RFI at L-band. Radars generally have a pulsed nature, and hence much of the RFI detection algorithm analysis to date has been done assuming a pulsed-sinusoidal RFI signal [31, 45].

Communication signals on the other hand are generally of a continuous nature. Depending on the modulation scheme employed, the signals have some finite bandwidth around its carrier frequency. Such signals are still modeled as a pulsed-sinusoid with a 100% duty-cycle. Frequency bands other than L-band carry signals from TV stations, or satellite downlink channels, or wireless communication towers, all of which behave like a CW signal. Another type of RFI source that has been studied is spread-spectrum type

communication signals [46]. These communication protocols were developed to operate below the noise-floor and temporally and spectrally look like noise by using innovative techniques such as frequency hopping or code-division multiple access. These signals are considered relatively harder to detect. The low power characteristic of these signals makes it hard to detect due to low signal-to-noise (SNR) ratios. Appendix II details the detectability of such spread-spectrum type RFI sources using conventional detection algorithms.

The RFI nature at L-band over the continental USA was characterized using data from an airborne mission SMAPVEX, with a primary mission to develop soil-moisture algorithms. Results from that study, indicate the the relative percentage of CW RFI to pulsed-type RFI for L-band is low. Details of the study can be found in Appendix I, where the occurrence and frequency of man-made RFI is measured, and the performance of RFI detections algorithms (discussed in next section) evaluated.

#### **1.4 Detection and Mitigation algorithms**

With the increase in RFI in various bands of passive microwave remote sensing, it becomes necessary to develop and implement RFI detection and mitigation algorithms to avoid contamination of scientific data. According to the International Telecommunications Union (ITU) – *studies have established that measurements in absorption bands are extremely vulnerable to interference because, in general, there is no possibility to detect and to reject data that are contaminated by interference, and because propagation of undetected contaminated data into models may have a destructive impact on the reliability/quality of weather forecasting[47]* . ITU goes on to recommend that most interference levels should be around 0.2 times the noise-margin of

the measuring radiometer. The noise margin of a radiometer is known as its Noise Equivalent Differential Temperature or NE $\Delta$ T. The NE $\Delta$ T represents the sensitivity of the Tb measurements made by the radiometer and is calculated as shown below,

$$NE\Delta T = \frac{T_{sys}}{\sqrt{B\tau}} \quad (1.16)$$

where,  $T_{sys}$  is the overall system temperature of the receiver (combination of antenna temperature and receiver temperature),  $B$  is the bandwidth of the radiometer system and  $\tau$  is the integration time of the radiometer.

Many attempts have been made at developing a robust RFI detection algorithm. RFI detection algorithms can be broadly classified into five categories.

1. Spectral detection
2. Temporal detection
3. Statistical detection
4. Spatial detection
5. Stokes detection

The five detection principles can be combined together in various manners to create an optimal detection technique. This is illustrated in Fig. 1.8. All types of algorithms can be implemented using analog hardware or digital back-ends.

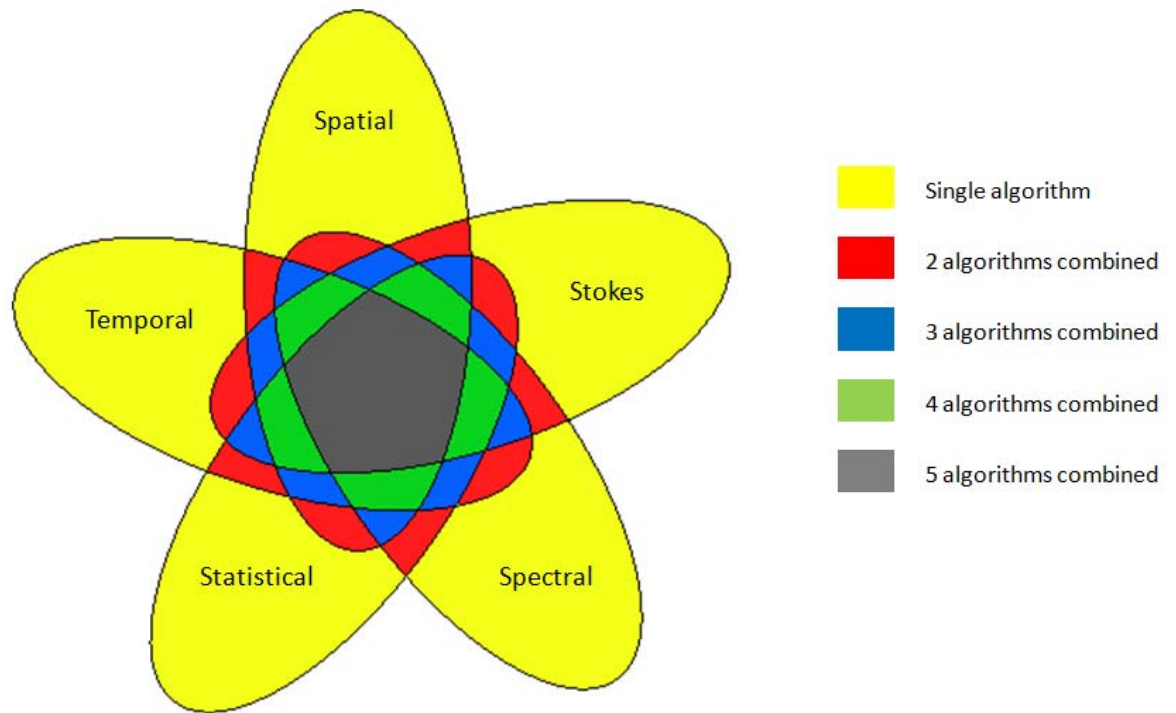


Fig. 1.8 Venn diagram illustrating five separate RFI detection principles and their possible combinations for implementation purposes.

Spectral detection techniques involve dividing the incoming radiometric signal into various spectral bins. [48] attempted to detect and mitigate RFI using an analog bank of parallel sub-band filters. This technique allows strong, narrow-band RFI to be detected relatively easily. [49-50], have implemented a similar spectral detection technique in the digital domain. The digital technique has an advantage of increased spectral resolution and hence improved detectability. Although the spectral detection technique is suitable for narrow-band, CW type RFI [51], it is unable to distinguish between low-level RFI and the radiometric noise (NEAT), which, as mentioned before, can impact scientific measurements. Another issue with such spectral techniques is their practicality when considering implementation on space-borne radiometers. A very high spectral resolution

means higher amount of data being transmitted back to the ground station, which might not be feasible, unless some sort of RFI-related processing is done on-board.

Temporal detection techniques [49-50] rely on chopping the signal into smaller (shorter) temporal bins. The incoming radiometric signal is highly oversampled, thus increasing the temporal resolutions. Such algorithms can then easily detect pulsed-type RFI signals that are active for a much shorter time interval than the radiometer's science-based integration time. The algorithm's capability decreases as the width of the pulse relative to the temporal resolution increases. This is discussed in detail in Chapter 3. Similar to the spectral algorithms, high temporal resolution algorithms impact data bandwidth and have difficulty detecting low-level RFI. A preliminary study of detectability of such a temporal algorithm is discussed in Appendix I.

The third detection technique, spatial algorithms, considers detecting RFI based on variability of the brightness temperature in the spatial domain [34]. Any "hot-spot" on a brightness-temperature map compared to its neighboring pixels is flagged as RFI. The advantages and disadvantages of such a technique are discussed in detail in Chapter 5.

The fourth technique relies on the Gaussian nature of the incoming thermal signal. As discussed in Sec 1.3, natural thermal emission has a normal distribution, whereas typical RFI signals have a distribution that is distinctly non-Gaussian. Statistical detection techniques such as the kurtosis algorithm [31-32, 52] take advantage of this fact and measure higher-order moments of the incoming signal to detect deviations of the signal from normality. The advantage of such a detection algorithm is the fact that it can detect certain types of low-level RFI which go undetected by the other algorithms. In spite of

measuring more moments, the kurtosis algorithm does not necessarily tax data bandwidth resources since temporal and spectral sub-divisions can be relaxed without impacting that detectability performance (see Chapter 3 for a more detailed discussion). The algorithm also has blind-spots for certain types of RFI, as discussed [31-32, 53-54] and investigated further in Chapter 4. Chapter 3 discusses the kurtosis detection algorithm in greater detail.

The fifth and final detection technique has only been recently implemented by [38], where the third and fourth Stokes signals are observed for anomalous behavior. Generally the Stokes signals are expected to be around 0K for thermal emissions, but RFI sources with polarized signatures can be picked up by the above algorithm.

As indicated in Fig. 1.8, any of the following techniques can be combined together. [50] divide the incoming data into spectral and temporal grids for RFI detection. Similarly, [32, 55] apply a statistical detection technique after dividing the incoming signal into spectral bins, whereas [52] use a single channel for statistical detection with a much higher temporal resolution.

## **1.5 Structure of thesis**

The thesis follows the development, analysis and/or implementation of various RFI detection algorithms for different radiometric platforms. Each RFI algorithm is unique with respect to the individual platform, based on the hardware and data bandwidth resources available. The flow-chart shown in Fig. 1.9 below indicates the progression of methods presented in the thesis.

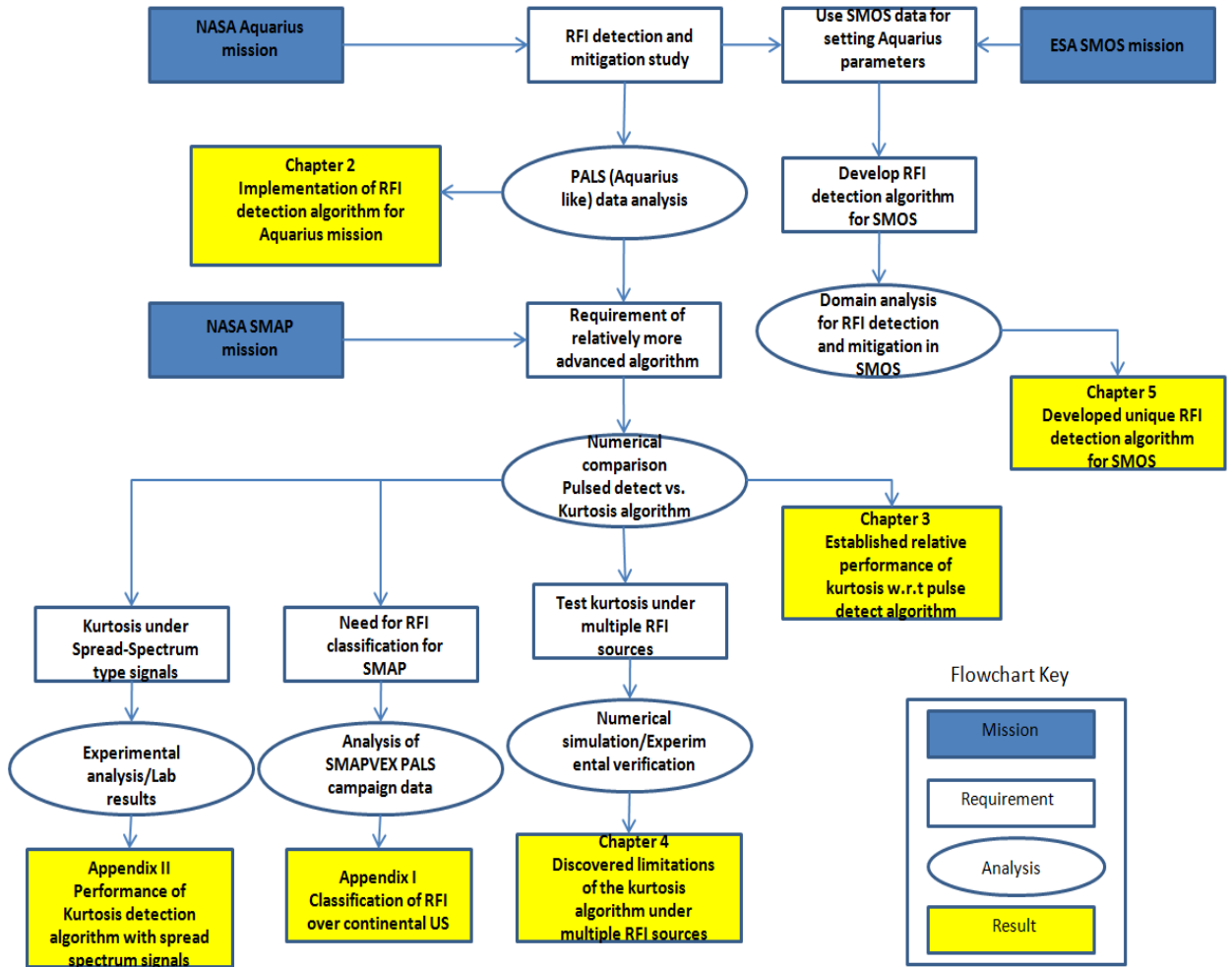


Fig. 1.9: Flowchart of dissertation topic.

Chapter 2 discusses the implementation of an RFI detection algorithm for the Aquarius radiometer. The algorithm compares individual brightness temperature samples with a local mean obtained from neighboring temporal samples. If the sample under test deviates significantly from the local mean then it is assumed to be corrupted by RFI. The algorithm has several adjustable parameters to optimize RFI detection. The performance of the algorithm has been characterized as a function of these parameters using a new form of RFI “ground truth” that is based on the kurtosis of the amplitude distribution of the pre-detected voltages of a radiometer. Ground based radiometric data obtained from a

JPL-PALS (Jet Propulsion Laboratory – Passive Active L /S band radiometer) campaign were used to assess the performance of the algorithm. False alarm rates and the dependence of false alarms on worst case naturally occurring brightness temperature variations on orbit are determined as functions of the adjustable parameters of the algorithm.

Chapter 3 considers a possible implementation of a statistical detection algorithm in the Soil Moisture Active Passive (SMAP). Two algorithms used in microwave radiometry are discussed for RFI detection and mitigation - the pulse detection algorithm and the kurtosis detection algorithm. The relative performance of the algorithms is compared both analytically and empirically. Their probabilities of false alarm under RFI-free conditions and of detection when RFI is present are examined. The downlink data rate required to implement each algorithm in a spaceborne application is also considered. The kurtosis algorithm is compared to a pulse detection algorithm operating under optimal RFI detection conditions. The performance of both algorithms is also analyzed as a function of varying characteristics of the RFI. The RFI detection probabilities of both algorithms under varying subsampling conditions are compared and validated using data obtained from a field campaign. Implementation details, resource usage, and post processing requirements are also addressed for both algorithms.

Chapter 4 discusses some of the issues faced by the kurtosis detection algorithm as demonstrated in several airborne field campaigns [56-57]. The performance of the kurtosis algorithm in detecting multiple-source RFI is characterized. A new RFI

statistical model is presented which takes into account the behavior of multiple RFI sources which may be present in a large antenna foot-print. Results characterize the behavior of the kurtosis detection method under central-limit conditions due to a large number of RFI sources.

Conventional RFI detection techniques have different behavior and challenges for interferometric radiometers such as the MIRAS (Microwave Imaging Radiometer using Aperture Synthesis) radiometer on the SMOS mission. SMOS does not have high (i.e. over-sampled) temporal resolution, or any kind of spectral resolution. Chapter 5 contrasts and compares different domains of SMOS such as the Visibility domain, Brightness temperature spatial domain or Brightness temperature angular domain to apply the RFI detection algorithm.

Chapter 6 summarizes the original contributions of the thesis and possible future research topics to build upon this work.

## **1.6 Personal Contributions**

Work from this thesis and related to this thesis has resulted in a few journal and conference publications. The following publications have contributed some insight or knowledge to the relatively new field of RFI detection algorithms for microwave radiometry.

1. Ruf, C.S., S. M. Gross and S. Misra, "RFI Detection and Mitigation for Microwave Radiometry with an Agile Digital Detector," IEEE Trans. Geosci. Remote Sens., vol. 44, no. 3., 694-706, March 2006.

- The above paper was the first publication detailing a statistical RFI detection technique (kurtosis) and its results from a field campaign in Canton, MI. My work with this paper involved simulating the detection hardware performance to iteratively set the histogram measuring hardware parameters, designing the digital filter banks required for sub-banding as well as developing the analysis software.
2. S. Misra, Ruf, C.S and R. De Roo, “Agile Digital Detector for RFI Mitigation,” 9<sup>th</sup> Specialist Meeting on Microwave Radiometry and Remote Sensing Applications (MicroRad ’06), San Juan, Puerto Rico, 28 Feb ’06 – 03 Mar ’06
    - This publication continued the discussion on the kurtosis detection algorithm and presented the first results from an airborne field campaign done at C-band over the Gulf, using a new type of kurtosis detector that only measures higher order moments. The impact of a 50% duty-cycle blind-spot on kurtosis detection is also presented.
  3. Ruf, C.S, S. Misra, S. Gross and R. De Roo, "Detection of RFI by its Amplitude Probability Distribution," Proc. 2006 IEEE IGARSS, Denver, CO, 31 Jul - 4 Aug 2006.
    - The above conference proceeding details the performance of kurtosis with power and duty-cycle. My work involved performing analysis and presenting results of the C-band flight campaign. This work won the IGARSS Symposium Prize Paper Award.

4. R. De Roo, S. Misra and Ruf, C.S., “Sensitivity of the Kurtosis as a Detector of Pulsed Sinusoidal RFI,” IEEE Trans. Geosci. Remote Sens. , vol 45, 1938-1946, July 2007
  - The above publication is a highly cited article that details the behavior of the kurtosis detection algorithm under digitization, in the presence of pulsed sinusoidal RFI. The noise statistics of kurtosis and its blind-spots are also covered. My work primarily involved developing the pulsed-sinusoidal distribution model and then comparing field-campaign observations with the combined (Gaussian+RFI) distribution model developed by the first author.
5. Ruf, C.S and S. Misra, “Detection of Radio Frequency Interference with the Aquarius Radiometer,” Proc. 2007 IEEE IGARSS, Barcelona, Spain, 23-28 July 2007, pp 2722-2725
  - This conference proceeding presents a first look at the RFI detection algorithm for the Aquarius mission. My work involved designing an implementable detection algorithm tailored to Aquarius system. This algorithm is now the working detection algorithm for the Aquarius mission.
6. R. De Roo, S. Misra and Ruf, C.S., “Sensitivity of the Kurtosis statistic as a Detector of Pulsed Sinusoidal Radio Frequency Interference,” Proc. 2007 IEEE IGARSS, Barcelona, Spain, 23-28 July 2007, pp 2706-2709
  - In the above paper we performed experimental verification of the kurtosis sensitivity model mentioned before using a bench-top radiometer system.

7. S. Misra, Kristensen, S., Steen, S. And Skou, N., "CoSMOS: Performance of Kurtosis Algorithm for Radio Frequency Interference Detection and Mitigation," Proc. 2007 IEEE IGARSS, Barcelona, Spain, 23-28 July 2007, pp 2714-2717
  - The above conference proceeding detailed the performance of the kurtosis detection algorithm for the CoSMOS mission, a Technical University of Denmark (DTU) led support mission for SMOS. The robustness of kurtosis to non-stationary scenes was presented, as well as a detectability study was performed on the data to determine the sensitivity of kurtosis to generic RFI of various power levels.
8. R. De Roo and S. Misra, "Effectiveness of the sixth moment to eliminate a kurtosis blind-spot in the detection of interference in a radiometer," Proc. 2008 IEEE IGARSS, Boston, MA, 7-11 July 2008, pp 331-334
  - The above study was undertaken to assess the performance of a sixth moment RFI detector. Kurtosis suffers from a blind-spot from RFI signals that have a 50% duty-cycle. The authors developed a new higher-order detection technique to eliminate the such blind-spots.
9. S. Misra, Ruf, C.S., and Kroodsma, R., "Detectability of Radio Frequency Interference due to spread-spectrum communication signals using the kurtosis algorithm," Proc. 2008 IEEE IGARSS, Boston, MA, 7-11 July 2008, pp 335-338
  - The above proceeding publication tested the detectability of spread-spectrum type RFI by the kurtosis statistic. This work answered the question, to whether kurtosis can detect RFI that has temporal noise-like

properties. Laboratory experiments were performed, indicating reduced sensitivity of kurtosis.

10. S. Misra and Ruf, C.S., "Comparison of pulsed sinusoid Radio Frequency Interference detection algorithms using time and frequency sub-sampling," Proc. 2008 IEEE IGARSS, Boston, MA, 7-11 July 2008, pp 153-156

- The above conference proceeding compares the kurtosis detection algorithm to other popular RFI detection algorithms. Results indicate the superior performance of the kurtosis detection algorithm with temporal and spectral sub-banding compared to a pulse-detection algorithm.

11. R. De Roo and S. Misra, "A Demonstration of the Effects of Digitization on the Calculation of Kurtosis for the Detection of RFI in Microwave Radiometry," IEEE Trans. Geosci. Remote Sens., vol. 46, no. 10., 3129-3136, Oct. 2008

- The above journal publication discusses distortions that the kurtosis statistic suffers from due to digitization effects. This is demonstrated using a controlled laboratory experiment with known sources injected into a radiometer. My contribution has involved detailed discussions with the first author regarding the impact of such digitizers, especially dealing with the impact of truncation or saturation errors on kurtosis.

12. S. Misra and Ruf, C.S., "Detection of Radio Frequency Interference for the Aquarius Radiometer," IEEE Trans. Geosci. Remote Sens., vol. 46, no. 10., 3123-3128, Oct. 2008

- This journal publication details the RFI detection algorithm for the Aquarius radiometer. This paper has contributed towards an

implementable RFI detection algorithm for the mission, with four separate parameters that can be modified based on probability of detection and false alarm rate.

13. S. Misra and Ruf, C.S., “Inversion algorithm for estimating Radio Frequency Interference characteristics based on kurtosis measurements,” Proc. 2009 IEEE IGARSS, Cape Town, South Africa, 12-17 July 2009, pp II-162 – II-165

- The above conference proceeding tackles the issue of signal estimation as well as signal detection. Innovative inversion technique such as simulated annealing was applied along with the traditional Newton-Raphson to back out RFI power and duty-cycle.

14. S. Misra, P. Mohammed, B. Guner, Ruf, C.S., J. Piepmeier, and J. Johnson, “Microwave radiometer Radio Frequency Interference detection algorithms: A comparative study,” IEEE Trans. Geosci. Remote Sens., vol. 47, no. 11., 3742 - 3754, 2009

- The above journal publication compares the pulse detection algorithm used by Aquarius to the kurtosis detection algorithm. The paper coined a new detectability metric to assess RFI detection algorithms called the AUC (Area Under the ROC Curve). The paper helped determine the minimum number of sub-banding filters required for optimum detection performance, as well as show superior performance of the algorithm with a lesser data bandwidth. The characteristic relative performance of the algorithm under varying RFI scenarios was also studied.

15. N. Skou, S. Misra, J. Balling, S. Kristensen and S. Søbjærg. “L-Band RFI as experienced during airborne campaigns in preparations for SMOS,” IEEE Trans. Geosci. Remote Sens., vol. 48, no. 3(2), 1398 - 1407, 2010
- The above journal publication discusses L-band RFI observed over regions of Western Europe. My work involved analyzing the received data, demonstrating the insensitivity of kurtosis to coastal crossing, performing a detectability study to demonstrate the percentage of RFI flagged by kurtosis with respect to RFI power, as well as calculating occurrence statistics of RFI over different regions of the airborne campaign.
16. R. De Roo and S. Misra, “A moment ratio RFI detection algorithm that can detect pulsed sinusoids of any duty cycle,” IEEE Geosci. Remote Sens. Letters, vol. 7, no. 3., 606-610, 2010
- The following IEEE letter, discusses a combined higher order algorithm to detect any type of pulsed-sinusoidal RFI. Here we decided to supplement the kurtosis detection algorithm with a more recently developed sixth moment algorithm for improved RFI detection. This paper also introduced the characteristic function for a pulsed-sinusoid.
17. S. Curry, M. Ahlers, H. Elliot, S. Gross, D. McKague, S. Misra, J. Puckett and Ruf, C.S., “K-band Radio Frequency Interference survey of south-eastern Michigan,” Proc. 2010 IEEE IGARSS, Honolulu, Hawaii, 25-30 July 2010, pp 2486 -2489

- This conference proceeding detailed a student-built RFI survey mission. My contribution involved aiding with the algorithm development with respect to a unique nature of the measuring hardware.

18. S. Misra, R. De Roo and Ruf, C.S., “Evaluation of the kurtosis algorithm in detecting Radio Frequency Interference from multiple sources,” Proc. 2010 IEEE IGARSS, Honolulu, Hawaii, 25-30 July 2010, pp 2019 – 2022

- The above proceedings paper discusses the performance of a kurtosis detection algorithm when observing multiple RFI sources at once. This paper tackles an important issue of RFI modeling and algorithm performance review. The paper presents a new RFI model that is more general than the single pulsed-sinusoidal model used in previous studies. The reason for anomalous behavior of kurtosis observed in past airborne observations is explained in this paper.

19. J. Park, J. T. Johnson, N. Majurec, N. Niamsuwan, J. Piepmeier, P. Mohammed, C. Ruf, S. Misra, S. Yueh and S. Dinardo, “Airborne L-band Radio Frequency Interference observations from the SMAPVEX08 campaign and associated flights,” IEEE Trans. Geosci. Remote Sens. (*in press*)

- The above journal publication is a joint study to analyze the performance of different RFI detection systems using the SMAPVEX campaign fall data. My work involved supporting analysis of the University of Michigan Agile Digital Detector (ADD) system.

## **Chapter 2**

### **Detection of Radio-Frequency Interference for the Aquarius Radiometer**

#### **2.1 Introduction**

The Aquarius low Earth orbiting mission is intended to produce global maps of sea surface salinity (SSS) for use in climate studies. It includes a microwave radiometer operating at 1.4 GHz to measure SSS [58]. The contamination of radiometer data is possible if man-made sources of radio-frequency interference (RFI) are mistakenly detected and interpreted as natural thermal emission by the ocean surface. The presence of RFI has been noted in a number of space-borne microwave radiometers at higher frequencies than that of Aquarius [34] and on airborne radiometers operating at the same frequency as Aquarius [40-41, 59]. The sensitivity of the observed L-band brightness temperature (T<sub>b</sub>) to climatically relevant changes in SSS is low enough that even quite small biases in the observations due to RFI can be detrimental to the mission objectives. Aquarius requires a calibration accuracy of 0.2K to reach a weekly average accuracy of 0.2psu [16]. For this reason, the radiometer's data sampling rate (10ms) has been increased by magnitude factor of approximately 140 above the Nyquist rate (1.44s) suggested by the antenna-footprint size and the spacecraft orbital velocity [44]. This will significantly enhance the flexibility and sensitivity of an RFI "glitch detection" algorithm that will be included as part of the ground processing.

One previous RFI mitigation technique, which is known as “asynchronous pulse blanking,” that takes advantage of high resolution in the temporal domain to detect and remove glitches in real time prior to detection, has been developed [60]. This algorithm has been adapted for use by the Aquarius mission. The Aquarius RFI detection algorithm operates on samples of the antenna temperature, after detection, at their raw (highest) sample rate. It is designed to detect individual samples that significantly differ from the local average value of those nearest neighbor samples that are themselves not corrupted by RFI. There are a number of parameters in the detection algorithm that can be adjusted to control its behavior. Those parameters affect the following: 1) the extent of the region surrounding a sample that constitutes its local neighborhood; 2) the magnitude of the difference between a sample and its local average, which indicates the presence of RFI; and 3) the “guard band” surrounding a sample with RFI that will also be flagged as potentially contaminated. In addition, optimal values for the parameters may vary depending on the proximity of a sample to expected variations in geophysical brightness, such as a major coastline. The behavior of the detection algorithm can be characterized in several ways. The probability of false alarm characterizes excessive sensitivity, in which case RFI is indicated when it is not present. This possibility is more likely near a major coastline, when the natural variations in  $T_b$  are greatest, than it is in the open ocean. The probability of missed detection characterizes the inadequate sensitivity of the algorithm to the presence of RFI. The settings of the parameters in the algorithm must weigh these two competing characteristics against one another in order to reach an acceptable compromise.

The kurtosis algorithm that measures higher order moments has been found to be a reliable indicator of the presence of RFI, even when its power level is extremely low. A series of field campaigns was conducted with a new type of microwave radiometer that uses an agile digital detector (ADD) which measures both the second and fourth moments of the pre-detection voltage [32, 55, 61]. The second moment is the conventional measurement made by a square-law detector. The additional fourth-moment measurement allows the kurtosis of the voltage to be calculated. Data from the ADD field campaigns, if taken at the proper sample rate, can be used as an experimental test bed for assessing the behavior of the Aquarius RFI detection algorithm as a function of its adjustable parameters. In particular, the availability of the kurtosis measurements allows for the experimental verification of the probability of false alarm of the algorithm, which is a statistic that is otherwise difficult to validate with confidence. Details about the kurtosis algorithm and ADD can be found in Chapter 3.

## **2.2 RFI Detection Algorithm**

The algorithm works on the detection principle of flagging any sample above a certain threshold as being contaminated by RFI. There are five steps involved in calculating the threshold and flagging a particular sample. The algorithm consists of four separate parameters that can be varied to control the detection performance.

Denoting  $x_i$  as the radiometric antenna temperature of the sample under test, a set of neighboring antenna temperature samples surrounding  $x_i$  (excluding the sample itself) is chosen to estimate its local mean value. The interval of time within which these samples lie is kept constant to keep the ground track distance covered by the antenna footprint constant. The number of earth viewing samples taken during this time interval varies due

to noise diode and ambient reference calibration samples that are interleaved between multiple earth viewing samples. The number of neighboring samples to be used is determined by the parameter  $W_S$  (window-size). The set of neighboring antenna temperature samples associated with  $x_i$  is given by the following:

$$Y_i = [x_{\left(i-\frac{W_S}{2}\right)}, \dots, x_{(i-1)}, x_{(i+1)}, \dots, x_{\left(i+\frac{W_S}{2}\right)}] \quad (2.1)$$

where  $i = [(W_S/2 + 1), \dots, (N - W_S/2)]$  is the index of samples within the window,  $W_S$ , surrounding  $x_i$ . In order to keep the window symmetric about both sides of  $x_i$ , the parameter  $W_S$  is always an even integer. The set  $Y_i$  may contain certain samples that have been flagged as RFI from previous tests. While calculating the local mean value of  $Y_i$  such samples are not used. The local mean value of  $Y_i$  is defined as follows:

$$\tilde{y}_i = \frac{\sum_{j=\pm 1, \pm 2, \dots, \pm \frac{W_S}{2}} x_{i+j} f_{i+j}}{\sum_{j=\pm 1, \pm 2, \dots, \pm \frac{W_S}{2}} f_{i+j}} \quad (2.2)$$

where  $f_k=0$  if antenna temperature sample  $x_k$  has been previously flagged as having RFI present and  $f_k=1$  if not. The local mean value calculated in this way is termed “dirty” because there might still be RFI contaminated samples in  $Y_i$  that were not flagged. In order to obtain a “clean” local mean, a threshold filter is applied. The threshold is determined using the local mean value given by eqn. (2.2) and a multiple of the radiometric uncertainty (noise equivalent delta temperature, NE $\Delta$ T) of a single sample of the antenna temperature. For Aquarius, the NE $\Delta$ T will vary with each of its three

radiometers. The elements of  $Y_i$  are tested for RFI contamination and flagged if they exceed the threshold test given by the following:

$$f'_{i+j} = \begin{cases} 0, & \text{if } x_{i+j} \geq \tilde{y}_i + T_m \sigma \\ 1, & \text{if } x_{i+j} \leq \tilde{y}_i + T_m \sigma \end{cases} \quad (2.3)$$

where  $f'_k$  is the RFI flag for  $x_k$ ,  $j = [-W_s/2, \dots, -1, 1, \dots, W_s/2]$ ,  $\sigma$  is the NEAT radiometric uncertainty of an individual sample of the antenna temperature, and the threshold level above which RFI is assumed to be present is  $T_m \sigma$ , where  $T_m$  (mean-threshold magnitude) is a scaling factor (not necessarily an integer).  $T_m$  is a variable parameter of the RFI algorithm (value given below). The remaining, RFI-free, elements of  $Y_i$  are averaged together to estimate the local “clean” mean value of  $x_i$ . This test removes any apparent RFI spikes present in  $Y_i$ , along with the naturally occurring at the upper tail-end of the normally distributed signal. The local “clean” mean value is given by the following:

$$\tilde{y}_{ci} = \frac{\sum_{j=\pm 1, \pm 2, \dots, \pm \frac{W_s}{2}} x_{i+j} f_{i+j} f'_{i+j}}{\sum_{j=\pm 1, \pm 2, \dots, \pm \frac{W_s}{2}} f_{i+j} f'_{i+j}} \quad (2.4)$$

The sample under test,  $x_i$ , is then compared to the local clean mean using a second threshold test. If  $x_i$  deviates from the local clean mean by more than a certain multiple of the NEAT then it is considered to be contaminated by RFI and flagged accordingly. This test is given by the following:

$$f_i = \begin{cases} 0, & \text{if } x_i \geq \tilde{y}_{ci} + T_{\text{det}} \sigma \\ 1, & \text{if } x_i \leq \tilde{y}_{ci} + T_{\text{det}} \sigma \end{cases} \quad (2.5)$$

where the threshold level above which RFI is assumed to be present is given by  $T_{det}\sigma$ , where  $T_{det}$  (detection-threshold magnitude) is a scaling factor (not necessarily an integer).  $T_{det}$  is also a variable parameter of the RFI algorithm. This detection threshold test can be less strict than the previous mean threshold test (*i.e.*  $T_{det} > T_m$ ) because it directly results in discarded data, whereas the previous test only lowers the number of samples used to determine the local mean.

If  $x_i$  is flagged due to RFI then a certain number of samples before and after  $x_i$  are also considered to be contaminated by RFI. This is to remove any RFI contaminated samples in the near vicinity of a flagged sample that might be just below the detection threshold. The range of samples to be so flagged is determined based on the characteristic time scale with which signals can enter and leave the radiometer antenna beam versus the time interval between raw samples. This RFI flag can be expressed as follows:

$$f_{i+m} = 0, \quad m = [-W_r, \dots, -1, 1, \dots, W_r] \quad (2.6)$$

where  $W_r$  (range window) is the range of samples so flagged.  $W_r$  is a fourth variable parameter of the detection algorithm.

### 2.3 Ground Truth and FAR

A ground-based campaign was conducted during April–May 2006 at the NASA Jet Propulsion Laboratory (JPL) to assess the performance of the ADD kurtosis detector for RFI detection and mitigation. Measurements were made using a hybrid radiometer consisting of the JPL-PALS RF front end [62] and University of Michigan ADD back end [32]. The sampling characteristics of the measurements and the controlled variation of the observed Tb scene were similar to the expected conditions with Aquarius on orbit.

The Aquarius data system will sample every 10 ms, which is similar to the PALS-ADD system. The spacecraft has a ground track velocity of 7.5 km/s, and the antenna-footprint dimensions of the three radiometer antenna patterns in the along-track direction are 85, 102, and 125 km. For the central 102-km footprint, it will, therefore, take approximately 13 s for the Aquarius Tb to fully transition from ocean to land during a coastal crossing. During this time, roughly 1300 Tb samples will be taken. This is mimicked in the data taken by PALS-ADD by sweeping a blackbody absorber over its sky-looking antenna in 13s. Due to these similarities, the measurements can be used as a proxy for Aquarius flight data to assess the expected performance of the Aquarius RFI detection algorithm.

ADD measures the first four moments of the amplitude distribution of the pre-detected signal. The kurtosis parameter derived from these four moments is a reliable indicator for the presence or absence of RFI at or above  $NE\Delta T$  levels [32]. RFI detection by kurtosis serves as RFI ground truth for the assessment of the performance of the Aquarius RFI detection algorithm.

The performance of the algorithm with respect to its various adjustable parameters is assessed in terms of the false-alarm rate (FAR), which is the probability that RFI will be detected when it is not present. The FAR of the detection algorithm, which uses only the second moment, is obtained by comparing its results to the results obtained by using the kurtosis. It should be noted that the kurtosis algorithm itself has a FAR associated with it. The threshold for RFI detection by the kurtosis was chosen so as to produce an extremely low FAR. The kurtosis FAR is given by the following [31]:

$$FAR = 1 - erf\left(\frac{z}{\sqrt{2}}\right) \quad (2.7)$$

where  $erf()$  is the error function and  $z$  is the normalized kurtosis threshold in units of the theoretical standard deviation of the samples of kurtosis. In eqn. (2.7), it is assumed that the RFI thresholds above and below the mean are equidistant about it. The kurtosis FAR with respect to  $z$  is shown in Fig. 2.1. The dashed line is obtained by using simulated normally distributed data, and the solid line indicates values obtained by using an RFI-free portion of the PALS-ADD data. The curve based on observations is slightly lower than that predicted by eqn. (2.7) as a result of known quantization effects in the measurements [31].

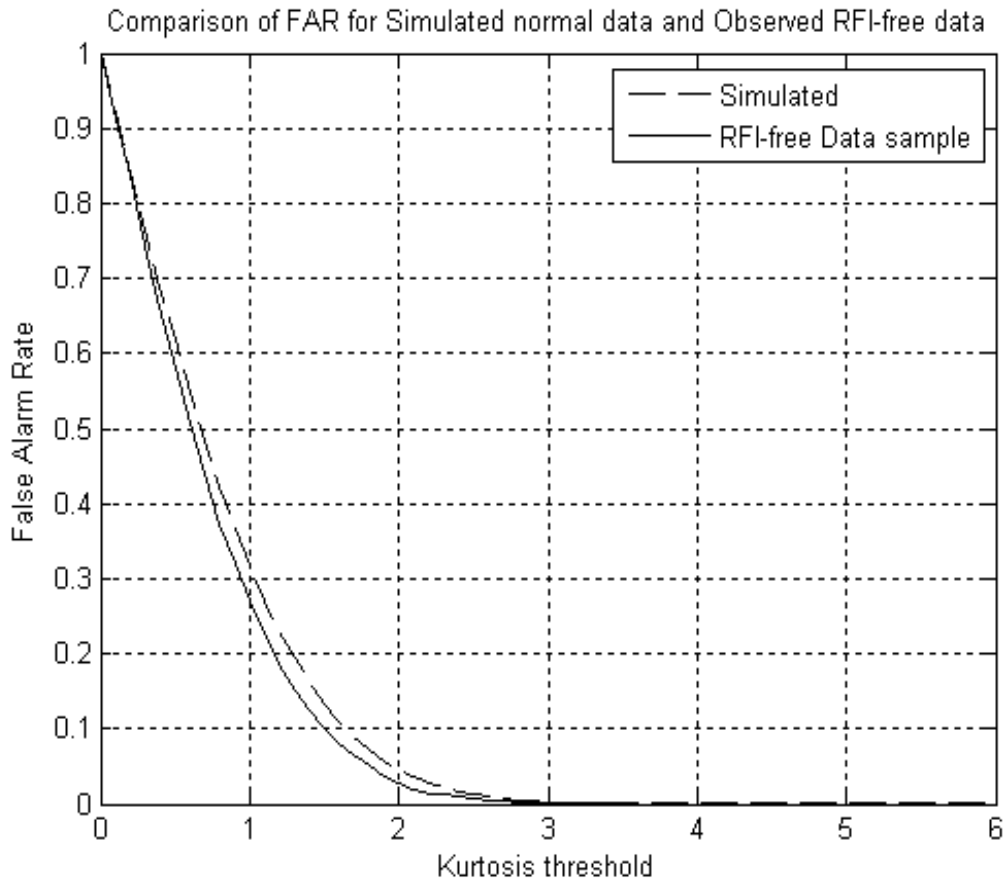


Fig. 2.1: FAR of the kurtosis detection algorithm for various thresholds calculated from normally distributed simulated data (dashed line) and RFI-free PALS-ADD data sample (solid line)

For use as a ground truth reference, the kurtosis threshold is set at 3.7 times the standard error in the estimate of kurtosis (i.e.,  $z = 3.7$ ), which gives the kurtosis algorithm an extremely low FAR of 0.02% from eqn. (2.7). It should be noted that a lower FAR is accompanied by a lower probability of detection. As a result, even though the kurtosis algorithm is nearly error free, it cannot detect all RFI present.

Applying the second-moment detection and kurtosis algorithms to PALS-ADD measurements, it is observed that  $T_m$  and  $T_{det}$  have the greatest effect on second moment detection algorithms FAR. Fig. 2.2 shows the FAR with a varying  $T_m$  value using normally distributed simulated data and RFI-free PALS data. The curves have been generated for different  $T_{det}$  while  $W_r$  and  $W_S$  are held constant. The result shown in Fig. 2.2 is intuitive. If we decrease  $T_m$ , high-amplitude second-moment data are discarded. The local clean mean is, hence, lower, which sets a lower second detection threshold, resulting in more data being flagged and higher FAR.

Similarly,  $T_{det}$  has a significant effect on the detectability of the second-moment detection algorithm. A sample is flagged as being contaminated by RFI whenever the second moment is above the threshold indicated by eqn. (2.5). The dependence of the FAR of the Aquarius detection algorithm on  $T_{det}$  is shown in Fig. 2.3. The FAR is obtained for different levels of  $T_m$  while  $W_r$  and  $W_S$  are held constant. As expected, a lower  $T_{det}$  makes the detection algorithm stricter, and as a result, more data are flagged and the FAR is increased. Because the second-moment data have a Chi-squared distribution, the proper detection threshold can be theoretically determined to produce a desired FAR.

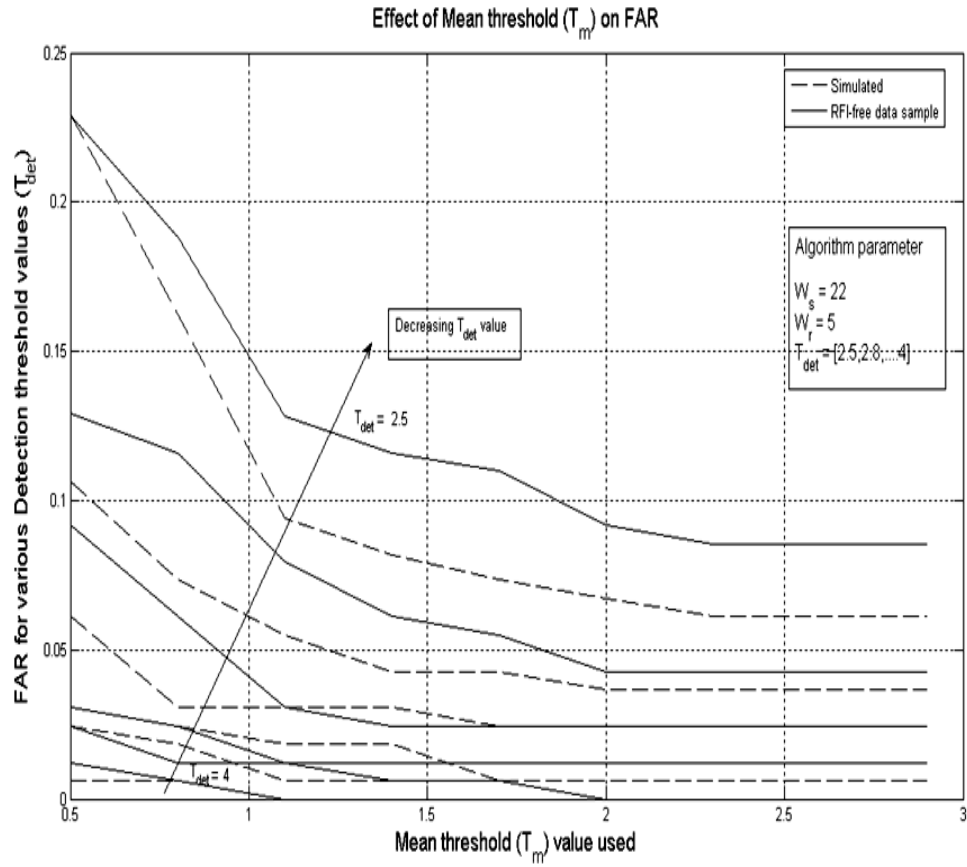


Fig. 2.2: Effect of mean-threshold magnitude,  $T_m$  on the FAR of the second moment detection algorithm for the detection-threshold magnitude,  $T_{det}$  values (from upper right to lower left):  $T_{det} = 2.5, 2.8, 3.1, 3.4, 3.7, 4.0$ .

$W_s$  does not have a significant effect on the FAR of the detection algorithm. In a window that is densely populated with RFI, a larger window size would be helpful in detecting the local clean mean, whereas, in a sparsely RFI-populated data set, the sample window would have less of an effect. Increasing  $W_r$  has no effect on false detection of RFI, but increases the FAR by removing more samples when a false detection occurs.

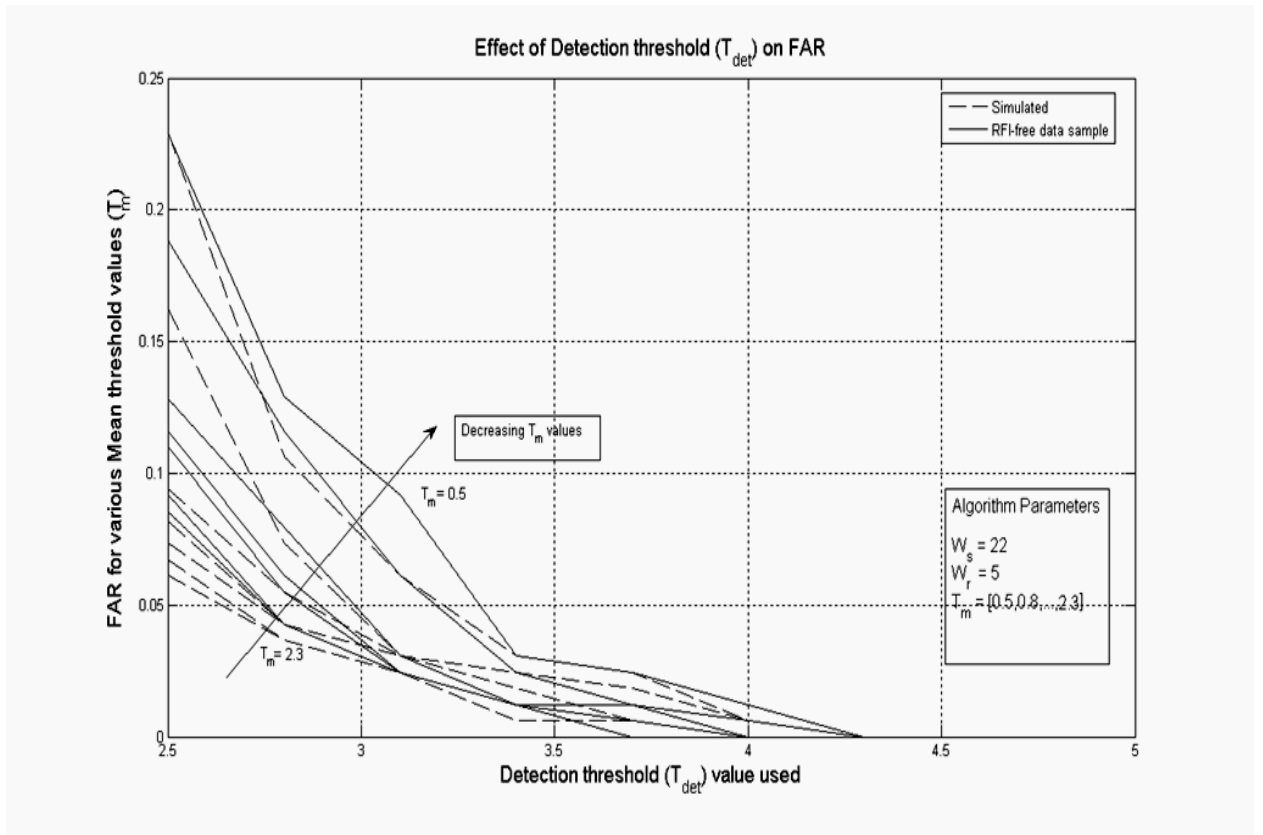


Fig. 2.3: Effect of detection-threshold magnitude,  $T_{det}$  on the FAR of the second moment detection algorithm for the mean-threshold magnitude,  $T_m$  values (from upper right to lower left):  $T_m = 0.5, 0.8, 1.1, 1.4, 1.7, 2.0, 2.3$ .

## 2.4 Performance of the algorithm

PALS-ADD data were used as a proxy for Aquarius on-orbit data in order to characterize the performance to the Aquarius detection algorithm before launch. Fig. 2.4 is an example of algorithm performance on data measured while viewing the sky at nadir. The top panel indicates the second moment of the predetection signal. The estimated value of second-moment data is proportional to the radiometer system noise temperature and includes contributions from the down-welling sky  $T_b$ , thermal emission by the radiometer's antenna and the cabling between the antenna and receiver, and the noise temperature of the receiver itself. The second moment measured by ADD is equivalent to

the Level 0 data product measured by conventional radiometers. The algorithm parameters used in the Aquarius detection algorithm for the following data sets are the following:  $W_s=20$ ,  $T_m=1.5$ ,  $T_{det}=4$ , and  $W_r=5$ . These are candidate values for which the algorithm has a reasonably low FAR but is still able to detect most low level RFI. Other values that also yield satisfactory results are possible, and the determination of optimum values to be used will be an important task during the early phase of the on-orbit evaluation process for Aquarius. In the Aquarius flight processing implementation of the algorithm, all of the parameter values are adjustable as functions of longitude and latitude. This will permit them to be adjusted depending on the prevalence of RFI and the spatial variability of the Tb (e.g., near a coastline or islands versus in open ocean). There are clear spikes in the top panel of Fig. 2.4, which indicate the presence of RFI during daytime weekday operation at JPL. These RFI spikes are considered representative of the interference received by Aquarius because the radiometer integration time has approximately been matched with the pulse width of terrestrial radars operating within the relevant frequency range [44]. The kurtosis measurements are indicated by the center panel. A vertical bar is present whenever the algorithm detects an RFI-contaminated sample. The bottom panel indicates the results obtained from the second-moment detection algorithm. It can be observed that the clear RFI spikes that are visible in the second-moment data are detected by the Aquarius detection algorithm. The kurtosis algorithm flags a few other RFI-contaminated samples in the center panel that are near the NE $\Delta$ T level. Such low-level RFI is missed by the second-moment detection algorithm.

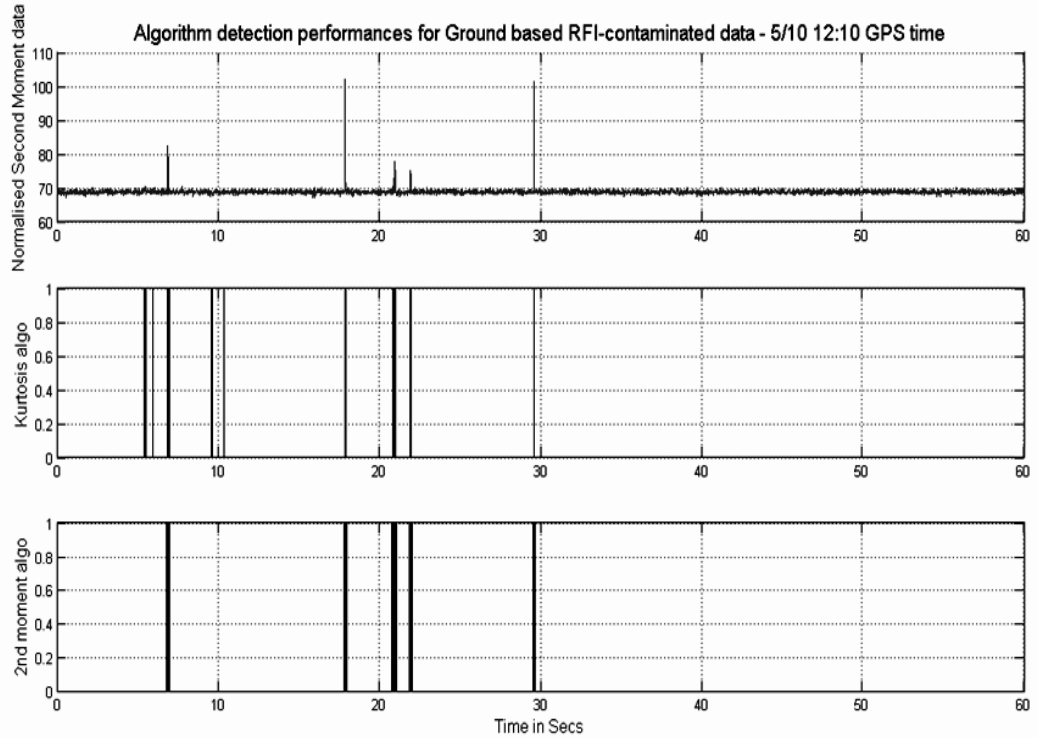


Fig. 2.4: RFI detection of PALS-ADD L-Band radiometer measurements of nadir sky view with strong RFI present: (top) 2<sup>nd</sup> moment time series; (center) kurtosis of signal; (bottom) Aquarius RFI detection algorithm.

It is informative to consider the performance of the Aquarius detection algorithm in terms of RFI false alarms during natural rapid Tb changes such as a coastal crossing. A second PALS-ADD example is shown in Fig. 2.5, in which a blackbody absorber was slowly swept in front of the PALS antenna while looking at the nadir sky. The sweep rate approximates the rate at which the Aquarius footprint on orbit would cross over a coastline.

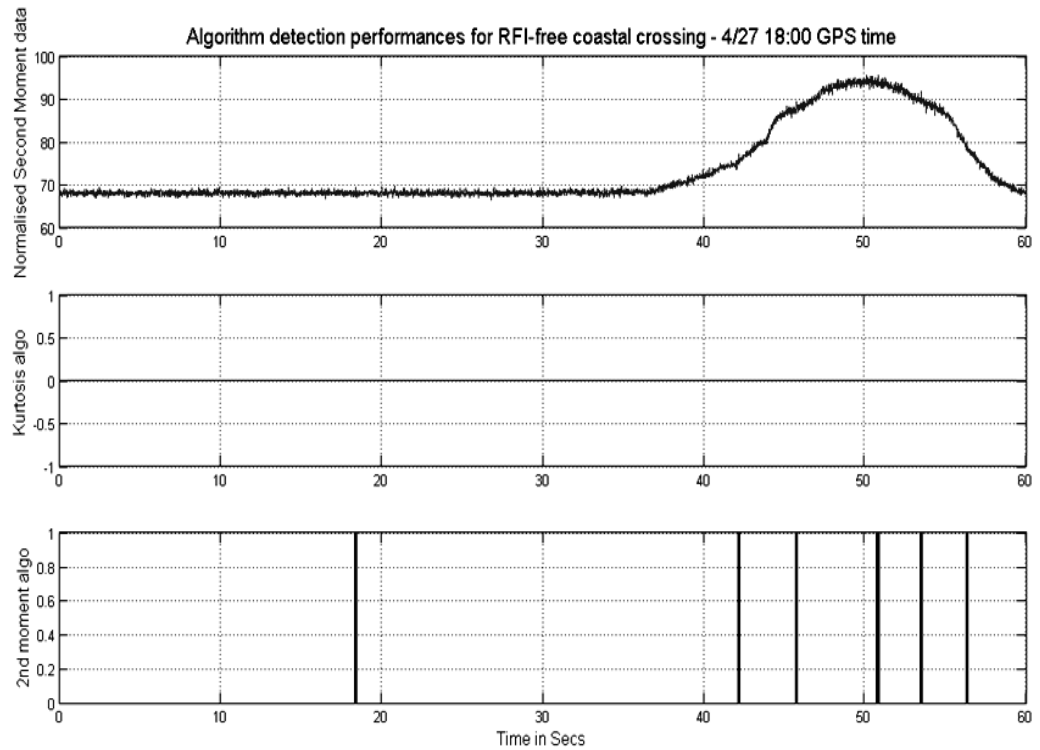


Fig. 2.5: PALS-ADD L-Band radiometer measurements during transition from nadir sky view to BB absorber. (top) 2<sup>nd</sup> moment time series; (center) kurtosis of signal; (bottom) Aquarius RFI detection algorithm

In the figure, the coastal crossing occurs at approximately the 45-s mark. The center panel shows that no RFI was present during this period. The bottom panel indicates a number of RFI false alarms, particularly in the vicinity of the most rapid changes in  $T_b$ . This suggests that the algorithm's detection threshold may need to be varied geographically to make the detectability less sensitive when approaching rapid  $dT_b/dt$  variations near coastlines.

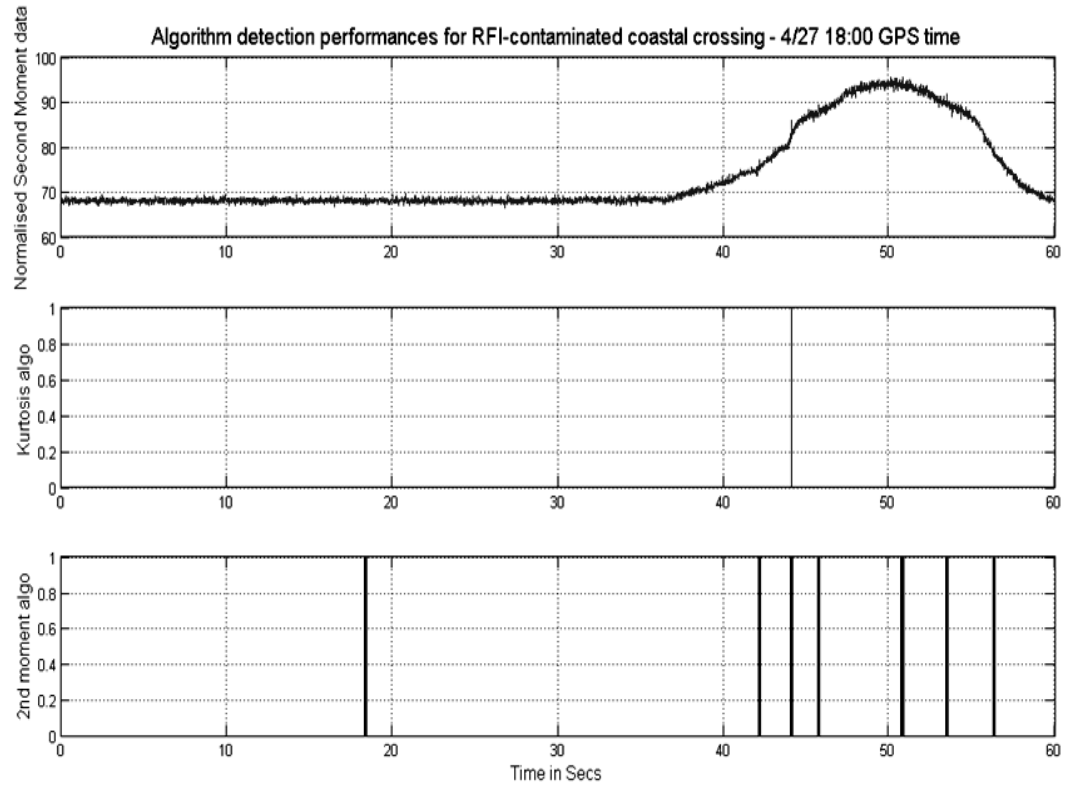


Fig. 2.6: Similar to Fig. 2.5 but with a single RFI event artificially added at the point of maximum time-rate-of-change of  $T_b$  during simulated coastal crossing. (top) 2<sup>nd</sup> moment time series; (center) kurtosis of signal; (bottom) Aquarius RFI detection algorithm.

The next example, shown in Fig. 2.6, starts with the same data set as in Fig. 2.5 and artificially introduces an RFI sample where the  $dT_b/dt$  is highest (at approximately the 44-s mark). This is done to examine the performance of the algorithm in case an RFI source is located on the coastline. From Fig. 2.6, it can be seen that the second-moment detection algorithm successfully identifies the RFI-corrupted sample along with the other false alarms that were also present in Fig. 2.5. This verifies the ability of the detection algorithm to detect RFI with a rapidly changing background  $T_b$ .

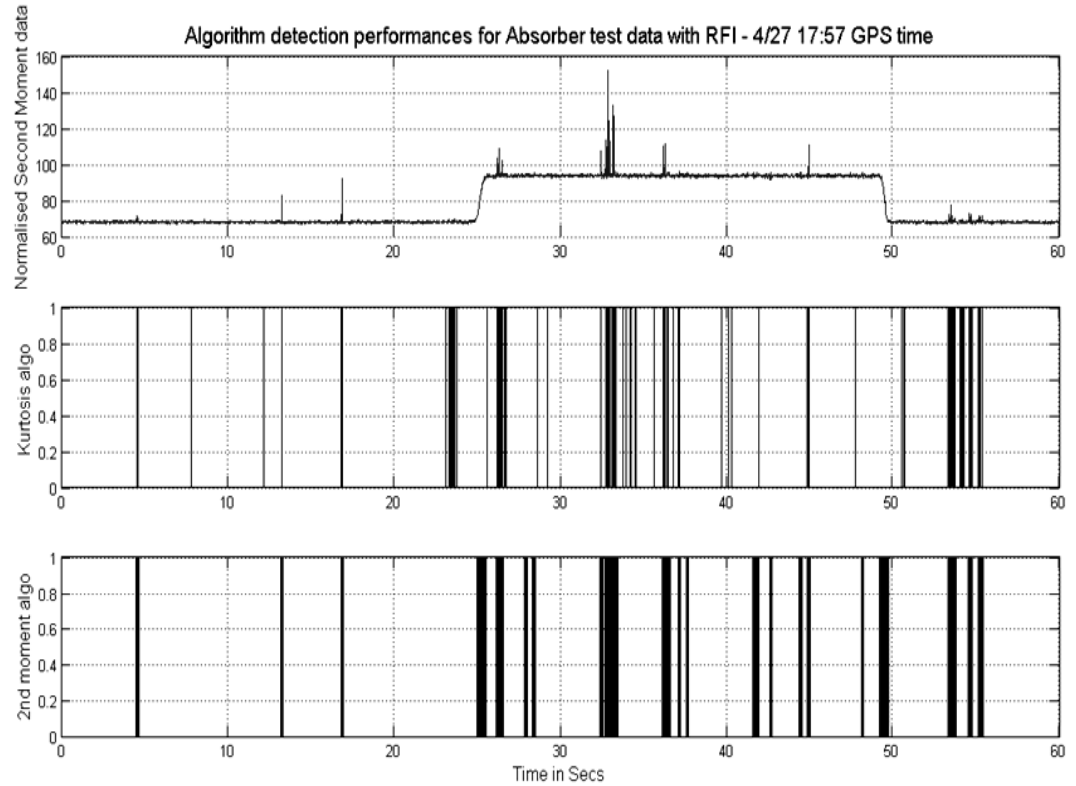


Fig. 2.7: PALS-ADD L-Band radiometer measurements of nadir sky view with BB absorber placed in front of the antenna for a while. (top) 2<sup>nd</sup> moment time series; (center) kurtosis of signal; (bottom) Aquarius RFI detection algorithm

The performance of the Aquarius detection algorithm in the presence of both rapid Tb changes and high levels of RFI was assessed by using the PALS-ADD data set shown in Fig. 2.7. During this particular minute of data, an absorber was temporarily placed in front of the PALS radiometer antenna and then removed. This results in a very high value of  $dT_b/dt$ , as seen in the top panel of the figure near the 25- and 49-s marks. The data were taken during the regular workday at JPL, during which time significant interference is often experienced. The RFI likely entered around the edges of the absorber, which was not tightly joined to the antenna, and into the radiometer. The kurtosis algorithm can be seen to pick up much more RFI than the second-moment detection algorithm in instances

when the RFI perturbations are not easily distinguishable from the NE $\Delta$ T fluctuations of the radiometer. Near the points of abrupt change in the second-moment data, the kurtosis data correctly do not flag the samples as being corrupted by RFI. On the other hand, the second-moment detection algorithm erroneously flags these samples as RFI. It should be noted that such rapid variations in  $T_b$ , as are produced here, would not be produced in the case of Aquarius on orbit, taking into account its antenna beam width and ground track velocity.

## **2.5 Summary and Discussion**

A second-moment detection algorithm is proposed that detects the presence of RFI-contaminated samples in the  $T_b$  data of the Aquarius radiometer. The form of the algorithm could, with some modification, also be applied to other spaceborne radiometers for the removal of RFI. The algorithm works best if raw samples of the  $T_b$  are made at a substantially greater rate than the Nyquist criteria set by the motion of the antenna footprint on the ground. This permits short duration radar interference to be better isolated and detected. For just this reason, a highly oversampled data rate is planned, for example, in the case of the L-band radiometer on the upcoming Soil Moisture Active Passive (SMAP) mission. SMAP is also considering incorporating a digital kurtosis detector into its design for added RFI detection capability, discussed in the next few chapters. On the other hand, the L-band interferometric radiometer on the Soil Moisture Ocean Salinity mission does not significantly oversample its data and, hence, can not incorporate as effective a version of the second-moment detection algorithm [63].

The algorithm is a “glitch detector” in the sense that it compares a sample under test with a local mean obtained from neighboring samples and rejects the sample if it deviates too much from the local mean. The algorithm has four adjustable parameters that control the sensitivity of the detection. The first parameter is  $W_s$ , which defines the averaging window within which the local mean is computed. The mean threshold  $T_m$  then selects uncorrupted Tb samples for calculating the local mean. The third parameter  $T_{det}$  sets the threshold with which the sample under test is compared and RFI is flagged. The last parameter  $W_r$  determines a range in the neighborhood of a contaminated sample within which samples are flagged with RFI even if they themselves do not set off the RFI flag.

Algorithm performance has been characterized by measuring the false-alarm rate while varying the algorithm parameters. The kurtosis of the radiometric pre-detection signal measured by using ADD has been used as a ground truth for flagging RFI. The kurtosis measurement can reliably identify the presence of RFI near the NEAT radiometric noise floor. The performance of the Aquarius detection algorithm is assessed by comparing its results with the results obtained by using kurtosis detection.  $T_{det}$  and  $T_m$  parameters influence the FAR of the detection algorithm the most. RFI detection sensitivity can be increased with a lower  $T_{det}$ . In the absence of RFI, this will result in an increase in the FAR and in the number of data samples mistakenly flagged with RFI. With fewer data samples available, the NEAT will be increased and radiometric sensitivity will be reduced. Thus, the proper setting of parameters such as  $T_{det}$  and  $T_m$  must balance between radiometric sensitivity and RFI detection sensitivity. It should be noted that false-alarm detections will, on average, produce a downward bias in Tb because higher values are preferentially discarded. The resulting bias will increase with decreasing  $T_{det}$ .

Due to similarity with the Aquarius on-orbit sampling data, PALS-ADD ground data were taken as case-study examples to assess the detection algorithm performance. The Aquarius detection algorithm can easily pick up high-level RFI spikes but is less effective when dealing with RFI at or near the NE $\Delta$ T level of the radiometer for individual 10-ms samples. In most cases that are expected to be encountered on-orbit, this limitation will not have a significant impact on its ability to estimate SSS. The nominal integration time on which salinity measurements are based is approximately 6 s, i.e., approximately 600 of the individual 10-ms samples are averaged together. Therefore, the effects of the RFI corruption of a single 10-ms sample are reduced by a factor of 600 due to averaging. If a single 10-ms sample contains RFI at the NE $\Delta$ T level, the corresponding error in the SSS estimate made from a 6-s sample is approximately 0.006 psu [16]. In comparison, the salinity retrieval uncertainty requirement for the Aquarius mission is 0.2 psu—more than one order of magnitude greater than the error due to RFI. It is possible, but unlikely, that many RFI-corrupted samples will be included in a 6-s integration period, due to the azimuthal sweep rate of typical ground scanning radars and the along-track motion of the Aquarius antenna footprint.

Regions near the coast are most likely to have terrestrial radars used for national defense and air-traffic safety. The performance of the detection algorithm in such areas is critical. The second moment has an enhanced susceptibility to erroneous detection of RFI (false alarms) when the  $T_b$  of the scene under observation is changing rapidly, e.g., near a coastal crossing. In spite of a rapidly varying  $T_b$ , the second-moment detection algorithm

successfully detected the RFI that was present. This was tested by using a PALS-ADD data set that simulates the expected rate of change of  $T_b$  when Aquarius would cross over a coastal region. The detection threshold can be adjusted to control the probability of false alarms and reduce sensitivity near coastal crossings, via the adjustable parameters  $T_m$  and  $T_{det}$ . It is anticipated that the Aquarius flight algorithm will have all these parameters dynamically adjusted as a function of the latitude and longitude of the antenna footprint to ensure better detectability.

## **Chapter 3**

### **Microwave radiometer Radio Frequency Interference detection algorithms: A comparative study**

#### **3.1 Introduction**

The design of the Aquarius RFI detection algorithm described in Chapter 2 was limited by the hardware characteristics of the mission. The algorithm was tuned to work with the available hardware resources. The Soil Moisture Active/Passive (SMAP) mission still had hardware flexibility to entertain different options of RFI detection algorithms. The “glitch detector” algorithm though efficient in detecting high level RFI spikes, often missed low-level RFI. Reliable detection of such low level RFI can be much more difficult.

As mentioned briefly in Chapter 1, a number of approaches to low level RFI detection and mitigation have been developed and implemented recently in both hardware and software. The approaches to detection can be generally divided into four classes: Pulse detection compares the power in samples of the signal (*i.e.* its 2<sup>nd</sup> central moment) in the time domain to expected power levels and considers anomalously high values to be caused by RFI [60]. Kurtosis detection evaluates the 4<sup>th</sup> central moment of a signal divided by the square of its 2<sup>nd</sup> central moment and considers as RFI those values which differ from that of a Gaussian distributed signal [32]. Cross-frequency techniques examine the power in the signal as function of frequency [50], and spatial methods consider the behavior of brightness temperature as a function of the spatial location [34].

This chapter considers only kurtosis and pulse detection algorithms. Both of these algorithms have been implemented and tested in the field with a version of the pulse detection algorithm being applied for the Aquarius mission, and the kurtosis detection algorithm being considered for the upcoming Soil Moisture Active/Passive (SMAP) mission.

The pulse detection algorithm can be implemented using either a conventional analog square-law detector or digital signal processing. Kurtosis detection requires specialized detector hardware and/or firmware for implementation [32, 52]. Finer temporal or spectral resolution can be utilized to effectively detect and mitigate RFI. Based on the Analog-to-Digital (A/D) sampling frequency, a large number of samples are accumulated to give a single radiometer integration sample. If the sampling frequency is higher than the required rate, then the radiometer integration sample can be divided into smaller temporal sub-samples giving a better resolution. A temporal sub-sample accumulates fewer discrete samples than are used for the full integration sample. Thus, RFI mitigation can be accomplished by dividing an integration sample into temporal subsamples and removing only the contaminated ones, by dividing an integration sample into spectral subsamples and removing only the contaminated ones, or a combination of both. In general, any of these mitigation approaches can be used with either of the two approaches to detection [31-32, 50, 52, 64].

RFI is often localized in time and/or frequency, relative to the integration times and pre-detection bandwidths over which a spaceborne microwave radiometer acquires its

---

samples of brightness temperature. As a result, the number of subsamples –in both time and frequency– into which an integration sample is divided can affect the detectability of the RFI. In general, the more closely matched the subsample time and frequency intervals are to the characteristics of the RFI, the better the detection and mitigation. However, such matching requires knowledge of the RFI characteristics and can also require fairly finely resolved subsamples which impacts data-rates. Finely resolved temporal subsamples can drive up the data rate of a radiometer. Pulse detection and mitigation implemented in an on-board processor has been demonstrated using terrestrial and airborne radiometers [50], so that increases in data rate may be avoidable. Finely resolved spectral samples can increase both the data rate and the real time signal processing requirements. The work presented here addresses the cost/benefit trade-off between the data bandwidth and the quality of RFI detection and mitigation performance as a function of the detection algorithm. The performance of the detection algorithm is assessed with respect to varying RFI parameters both analytically as well as empirically from field-data.

Section 3.2 discusses details for both the kurtosis detection algorithm and the pulse detection algorithm. The performance of the two detection algorithms is compared under varying conditions, and relevant results are presented in Section 3.3. Concluding remarks are given in Section 3.4.

## **3.2 RFI Detection Algorithms**

### **3.2.1 Kurtosis Detection Algorithm**

Natural thermal emission incident on a space-borne radiometer antenna and the thermal noise generated by the receiver hardware itself are both random in nature. The kurtosis

algorithm makes use of the randomness of the incoming signal to detect RFI. Thermally generated radiometric sources have an amplitude probability density function that is Gaussian, whereas man-made RFI sources tend to have a non-Gaussian pdf [32]. The kurtosis algorithm measures the deviation from normality of the incoming radiometric source to detect the presence of interfering sources.

The kurtosis detection algorithm measures higher order central moments of the incoming signal than the 2<sup>nd</sup> central moment measured by a square-law detector in a total power radiometer. The n<sup>th</sup> central moment of a signal is given by,

$$m_n = \langle (x(t) - \langle x(t) \rangle)^n \rangle \quad (3.1)$$

where  $x(t)$  is the pre-detection voltage and  $\langle \cdot \rangle$  represents the expectation of the measured signal. The kurtosis is the ratio of the 4<sup>th</sup> central moment to the square of the 2<sup>nd</sup> central moment, or

$$\kappa = \frac{m_4}{m_2^2} \quad (3.2)$$

The kurtosis equals three when the incoming signal is purely Gaussian distributed and it in most cases deviates from three if there is a non-normal (typically man-made) interfering source present. The kurtosis statistic is independent of the 2<sup>nd</sup> central moment of the signal, i.e., the kurtosis value is not affected by natural variations in the brightness temperature of the scene being observed.

The kurtosis estimate itself behaves like a random variable since it is calculated from a finite sample set [65]. Estimates of the kurtosis have a standard deviation associated with

them, and there is a corresponding kurtosis threshold for detecting RFI. If the sample size is sufficiently large, the kurtosis estimate exhibits a normal distribution.

### **3.2.1.1 Agile Digital Detector (ADD)**

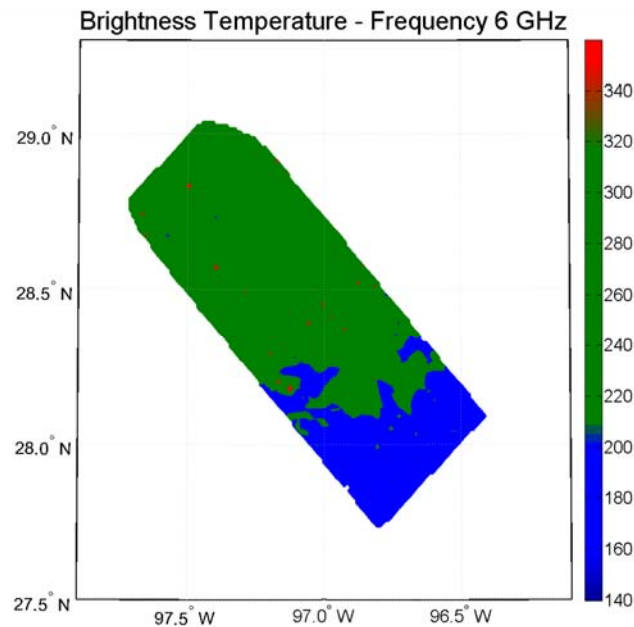
The kurtosis detection algorithm is implemented using the ADD. The ADD is capable of performing standard functions of a conventional analog detector as well as measuring higher order statistics for removal of low-level RFI [32].

ADD's basic design consists of an analog-to-digital converter (ADC) followed by 8 to 16 sub-band digital FIR filters implemented on an FPGA. These filters provide spectral sub-sampling of the incoming signal. The output signals from the filters are then accumulated over a temporal sub-sampling period to measure either the probability distribution function of the signal or its first four non-central moments.

Due to digitization effects such as rounding, truncating, quantization bin size, ADC span etc., the expected value of the kurtosis is shifted slightly, but these effects can be corrected for in post-processing [66]. The simulation results used in the algorithm comparisons presented in Section 3.3 assume no quantization effects. ADD has been deployed in many field campaigns, with successful results [32, 61, 64].

Fig. 3.1 indicates RFI detection using the kurtosis statistic obtained from ADD installed in parallel with the standard back-end detector sub-system of the stepped-LO C-Band channel of the NOAA/ETL Polarimetric Scanning Radiometer (PSR). PSR employed a frequency scanning technique that covered a range of approximately 5.5 GHz to 7.7 GHz with a channel resolution of 100 MHz. The figure represents data over the Gulf of Mexico measured at approximately 6.0 GHz. The transition at the coastline from land to

water is evident in the brightness temperature image (top figure) because of the high contrast in their emissivity. Discrete “hot spots” in the brightness temperature image are likely a result of RFI sources on the ground. The value of the kurtosis for natural thermal emission is approximately 3 and does not change with brightness temperature. For example, the transition from high land to low water brightness temperature has no effect whatsoever on the kurtosis image (bottom figure). The kurtosis of non-thermal RFI sources, on the other hand, is markedly different and stands out prominently in the image. Assuming a pulsed-sinusoidal type of RFI, kurtosis higher than 3 represents RFI with a duty-cycle less than 50% and kurtosis less than 3 represents RFI with a duty cycle more than 50%. The duty-cycle is measured relative to the radiometer integration period.



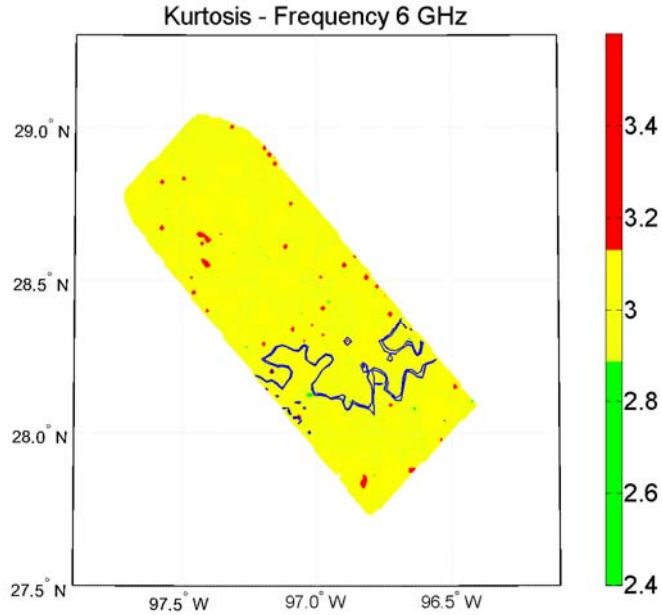


Fig. 3.1: Images of 6.0 GHz horizontally polarized brightness temperature (top) and kurtosis (bottom) during an overpass of the Gulf coast near Galveston, TX. The bottom plot of kurtosis has a blue coastal map added over it showing the insensitivity of kurtosis to brightness temperature changes.

### 3.2.2 Pulse Detection Algorithm

The Pulse detection algorithm theoretically evaluated here is based on the “glitch-detector” described in chapter 2 and [64, 67-68]. The algorithm applies a threshold detector to the  $T_b$  or power measurements obtained after integrated  $N$  time domain samples. These time-domain samples are independent zero mean Gaussian random variables (in the absence of RFI), which are then squared and summed to form a power measurement that is a scaled chi-squared random variable with  $N$  degrees of freedom. In the presence of RFI, the sum is a scaled non-central chi-squared variable with  $N$  degrees of freedom, where the non-centrality parameter can be calculated based on the characteristics of the RFI source [45]. The radiometric integration period of  $N$  samples is

further resolved into  $R$  sub-sampling periods of  $Q$  samples each ( $N=QR$ ), giving  $R$  chi-squared random variables. RFI is detected if the maximum of this set of  $R$  exceeds a defined threshold [69].

### 3.3 Performance Comparison of RFI Detection Algorithms

#### 3.3.1 RFI Model and Area Under Curve (AUC) parameter

In order to characterize and compare the performance of the detection algorithms, the RFI is modeled as a radar-type pulsed sinusoidal signal. Based on this RFI model, detection statistics such as False Alarm Rate (FAR) and Probability of Detection (PD) are used to generate receiver operating characteristics (ROC) for both detection algorithms. The ROC curves are then used to parameterize the detection performance of the algorithm.

##### 3.3.1.1 Modeling RFI

Air-traffic control radars and early warning radars are expected to be sources of RFI at L-Band [44]. In order to compare and contrast the performance of the two detection algorithms, a pulsed-sinusoidal signal is considered as the model for the RFI source. The incoming radiometric signal can be written as,

$$x[n] = \begin{cases} a[n] & m \leq n \leq M \\ a[n] + A \sin(2\pi f_o n) & otherwise \end{cases} \quad (3.3)$$

where  $a$  is a normally distributed random variable with mean  $\mu$  and standard deviation  $\sigma$  (i.e.  $a \sim N(\mu, \sigma)$ ),  $A$  is the amplitude of the pulsed-sinusoid signal with frequency  $f_o$ , and  $M$  is the total radiometer integration period in units of samples. The duty cycle of the sinusoidal pulse is therefore given by  $d=m/M$ . For simplicity, the frequency  $f_o$  is assumed to be uniformly distributed between 0 and  $\frac{1}{2}$  where  $f_o = 0$  corresponds to a DC signal and

$f_0 = 1/2$  corresponds to a signal oscillating at the Nyquist rate. The frequency of each individual pulse is kept constant.

The phase of the pulse onset is assumed to be constant at 0. Since the power and duty-cycle characteristics of RFI are not affected by the phase of the signal, a phase of 0 is a valid assumption. It is also assumed that the RFI occurs at the start of the radiometer integration period. Thus, RFI pulse arrival is considered to be synchronous with the start of both the pulse and the kurtosis detection sub-sampling periods. If the pulse-width of the incoming RFI signal is considerably smaller than the integration period, the duty-cycle or power measured would not change even if the pulse is asynchronous with the start of the sub-sampling period. Thus the above assumption is valid for low duty-cycle RFI. At L-Band, typical radar signals that would cause RFI have a pulse width of 2-150  $\mu$ s with a PRF of approximately 300Hz [44]. Such signals result in a duty cycle of 0.2 to 15% with a 1ms radiometer integration period. For high duty cycle signals, model predictions would be slightly different because in this model the pulse-width of the RFI is considered to be an integer multiple of the pulse detection sub-sampling period.

### **3.3.1.2 FAR and PD of detection algorithms**

The two RFI parameters that vary in the RFI model presented in the previous section are its duty cycle and amplitude (or power). These parameters significantly affect the detection performance. The behavior of both detection algorithms in the presence of pulsed-sinusoidal RFI has been extensively analyzed previously [31, 45]. The kurtosis detection algorithm is extremely sensitive at low duty cycles. When the pulsed-sinusoidal RFI has a 50% duty-cycle, the detection algorithm has a blind-spot since the

kurtosis value is three. This may not seem to be a problem since most radar signals have a very low duty-cycle, but can become important when time sub-sampling is utilized.

For equal thresholds above and below the kurtosis mean, the FAR of the kurtosis detection algorithm is given by [11] [31]

$$Q_k(z) = \left( 1 - \operatorname{erf}\left(\frac{z}{\sqrt{2}}\right) \right) \quad (3.4)$$

where  $z$  is the normalized magnitude of the standard deviation of the kurtosis (i.e. the threshold is set at  $3 \pm z\sigma_{R0}$ , where  $\sigma_{R0}$  is the standard deviation of RFI free kurtosis), beyond which a sample is flagged as being corrupted by RFI.

In practical implementations of the detection algorithm the incoming signal is divided into temporal sub-samples, or spectral sub-samples, or both (Section 3.2.1.1) before calculating the kurtosis statistic [32]. If any sub-sample is flagged then it is discarded. In order to compare the kurtosis algorithm with other detection algorithms, an entire radiometer integration period is assumed to be corrupted by RFI if any single sub-sample is flagged. Eqn. (3.4) can be rewritten to calculate the FAR for detection of the whole temporal/spectral grid of sub-samples within the integration period, as given by

$$Q_k^{noRFI}(z) = 1 - (1 - Q_k(z))^{XR} \quad (3.5)$$

where,  $z$  is the normalized standard deviation magnitude of the kurtosis (i.e. the threshold is set at  $z\sigma_{R0}$ , where  $\sigma_{R0}$  is the standard deviation of RFI free kurtosis),  $R$  is the number of temporal sub-sampling periods within an entire integration period and  $X$  is the number of spectral sub-bands.

To simplify the analysis, pulsed-sinusoidal RFI is assumed to be located fully within a single frequency channel of the kurtosis algorithm when spectral sub-banding is used; this improves detection performance since the RFI signal-to-noise ratio is larger in this channel. Temporal sub-sampling also improves detection performance since it reduces the interval over which the RFI power is averaged and hence increases the relative RFI power measured. The analysis allows an RFI pulse to be spread over multiple temporal sub-samples if the sub-sampling period is smaller than the RFI pulse-width. Sub-sampling and sub-banding reduce the number of independent samples used to calculate kurtosis, as a result of which slight skewness is introduced to the normal distribution of the kurtosis statistic. However this skewness is not modeled in what follows. The probability of detection (PD) for the kurtosis algorithm for a single sub-sampling period and a single frequency channel can be calculated if the duty-cycle and power of the RFI signal are known. The PD was given by [31] and is repeated here

$$Q_{\kappa}^{pulsed\text{-}sin\text{ RFI}}(z) = \left( 1 \mp \operatorname{erf} \left( \frac{R_{th} - \bar{R}(S, d)}{\sqrt{2}\sigma_R(S, d)} \right) \right) \quad (3.6)$$

where  $S$  is the relative power of the pulsed-sinusoidal RFI to the thermal signal,  $d$  is the duty-cycle of the RFI,  $\bar{R}$  and  $\sigma_R$  are the mean and standard deviation of kurtosis for a pulsed-sinusoidal RFI with relative power  $S$  and duty cycle  $d$  given in [31],  $R_{th} = 3 \pm z\sigma_{R0}$  is the kurtosis threshold and  $\sigma_{R0}$  is the standard deviation of RFI free kurtosis. As mentioned above, an integration sample is divided into finer temporal and spectral resolution sub-samples, thus creating a grid. In order to detect RFI, the kurtosis with the maximum deviation from 3 within a temporal and spectral sub-sampling grid is

measured. If that particular kurtosis sub-sample is above  $3 + z\sigma_{RO}$ , or below  $3 - z\sigma_{RO}$  then the grid is considered to be corrupted by RFI, and hence the whole integration sample is flagged as being corrupted by RFI. Thus the final probability of detection is obtained by taking the maximum kurtosis deviation among the set of frequency and time resolved kurtosis values.

The pulse detection algorithm performs best when the sub-sample integration time is matched to the pulse-width of the RFI. The performance degrades as that sub-sampling time increases relative to the pulse-width. For time intervals containing RFI pulses, the power in the incoming signal is a non-central Chi-square random variable with the non-centrality parameter determined by the power and duty cycle of the RFI. The PD of the pulse detection algorithm can be calculated using the right-tail cdf of a non-central chi-squared random variable given in [45] with non centrality parameter

$$\lambda_{nc} = \sum_{n=m}^{m+d} A^2 \sin^2(2\pi f_o n) \quad (3.7)$$

where  $A$  is the amplitude of the pulsed-sinusoid signal with frequency  $f_o$  and  $d$  is the pulse-width of the RFI, determining the duty cycle.

### 3.3.1.3 Area Under Curve (AUC) parameterization

The receiver operating characteristic (ROC) of any detection algorithm is a graphical plot of the probability of detection (fraction of true positives) versus the false alarm rate (fraction of false positives). Fig. 3.2 gives the ROC curves of the kurtosis and pulse detection algorithms for RFI with  $M=240,000$ ,  $N=200$ ,  $d=800$  (a duty cycle of 0.33% relative to the total integration period) and an average power level of 0.5 NE $\Delta$ T. In Fig.

3.2, two versions of the ROC curve for the kurtosis algorithm are shown; one curve represents the full-band kurtosis with no temporal sub-sampling and the other assumes 16 spectral sub-bands are available and the data are sub-sampled at a rate that is a quarter of the total integration period. The third curve indicates the pulse detection algorithm, with the total integration period divided into 1200 sub-sampling periods. In general, better detection algorithms correspond to a ROC curve that is closer to the upper left corner of the PD vs. FAR space.

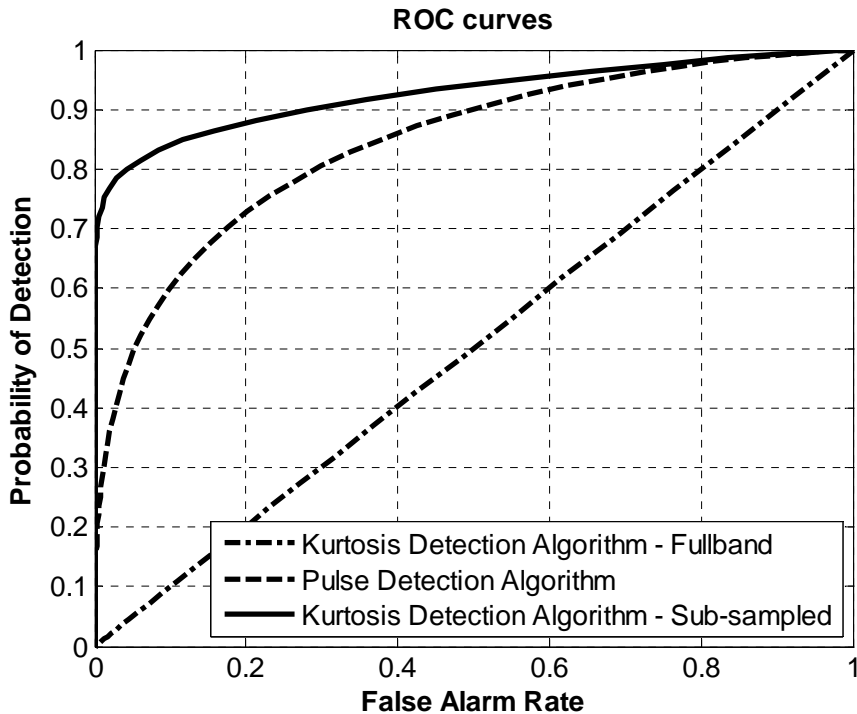


Fig. 3.2: Plot of the ROC curves for three RFI detection schemes (Pulse-detection algorithm, Fullband kurtosis detection algorithm, Sub-sampled kurtosis algorithm) for a 0.33% duty-cycle pulsed-sinusoid RFI with a 0.5 NEAT power level.

In order to estimate the relative performance of the detection algorithms under various conditions, the normalized area under the ROC curve (AUC) is used as a performance metric. An ROC curve that runs diagonally across the PD vs. FAR space with a positive slope represents the case of a detector that doesn't use information of the signal at the

antenna. The AUC parameter is scaled so that such a case has a performance metric of 0, whereas an AUC of 1 indicates an ideal detector, with zero probability of false alarms or missed detections. In Fig. 3.2, the full-band kurtosis algorithm (with a 0.33% duty cycle and 0.5 NE $\Delta$ T power level) has an AUC of 0.0012, whereas the sub-band kurtosis algorithm has an AUC of 0.85 and the pulse detection algorithm has an AUC of 0.69. These values suggest that the sub-band kurtosis as configured here is the best algorithm for this particular type of RFI. It should be noted that even though one algorithm performs better than the other, the performance might still not be optimal with the current configuration for this type of RFI.

### **3.3.2 Comparison with pulse detection algorithm under optimum resolution**

The pulse detection algorithm is considered to be operating under ideal detection conditions when the pulse duration of a pulsed sinusoid RFI is perfectly matched to its sub-sampling integration time. The performance of the kurtosis algorithm under various spectral and temporal sub-sampling schemes is compared to such an ideal detector. For comparison, a digital kurtosis detector similar to ADD is considered since sub-banding can be easily implemented. An analog kurtosis detector such as DD is equivalent to a full-band digital kurtosis detector with half the data-rate. We consider  $M=240,000$  (for example, a digitizer operating at 240MHz with a radiometer total integration time of 1ms.), the pulse width of RFI is  $m=400$  ( $\sim 1.66 \mu\text{s}$  at 240 MHz ) for radar signals and the pulse detection algorithm is nearly optimally matched with  $N=200$  raw samples in one sub-sample period. The  $1.66 \mu\text{s}$  pulse width used in the analysis below is similar to ground-based radars such as the ARSR-1,2 and 3. Newer radars such as the ARSR-4 have a typical pulse-width of  $100 \mu\text{s}$ .

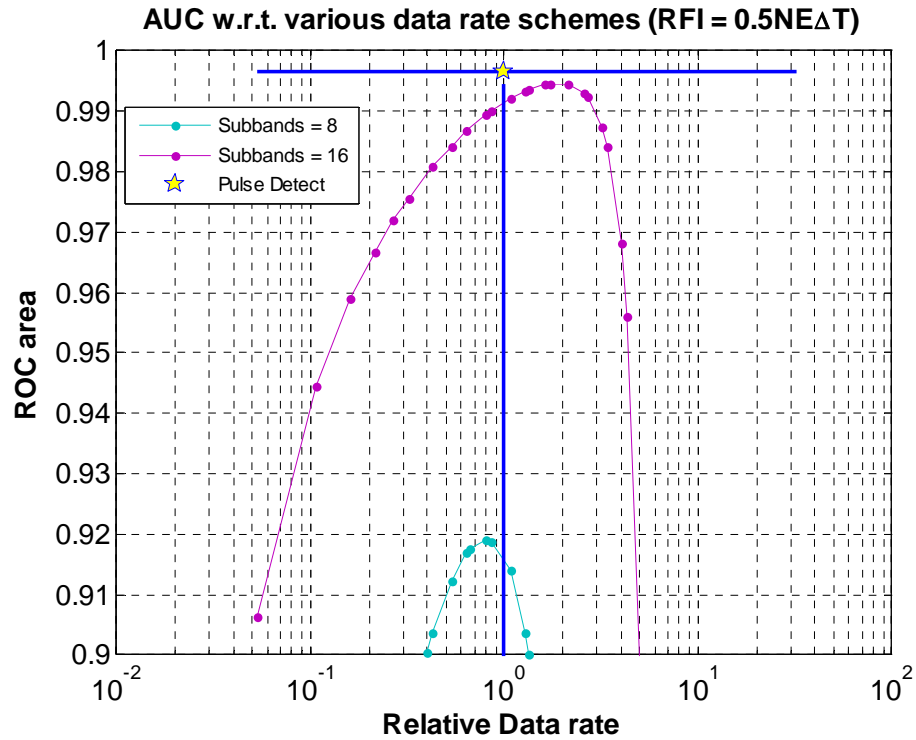
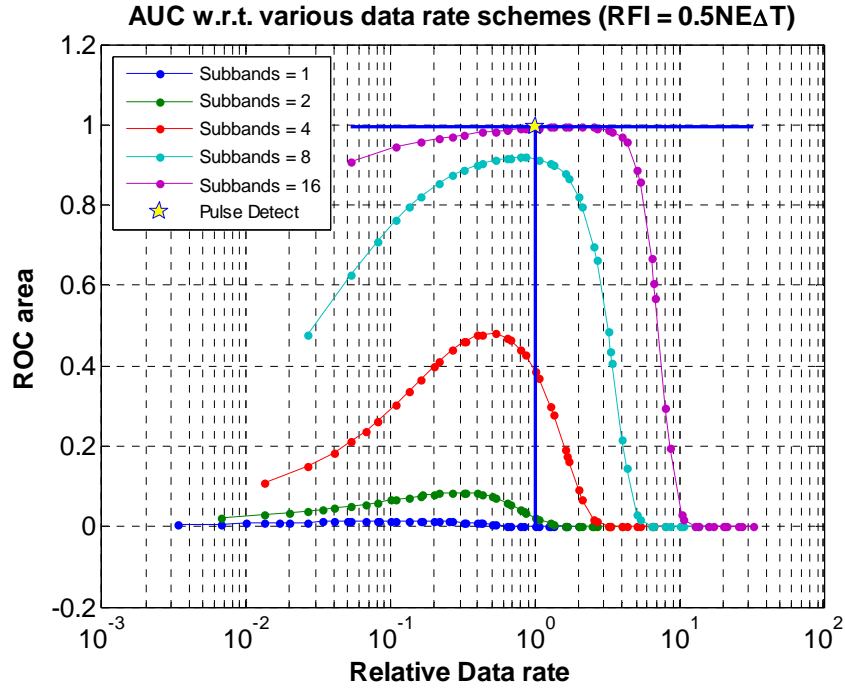
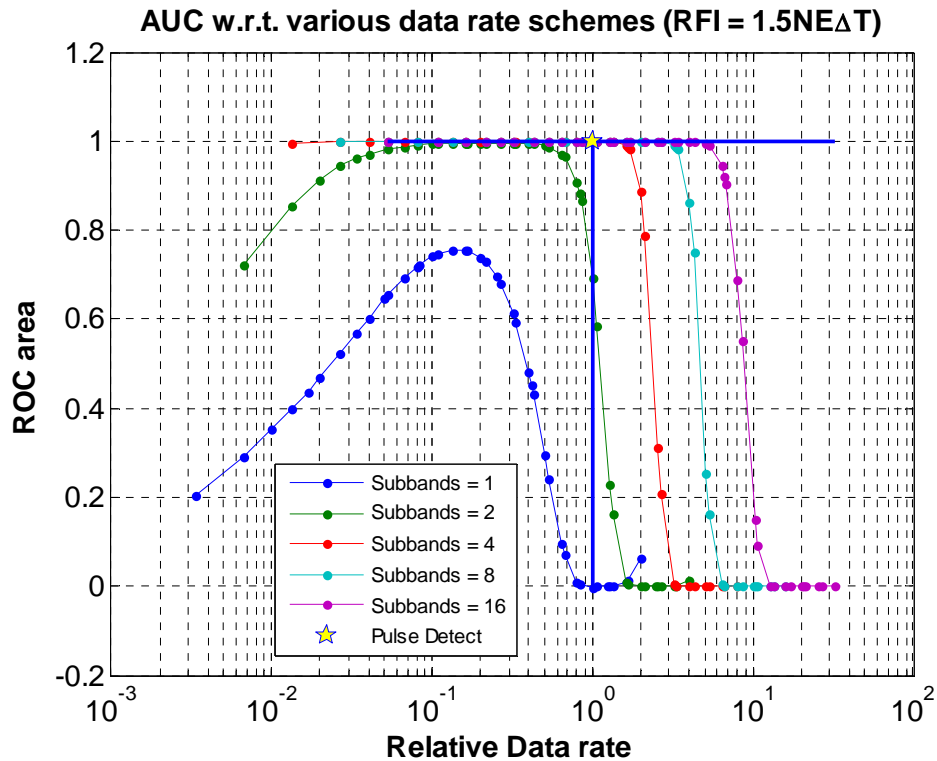


Fig. 3.3: (a) Plot comparing the ROC area for the kurtosis algorithm as a function of relative data rate and number of sub-bands with the matched pulse detection algorithm (star) (b) Magnified plot indicating ROC area of the kurtosis algorithm near matched pulsed detection algorithm (star) (RFI power = 0.5NE $\Delta$ T). The relative data rate is with respect to the ideally matched pulse detector. Heavy blue lines represent data rate and ROC area values for the matched pulse detector.

Fig. 3.3 compares the AUC of the kurtosis algorithm with a matched pulse detection algorithm as a function of the relative data rate and the number of sub-bands. The data-rate is an important factor when considering algorithm performance. Even though the pulse detector performs extremely well when matched with the RFI pulse-width, the resulting data-rate (when fully down-linked) due to such finely resolved sub-samples for detection and mitigation might be impractical in terms of downlink bandwidth. For RFI mitigation purposes, within a sub-sampling period the pulse detection algorithm needs to send only one piece of information, the power ( $2^{\text{nd}}$  moment) of the incoming thermal emissions. On the other hand, for a particular temporal sub-sampling period the kurtosis detection algorithm needs to send the first four moments to calculate the kurtosis ratio. It is possible to just send the second and fourth moments if the hardware can ensure zero mean and skewness through some feedback mechanism. However, for general kurtosis systems four pieces of information are sent for each sub-band used by the kurtosis. As a result, for the same temporal period the kurtosis algorithm has a higher data rate. The data-rate for the kurtosis algorithm decreases due to having a much longer sub-sampling period compared to the pulse detection algorithm. The relative data rate in Fig. 3.3 is a combined result of these two competing factors (more sub-bands with four moments vs longer integration period compared to the pulse detection algorithm). The relative data rate can be represented in terms of number of sub-bands ( $N$ ), pulse detection sub-sampling period ( $\tau_p$ ) and kurtosis sub-sampling period ( $\tau_k$ ) as  $4N*\tau_p/\tau_k$ .

As shown in Fig. 3.3, the matched pulse detection algorithm (relative data-rate = 1.0) has an almost ideal detection performance ( $AUC = 1$ ) for an RFI signal with power 0.5 times the NE $\Delta$ T of the radiometer. The kurtosis detection algorithm with 16 sub-bands has

nearly comparable performance, with an AUC of 0.9 or greater at a significantly lower data-rate than the fully down-linked pulse detector. As the sub-sampling period decreases, the kurtosis detection algorithm performs more poorly, even though the relative RFI to signal power level is higher. This is due to the fact that as the sub-sampling period becomes shorter, the pulse-width approaches the 50% duty-cycle. At higher RFI power levels, the kurtosis detection algorithm performs nearly as well as the pulse detection algorithm. Fig. 3.4 is similar to Fig. 3.3, except that the RFI power is 1.5 times the  $NE\Delta T$ . When using sub-banding, there is a larger optimum region of operation of the kurtosis detection algorithm for relatively lower data-rates.



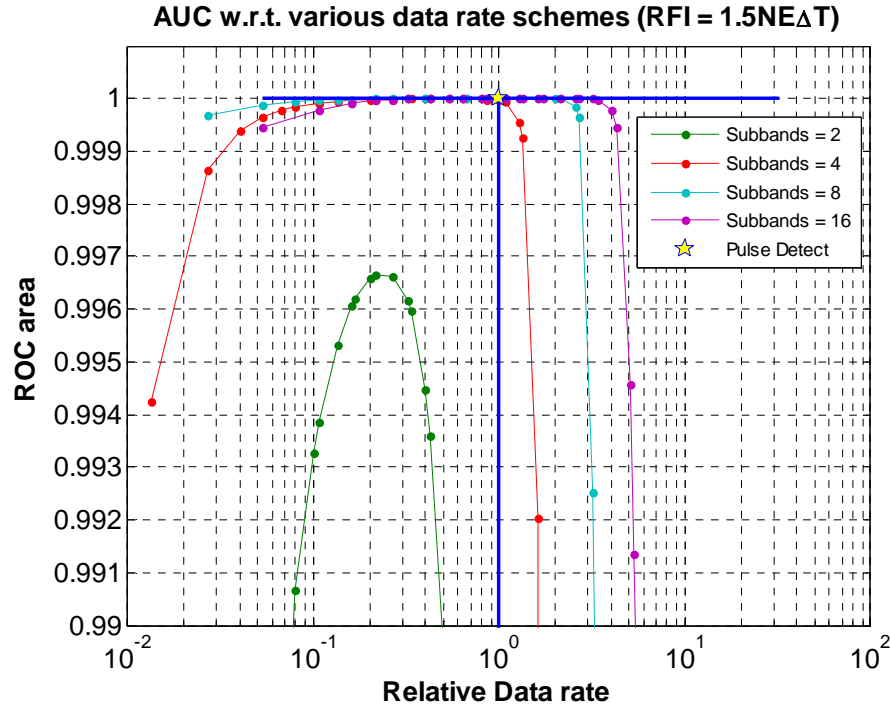


Fig. 3.4: Same as Fig. 3.3 except (RFI power = 1.5NEΔT)

### 3.3.3 Algorithm comparison under varying RFI conditions

Both types of detection algorithm have an optimum operating point in terms of sub-sample integration time based on certain expected properties of RFI. Considering a typical RFI pulse-width of  $d=400$  ( $1.66 \mu\text{s}$ ), the pulse detection algorithm with sub-sampling period  $N=200$  outputs samples at 1200 times the radiometer integration period for assumed sampling conditions. Similarly, based on Section 3.3.2, we find the peak performance for the kurtosis algorithm exists for 16 sub-bands and a sub-sampling period that is  $1/4^{\text{th}}$  the radiometer integration period. This yields a data-rate almost 5 times lower than the pulse detection algorithm, when compared to storing second moment data at a rate 1200 times the nominal radiometer integration period. If on-board mitigation is implemented or the pulse detector is configured at a slower rate, the data rate reduction becomes less significant.

Even though the detection algorithm parameters are set with respect to expected RFI characteristics, it is necessary to analyze their performance with respect to varying RFI characteristics. Fig. 3.5 indicates the difference in performance between the two detection algorithms in terms of AUC with respect to different RFI power levels and duty-cycles. If the AUC for both algorithms is below 0.5, then the detection performance is considered poor enough that the difference can be ignored.

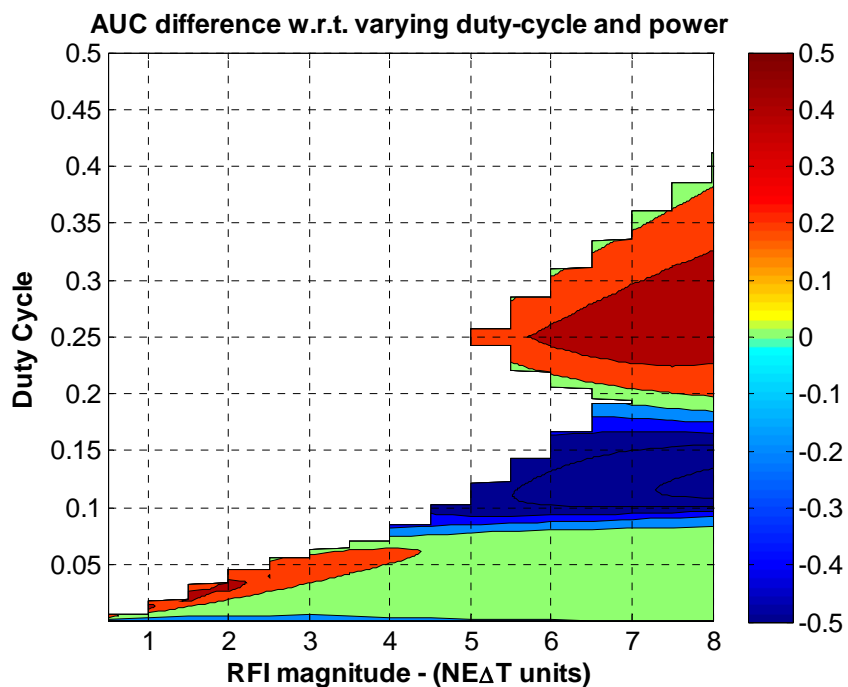


Fig. 3.5: Plot indicating difference between AUC of the pulse detection algorithm and kurtosis detection algorithm (16 sub-bands and 4 sub-sampling periods) for different RFI pulse widths and duty cycles (Blank areas indicate detection performance of both algorithms is poor, yellow to red areas indicate better performance by the kurtosis detection algorithm and light blue to dark blue areas indicate better performance by the pulse detection algorithm and green areas indicate similar performance by both algorithms)

In Fig. 3.5, a positive value indicates that the kurtosis algorithm performs better and a negative value indicates better pulse detection algorithm performance. The pulse detection algorithm works better when the RFI is optimally matched to its sub-sampling period, as seen for extremely low duty cycles, though the difference is not large. For low-

power and low duty-cycle, the kurtosis algorithm is more sensitive to RFI whereas for higher duty cycle signals (continuous-wave) the performance of the pulse detection algorithm degrades significantly as the power decreases. The range of duty cycle of interest for terrestrial radars is approximately 0 – 0.03 (0-3%). Within this range the kurtosis detection algorithm shows a significant advantage below 2 NE $\Delta$ T RFI magnitude, but no detection advantage over 4NE $\Delta$ T. The kurtosis algorithm with sub-banding does however retain a mitigation advantage, especially at high duty-cycles with respect to the radiometric integration period.

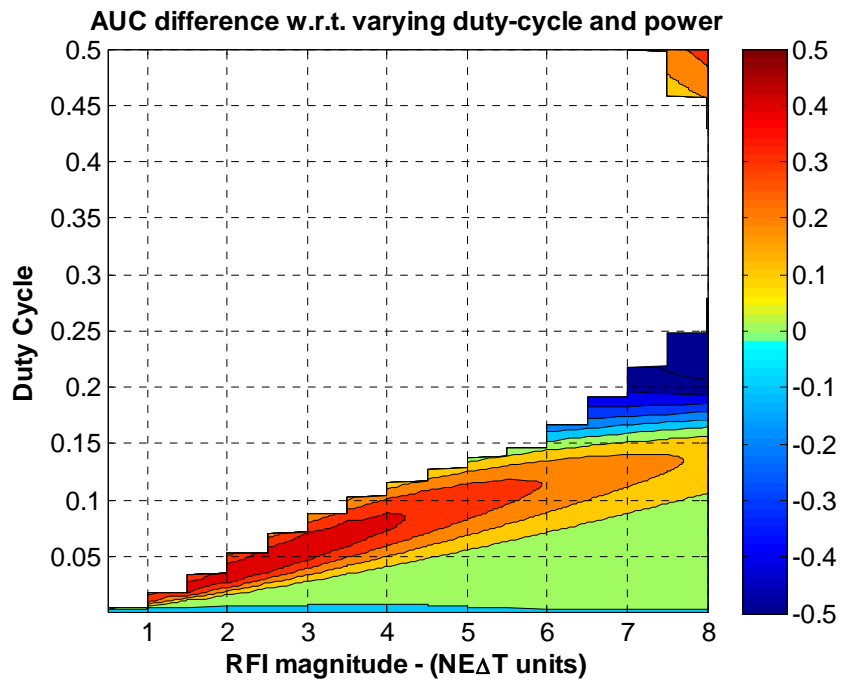


Fig. 3.6: Same as Fig. 3.5 except that the kurtosis detection algorithm has 16 sub-bands and 2 sub-sampling period

Fig. 3.5 indicates a dip around the 0.1 – 0.15 (10-15%) duty-cycle region where the performance of the kurtosis algorithm degrades significantly. This is due to the fact that the sub-sampling period approaches the 50% duty-cycle of the pulsed-sinusoid RFI. The 50% duty-cycle blind spot can be avoided by combining multiple sub-samples in ground

post-processing and recalculating the kurtosis ratio. Thus the detection performance of the kurtosis algorithm can be improved. Fig. 3.6 indicates the AUC difference when the kurtosis algorithm combines two sub-sampling periods to a new sub-sampling period that is 1/2 the radiometer integration period. As may be observed in the figure, the blind-spot present in Fig. 3.5 is easily removed in Fig. 3.6. Since this processing is performed after downloading, the regions of high sensitivity in Fig. 3.5 are not lost.

In both of these cases, other algorithms may also become effective for larger duty cycle pulses, particularly cross-frequency or “peak-picking” approaches. Such algorithms also require an a-priori estimate of the system brightness temperature, but such estimates are available by excluding the largest brightnesses when computing the mean of the remaining channels. Future work will compare performance with these algorithms; here the focus is on the pulse and kurtosis algorithms for low duty cycle pulses.

### **3.4 Summary and Discussion**

The pulse detection algorithm and the kurtosis algorithm are two RFI detection techniques developed for microwave remote sensing. The pulse detection algorithm operates on the principle of a simple threshold operation of the radiometric data. This technique requires a high integration rate and short integration period to optimally identify and mitigate short radar-like RFI pulses. The kurtosis detection algorithm detects RFI based on the Gaussian statistics of the incoming thermal signal. The kurtosis algorithm has been successfully implemented and tested by the ADD system developed by University of Michigan that uses spectral sub-bands.

One of the advantages of the pulse detection algorithm is a relatively simple implementation since it needs to measure only power. The digital kurtosis algorithm needs to record the first four moments of the signal, and the implementation can be slightly more complicated if sub-banding filters are used as well.

The detectability of both algorithms is characterized using the AUC for pulsed-sinusoid type of RFI signals. Though AUC's give an indication of the detection performance, the final PD and FAR are determined by a single threshold value. Kurtosis is independent of variations in power and hence RFI, and as a result the threshold value is easily set. The pulse detection algorithm, on the other hand, determines the threshold value based on the incoming data itself. Thus the threshold might be corruptible by natural brightness temperature variations or worse, RFI, especially for sub-samples that are longer in time.

Results indicate that the pulse detection algorithm has superior detectability when its sub-sample integration time matches the RFI pulse-width. If no flagging or on-board mitigation are used, the pulse detection algorithm requires a relatively high integration rate and bandwidth for it to work effectively as an optimal detector and mitigator for very low duty-cycle RFI. However it provides complementary performance to the kurtosis method in some cases and, if implemented as an on-board flag, can provide useful information without impacting the system data rate. The kurtosis algorithm can achieve nearly the same performance in terms of RFI mitigation at a considerably lower relative data rate, assuming all the sub-samples are down-linked in the pulse detection algorithm. Since the pulse detection algorithm works best when the sub-sampling period is exactly matched to the radar pulse-width, the algorithm gains no real advantage by recombining the sub-samples to improve detection performance, except in the cases where pulse-

widths are longer than the sub-sample period. The kurtosis algorithm with subbanding provides more robust detection when dealing with varying RFI duty-cycle and power. The sub-sampling periods of kurtosis can be combined to remove any blind-spots and improve detectability by operating at the optimum accumulation period for a given RFI signal.

The performances of both the algorithms have been empirically compared using data obtained from a field campaign at JPL [69]. A table from [69] prepared by NASA Goddard is shown below. The table indicates %RFI missed for various temporal sub-sampling periods, for varying strengths of RFI. The kurtosis algorithm represented by the table is not spectrally divided and is a slightly modified version of the algorithm described in section 3.2.1. Results confirm that for lower sub-sampling periods the pulse detection algorithm is better, provided high data-bandwidth is available or mitigation is done on-board. The observed RFI had short-pulsed characteristics which is why the pulse-detect performed better when its sub-sampling period was close to being optimally matched. As the sub-sampling period increases, the kurtosis algorithm performs better with a much lower data-rate.

Table 3.1  
 Results comparing Pulsed-detect to Kurtosis  
 (courtesy P.Mohammed and J.Piepmeyer [69])

Sampling time ( $\mu\text{s}$ )	% missed RFI i.e. $\Delta T_B > 0$		% missed RFI with $\Delta T_B > \text{NEAT}$		% missed RFI with $\Delta T_B > 2 \times \text{NEAT}$	
	Pulse	Kurtosis	Pulse	Kurtosis	Pulse	Kurtosis
4	0.0118		0.0342		0	
8	0.125		0.290		0.00645	
16	0.290		4.62		0.122	
32	0.971		32.8		8.13	
64	1.79		50.2		15.5	
128	3.05		52.9		6.44	
256	5.47	5.60	37.3	37.3	1.35	1.60
512		10.3		11.6		0.581
1024		18.9		5.37		0.353
2048		33.8		2.44		0.287
4096		55.8		1.62		0.304
8192		80.34		1.59		0.351
16384		90.03		2.57		0.521

## **Chapter 4**

### **An Improved Radio Frequency Interference model: Reevaluation of the kurtosis detection algorithm performance under central limit conditions**

#### **4.1 Introduction**

The SMAP mission is implementing the kurtosis detection algorithm as its primary RFI mitigation option. The kurtosis detection algorithm has been successfully tested and proven in many field-campaigns [32, 41, 59, 61, 64]. These campaigns demonstrate the capability of the kurtosis detector in detecting RFI around the noise-level of the radiometer.

This chapter discusses the performance of the kurtosis detection algorithm when simultaneously observing many RFI-sources. Considering the relatively high altitude of satellite missions compared to airborne missions, it is possible that many sources may exist in the large foot-print of the radiometer antenna, e.g. in densely populated areas. Since the kurtosis detector works on the principle of observing a Gaussian distributed signal, the effects of central-limit like conditions are considered here. The next section presents a brief description of the kurtosis detection algorithm and blind-spots associated with the detection algorithm. Section 3 introduces a new RFI model to take into account multiple sources and the results are presented in section 4. Experimental validation of the multiple-source model is in the following section. Summary and conclusion is discussed in the last section.

## 4.2 Kurtosis Algorithm and Issues

As mentioned in previous chapters, the kurtosis RFI detector identifies RFI in the amplitude domain or statistical domain by measuring the higher-order moments of the incoming pre-detected voltage signal from a radiometer [32]. The detection algorithm is independent of the incoming power, hence  $T_b$  variations, and is an effective tool for detecting low-level RFI compared to other detection algorithms [69].

Studies on the kurtosis statistic have found the algorithm to be extremely sensitive to low duty-cycle pulsed RFI and less sensitive to continuous-wave (CW) type RFI [31, 51]. For a pulsed-sinusoid type RFI, the kurtosis detection algorithm has a blind-spot for a 50% duty-cycle signal. Alternate higher-order algorithms like [54] have been proposed to supplement the kurtosis algorithm.

Most field campaigns at L-band have shown RFI to be of a pulsed nature [69], and kurtosis has high detectability for such RFI sources. In spite of the success of the kurtosis algorithm, there have been certain isolated cases where the detection algorithm has been unable to detect obvious high power RFI corrupted samples, as shown in Fig. 4.1. The plots indicate two separate field campaign results, SMAPVEX in the Fall of 2008 over New York, and CoSMOS in 2008 over central Europe. As shown, most of the RFI corrupted samples are detected, yet a few high-power samples remain undetected which can wash-out and cause low-level errors if consecutive integration periods are averaged together. One explanation is that these RFI sources have a 50% duty-cycle compared to the radiometric integration period. This is unlikely, since the statistics do not behave similar to a 50% duty-cycle signal when tested using variable integration periods [70].

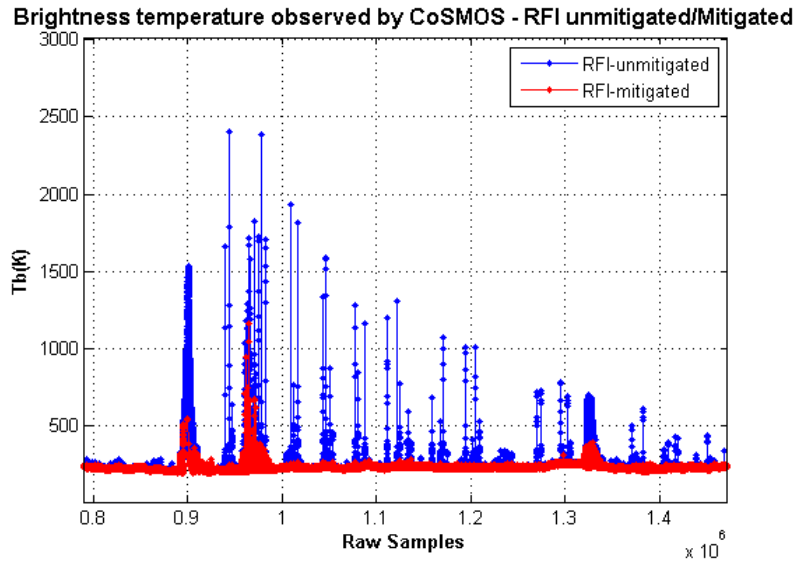
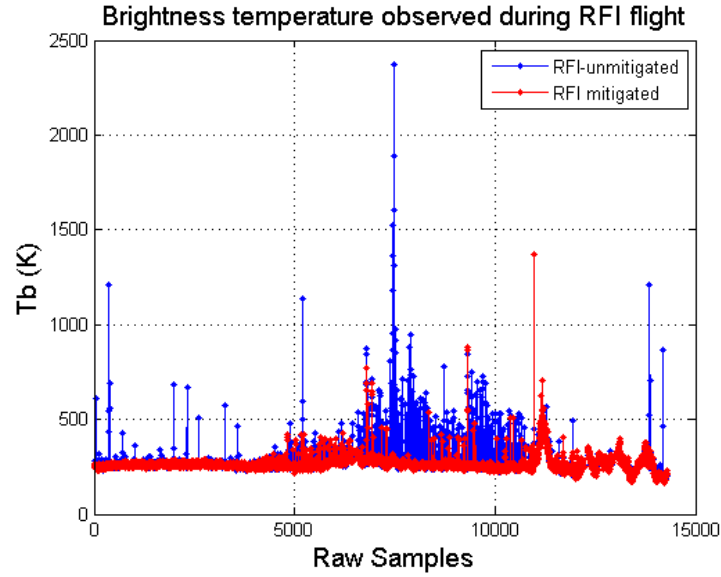


Fig. 4.1: Brightness temperature values over (a) New York – 10ms samples and (b) Central Europe – 8ms samples (*courtesy N.Skou*) indicating RFI (blue-unmitigated Tb, red-RFI mitigated Tb using full-band kurtosis)

### 4.3 Multiple Source RFI model

Previous literature [31, 46, 51, 54, 69] has modeled RFI as a single pulsed-sinusoidal source. Chapter 3 also assumes a pulsed source for comparing the detection algorithms.

This assumption was valid for L-band since most RFI expected is from air-defense and air-traffic control radars [44]. Although the 21 cm hydrogen line is officially protected, recent experience from field campaigns (Fig. 4.1) and results observed from SMOS indicate certain RFI signals exist in-band that might not be radar sites. Also, at other frequencies such as C-, X-, and K-band, low-powered multiple RFI sources might exist within the antenna footprint which need to be taken into consideration for evaluation of the kurtosis detection algorithm.

A more general RFI model is proposed which provides for the possibility of multiple pulse sinusoidal sources. It is given by

$$x(t) = n(t) + \sum_{i=1}^N A_i \cos(2\pi f_i t + \phi_i) \text{rect}\left(\frac{t-t_0}{w_i}\right) \quad (4.1)$$

where  $n(t) \sim N(0, \sigma^2)$  is normally distributed with zero mean and standard deviation  $\sigma$ ,  $A$  is the amplitude of the RFI source,  $f$  is the frequency,  $\phi$  is the phase shift,  $t_0$  represents the center of the on pulse of the duty-cycle,  $w$  is the width of the pulse and  $T$  is the integration period. The ratio ( $d=w/T$ ) represents the duty-cycle of the RFI source.  $f$  is assumed to be uniformly distributed between  $[0, 2\pi B]$  where  $B$  is the bandwidth of the radiometer.  $\phi$  and  $t_0$  are assumed to be uniformly distributed between  $[0, 2\pi]$  and  $[0, T]$  respectively.  $N$  is the total number of RFI sources.

Within an antenna footprint it is expected that the various RFI sources would be of different power levels. This is in addition to the fact that the side-lobes will see an RFI source differently than the main-lobe of an antenna does. As a result,  $A$  is modeled as a random variable. In order to obtain typical RFI amplitude distribution characteristic data

from the SMAPVEX RFI flight campaign was used (Appendix I). The distribution is exponential in nature with most of the RFI low-powered and very few high-powered outlying sources. Assuming the SMAPVEX data as representative of general RFI characteristics, the amplitude probability density function (pdf) is given by,

$$f(A) = \frac{1}{\nu} e^{-\frac{A}{\nu}} \quad (4.2)$$

where,  $f()$  represents the probability density function,  $A$  is the amplitude random variable of RFI, and  $\nu$  is the mean of the exponential pdf. For simulation purposes, the exponential mean is scaled to match total power contribution (sum of the distribution) between scenarios with different number of sources. Fig. 4.2 represents a typical amplitude pdf considered in this chapter.

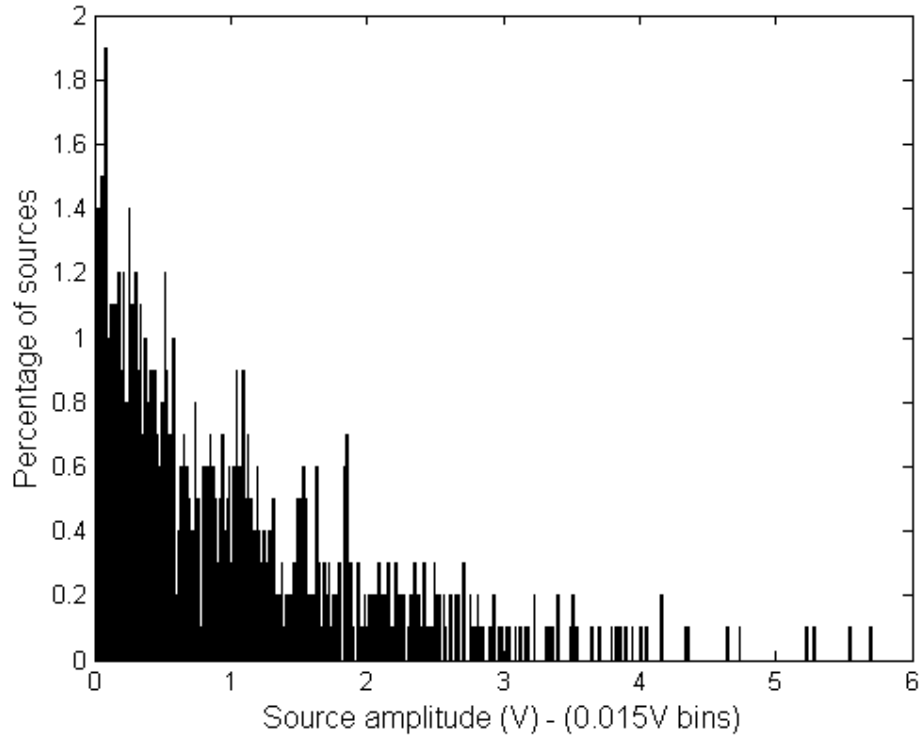


Fig. 4.2: Exponential pdf applied for amplitude of individual RFI sources, the mean of the exponential pdf is a scalable parameter based on required output power. The above plot has a mean of 1V.

Similarly, it is expected that most RFI sources within an antenna footprint would have different duty-cycles. Relative occurrence of RFI with a pulsed or CW duty-cycle can be characterized from a data set like the SMAPVEX campaign by noting whether the value of the kurtosis algorithm is above or below 3. Appendix I shows the CCDF of both types of RFI for various power levels. SMAPVEX results indicate that in general at L-band RFI is mostly pulsed-type in nature. Similar results are confirmed by analysis in [69] and [56], where most of the RFI pulses observed have a low duty-cycle. The above results though are typical of L-band signals and may not translate well to other microwave bands. Communication signals exhibit CW behavior, or have high duty-cycle. we consider a bimodal pdf with respect to duty-cycle, where the low-duty cycle region is approximated by a Rayleigh distribution and the high duty-cycle region is approximated by an exponential distribution as shown below,

$$f(d) = p \left( \frac{d}{b_d} e^{-\frac{d^2}{2b_d^2}} \right) + (1-p) \left( 1 - \frac{1}{\nu_d} e^{-\frac{1-d}{\nu_d}} \right) \quad (4.3)$$

where,  $f()$  is the probability density function,  $d$  is the duty-cycle (pulse width) random variable,  $p$  is the fraction of low duty-cycle sources,  $1-\nu_d$  is the mean of the exponential pdf and  $b_d$  is the mode of the distribution. For simulation purposes,  $\nu_d$  is kept around 0.1 and  $b_d$  is kept around 0.05. Both values are variable parameters that can be changed to assess the performance of detection algorithms. The Rayleigh distribution approximates a mostly low duty-cycle signal, whereas the reverse exponential pdf approximates signals around 100% duty-cycle trailing off towards 50%. The fraction  $p$  is a variable parameter that controls the amount of low to high duty-cycle sources within a single footprint. Fig.

4.3 indicates a duty-cycle distribution with equal amount of high and low duty-cycle sources.

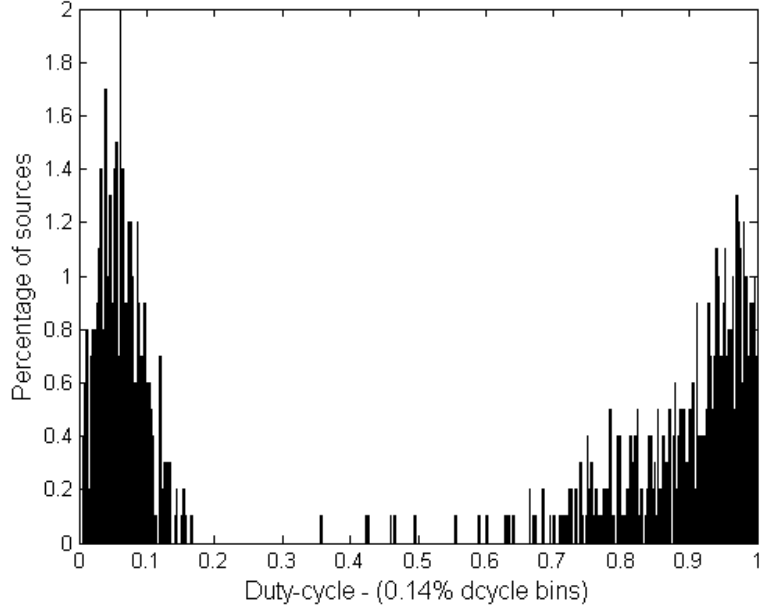


Fig. 4.3: Bimodal pdf applied for duty-cycle of individual RFI sources, the fraction of low duty-cycle to high duty-cycle is a variable parameter with the above plot indicating 50% of sources with low duty-cycle

#### 4.3.1 Probability distribution of Gaussian noise plus multiple pulsed-sinusoidal waveforms

In order to evaluate the performance of kurtosis detection in the presence of multiple RFI sources, it is necessary to obtain the probability density function of the thermal noise with RFI corrupting it. The previous RFI model [31, 54] used a pdf of a thermal noise source with additive pulse-sinusoidal RFI interference obtained from [71]. Due to multiple sources, the characteristic function of a pulsed-sinusoid source is calculated to obtain the pdf. The characteristic function of the sum of multiple independent sources is the product of their individual characteristic functions. The probability density function of RFI is the inverse Fourier transform of the calculated characteristic function.

In order to calculate the pdf, the characteristic functions of the individual components are obtained and then multiplied together. The characteristic function of a normal distribution is well known and is shown below.

$$\varphi_n(u) = e^{-\frac{\sigma^2 u^2}{2}} \quad (4.4)$$

where  $\sigma$  is the standard deviation of a normally distributed function. The characteristic function of a pulsed sinusoid can be found as follows

$$\begin{aligned} \varphi_{psi}(u) &= \frac{1}{2\pi} \frac{1}{T} \int_0^{2\pi} \int_0^T e^{juA_i \cos(2\pi f_i t + \phi_i) \text{rect}\left(\frac{t-t_0}{w_i}\right)} dt d\phi \\ &= \frac{1}{2\pi} \frac{1}{T} \int_0^{2\pi} \int_t^{t+T} e^{juA_i \cos(2\pi f_i t + \phi_i) \text{rect}\left(\frac{m}{w_i}\right)} dm d\phi \\ &= \frac{1}{2\pi} \int_0^{2\pi} \frac{1}{T} \left\{ e^{juA_i \cos(2\pi f_i t + \phi_i)} w_i + T - w_i \right\} d\phi \\ &= \frac{1}{2\pi} \int_0^{2\pi} \left\{ e^{juA_i \cos(2\pi f_i t + \phi_i)} d_i + (1 - d_i) \right\} d\phi \\ &= d_i J_0(A_i u) + (1 - d_i) \end{aligned} \quad (4.5)$$

where  $J_0$  is a Bessel function of the zeroth order,  $A_i$  is the amplitude of the  $i^{th}$  RFI source,  $f_i$  is the frequency,  $\phi_i$  is the phase shift,  $t_0$  represents the center of the on pulse of the duty-cycle,  $w_i$  is the width of the on pulse and  $T$  is the integration period. The ratio ( $d_i = w_i/T$ ) represents the duty-cycle of the  $i^{th}$  RFI source.

The total characteristic function is obtained by taking the product of eqn. (4.4) and eqn. (4.5) and is given by

$$\varphi_T(u) = \varphi_n(u) \prod_{i=1}^N \varphi_{psi}(u) \quad (4.6)$$

where  $N$  is the total number of RFI sources. The probability distribution function  $f(t)$  is the inverse Fourier transform of the characteristic function above. The probability density of eqn. (4.1) is given by

$$\begin{aligned} f(t) &= F^{-1}[\varphi_T(u)] \\ &= F^{-1} \left[ e^{-\frac{\sigma^2 u^2}{2}} \prod_{i=1}^N (d_i J_0(A_i u) + (1-d_i)) \right] \end{aligned} \quad (4.7)$$

where  $J_0$  is a zeroth order Bessel function and  $F^{-1}[\dots]$  represents the inverse Fourier transform operator.

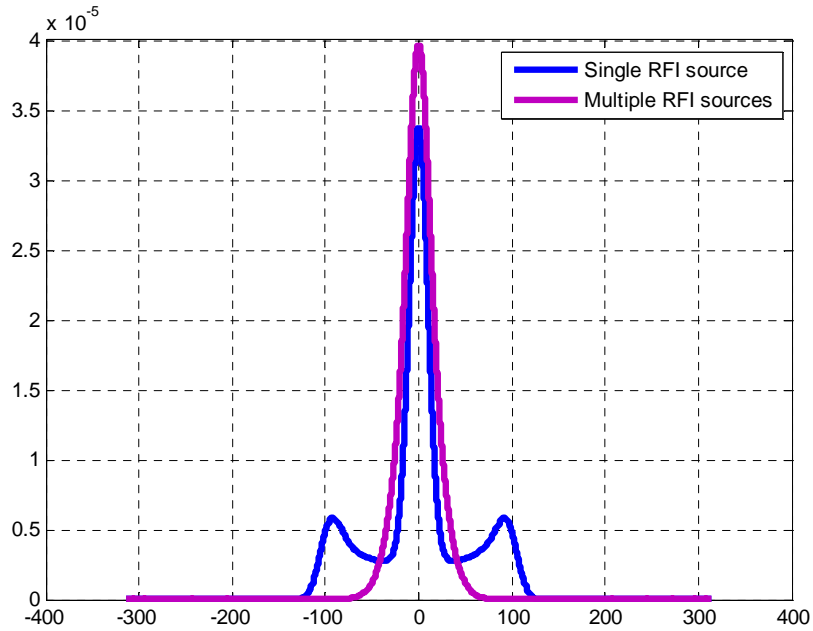


Fig. 4.4: Probability density function of RFI with thermal noise, blue curve represents a single RFI source and purple curve represents multiple sources (50% sources, 100% low duty-cycle)

Fig. 4.4 shows the pdf of a Gaussian signal corrupted by a single RFI source and multi-source RFI. Note that these distributions will in general depend on various RFI parameters such as mean power and duty-cycle fraction. As can be seen in Fig. 4.4 the distribution of a multi-source corrupted thermal signal appears to have a bell shaped curve, similar to the uncorrupted original signal.

#### **4.4 Kurtosis Performance**

The performance of the kurtosis detection algorithm can be assessed when multiple RFI sources are present within the antenna footprint. In order to account for the random distribution of duty-cycle and amplitude of the RFI sources, Monte-Carlo simulations were performed and the average kurtosis ratio and power were determined in each case. The total power contributed by all RFI sources is kept constant as the number of sources increases. An example is considered in which the total power level of RFI is nearly 100 times the NE $\Delta$ T. Fig. 4.5 shows the value of the kurtosis ratio with respect to number of sources and fraction of low duty-cycle sources within the antenna footprint. The orange region of the contour plot represents a kurtosis of approximately 3, which is the blind-spot region for the detection algorithm. As can be seen in Fig. 4.5, with a high number of sources, the kurtosis becomes Gaussian-like. RFI sources with low-duty cycle sources converge towards 3 at a much slower rate than RFI sources with even a small fraction of CW sources. Kurtosis still maintains superior detectability for low duty-cycle sources, but the performance degrades rapidly due to the inclusion of communication type CW signals. This indicates that the number of high duty-cycle sources dominates the performance of the kurtosis detection algorithm.

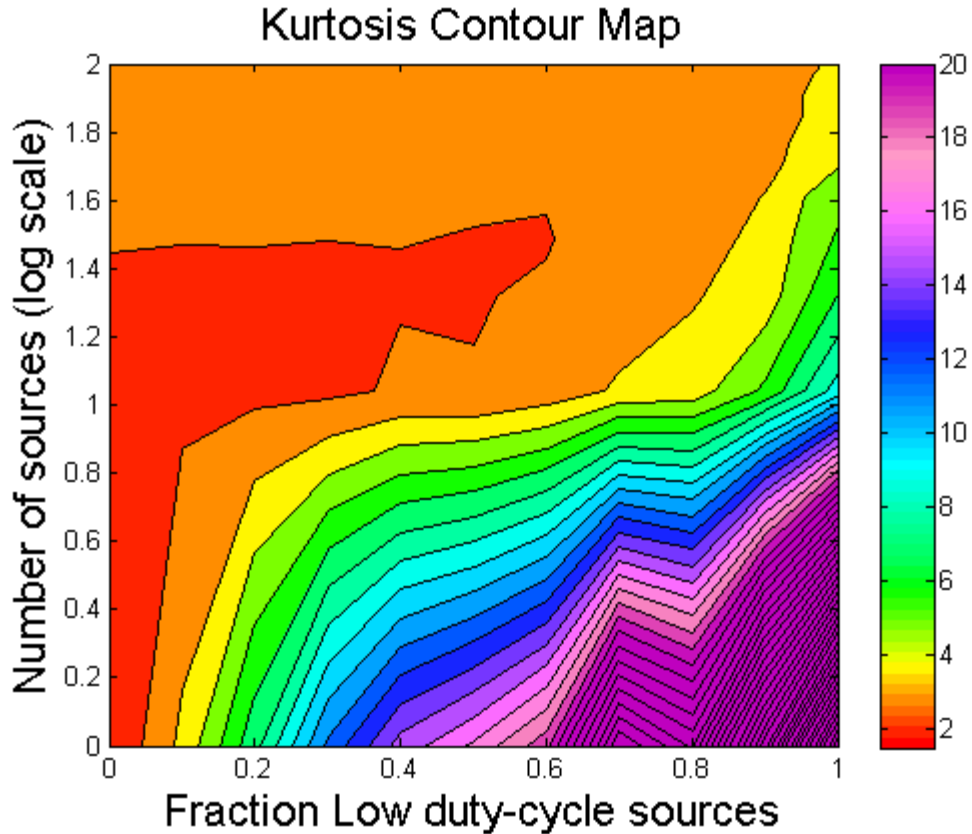


Fig. 4.5: Mean value of kurtosis as a function of number of sources and fraction of low duty-cycle sources. The overall power remains the same as the number of sources increases. (Orange  $\rightarrow$  Kurtosis = 3)

Characterization of RFI in L-band shows that most RFI is of the low duty-cycle type (Appendix I) and hence several low duty-cycle sources in the L-band would need to be present for kurtosis to be affected by central-limit conditions. Also, more RFI sources result in higher interference power. Platforms such as SMAP plan to operate a hybrid of the kurtosis detector and pulse-detector algorithms that can easily identify large brightness temperature jumps. Thus, the issue of central-limit should not be a problem for SMAP because even if the kurtosis misses detecting such RFI, a large number of sources resulting in high-power RFI should be caught by the pulse-detect algorithm.

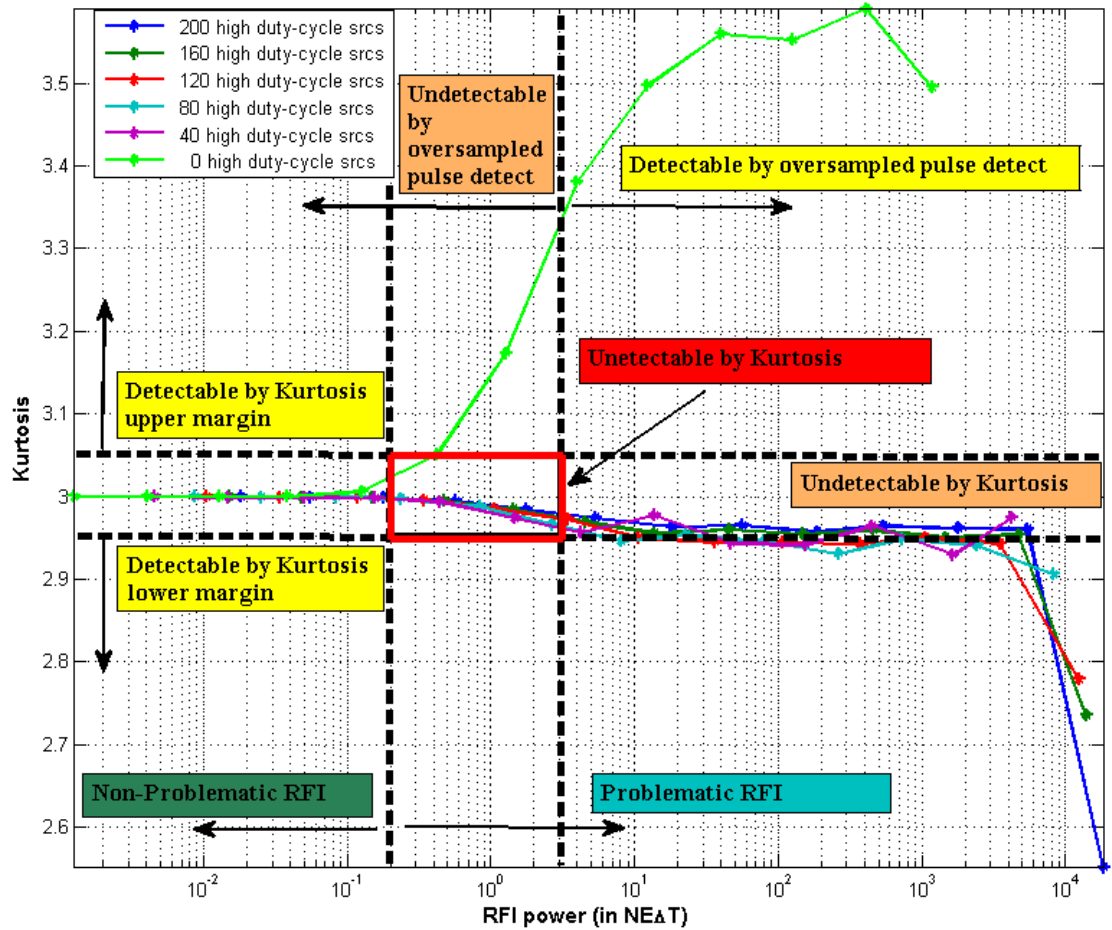


Fig. 4.6: Mean value of kurtosis vs. RFI power (in  $NE\Delta T$ ) for 200 sources (Region between black dashed lines – Undetectable RFI by kurtosis or oversampled pulse detect, Red rectangle – Undetectable problematic RFI)

Detectability for SMAP will be an issue when the power is low enough for pulse-detect to miss RFI but the number of sources is high enough for central-limit conditions to be applied to the kurtosis. With the advent of low-power RFID and Wi-Fi systems operating on individual electronic devices in a few years, RFI corruption from such devices might not be in the form of an obvious spike (or jump), and might be low enough to be near the NEAT of the radiometer. The kurtosis detector is capable of detecting spread-spectrum low-power systems [46] but with multiple sources and low power, detection becomes an

issue. This is illustrated in Fig. 4.6. The figure shows the effect on kurtosis observing 200 sources, as the relative power decreases. The rectangular box indicates a region where RFI power is between 0.2 and three times the  $NE\Delta T$  and kurtosis is within three times the  $NE\Delta K$ , the detection threshold of kurtosis, assuming  $\sim 100K$  independent samples in an integration period. RFI within this box will be undetectable, yet have a high enough power (above 0.2  $NE\Delta T$ ) to be potentially problematic and impact science measurements [47].

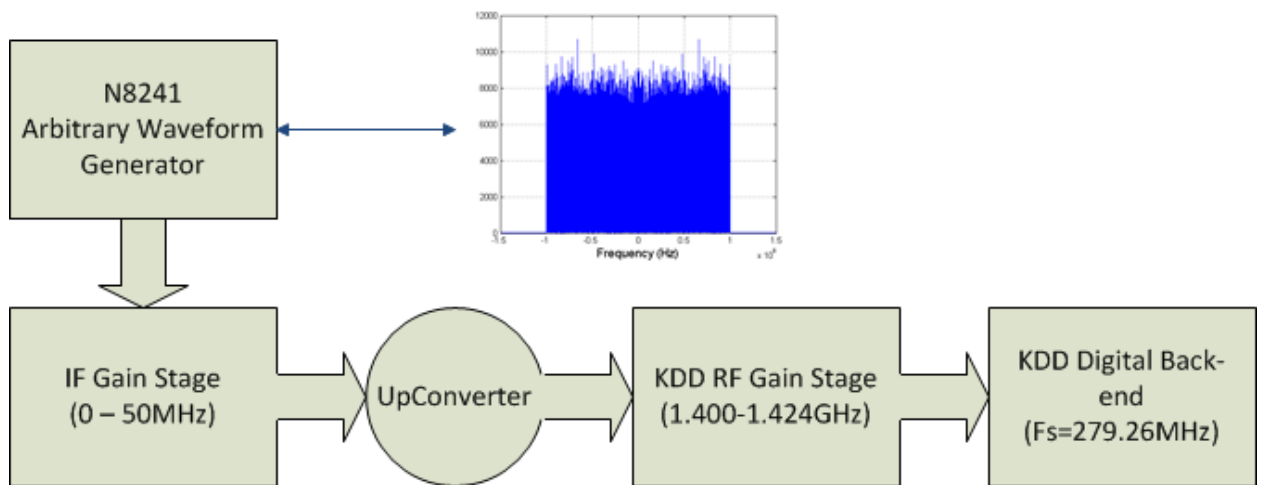


Fig. 4.7: Block-diagram of Multi-source RFI experimental setup

#### 4.5 Experimental verification

In order to demonstrate the performance of the kurtosis detector in the presence of multiple RFI sources, a bench-top radiometer experiment was performed. Fig. 4.7 shows a block diagram of the setup. The experimental setup uses a National Instruments Arbitrary Waveform Generator (AWG) N8241 to simulate background microwave thermal emission with RFI corruption. The AWG operates at a sampling rate of 1.25Gs/s. In order to generate phase matched and filtered thermal noise, an inverse

Fourier transform of a filtered random signal was taken. RFI was added with a variable number of sources but keeping the thermal signal power-level the same, and using uniform frequency, phase, and pulse start-time distributions. Duty-cycle and amplitude were also varied, according to the distributions discussed in the previous sections.

Analog signal output from the AWG (with a baseband bandwidth of 500MHz) was then up-converted to a 1.413GHz center frequency and filtered between 1.4 and 1.424GHz. The signal was then introduced into the University of Michigan Kurtosis Digital Detector (KDD) RF stage and digital back-end [30]. In summary, KDD sub-samples the RF input signal at a rate of 279.26MHz after which digital signal processing is performed including detection of the signal's kurtosis. For purposes of this experiment, band limited Gaussian noise covered the spectral passband and simulated RFI was uniformly distributed across the passband.

Fig. 4.8 shows results from the lab experiment, in which a background thermal source is corrupted with additive RFI. The overall relative power of the RFI was kept the same for varying number of sources. The plot indicates excess kurtosis vs. excess RFI in scaled brightness temperature units, based on a 300K clean thermal background. All the RFI sources have a high duty-cycle, which is why the excess kurtosis is below zero. The dashed lines represent the noise margin of kurtosis (i.e.  $4 \cdot \text{NE}\Delta\text{K}$ ) for the given system. Any sample between the dashed lines is undetectable. The different colors in Fig. 4.8 represent different data points with the same number of RFI sources. For example, red represents data points with a single RFI source and black represents 11 RFI sources; the other colors represent intermediate numbers of RFI sources. The experimental results confirm that as the number of sources increases the detectability of the kurtosis decreases.

This is apparent by looking at the slope of the single source CW RFI red data samples, which is more negative, whereas for multiple CW source RFI samples (e.g. black) the slope tends more towards the horizontal.

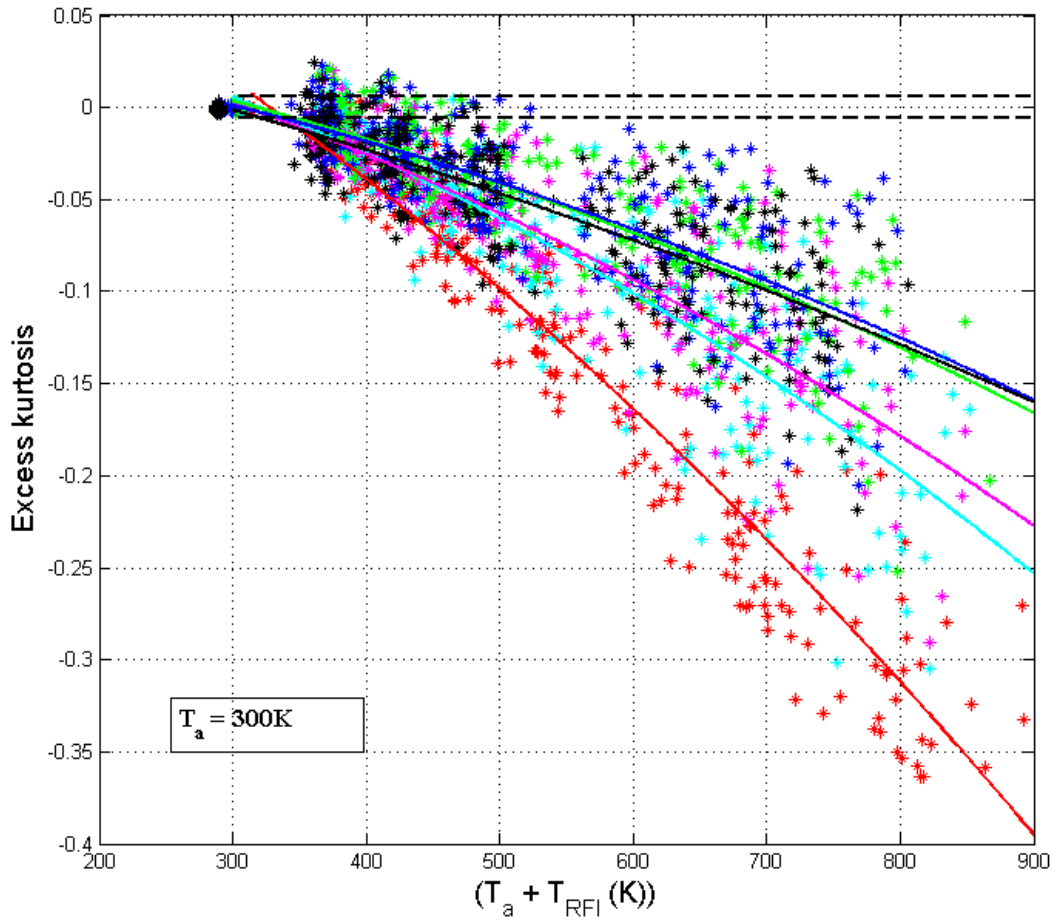


Fig. 4.8: Experimental results indicating excess kurtosis versus excess RFI Tbs in Kelvin (scaled assuming RFI-free thermal emission of 300K). The dashed lines represent the  $\pm 4 \cdot NE\Delta K$  of kurtosis. The colors represent any RFI corruption due to different numbers of sources. (Legend: Red=1src, Cyan=3srcs, Purple=5srcs, Green=7srcs, Blue=9srcs, Black=11srcs)

These results can be used to interpret and explain the presence of the large ( $\sim 1350 \text{ K}$ ) RFI spike noted in Fig. 4.1 that was not identified by the kurtosis detector. If the antenna footprint for this data sample is assumed to contain multiple CW RFI sources, the

minimum number of sources required to cause an RFI spike of 1350K that is blind to the kurtosis can be calculated. Performing a quadratic fit to the data in Fig. 4.8 it is possible to parameterize the behavior of kurtosis with respect to the number of sources for different power levels. The curves in Fig. 4.9 indicate how the kurtosis approaches 3 (excess kurtosis = 0) as the number of sources increases. Calculating a fitted curve for  $T_{REC}$  of 1350K, it is found that at least 27 separate CW RFI sources are needed to cause such a spike to be missed by the kurtosis detector. The geographic location of the antenna footprint for the 1350K TB spike in Fig. 4.1 was latitude = 40.74 degrees North, longitude = 74.04 degrees West, which is approximately near Manhattan, New York city. Urban areas can be expected to contain a higher density of CW RFI emitters.

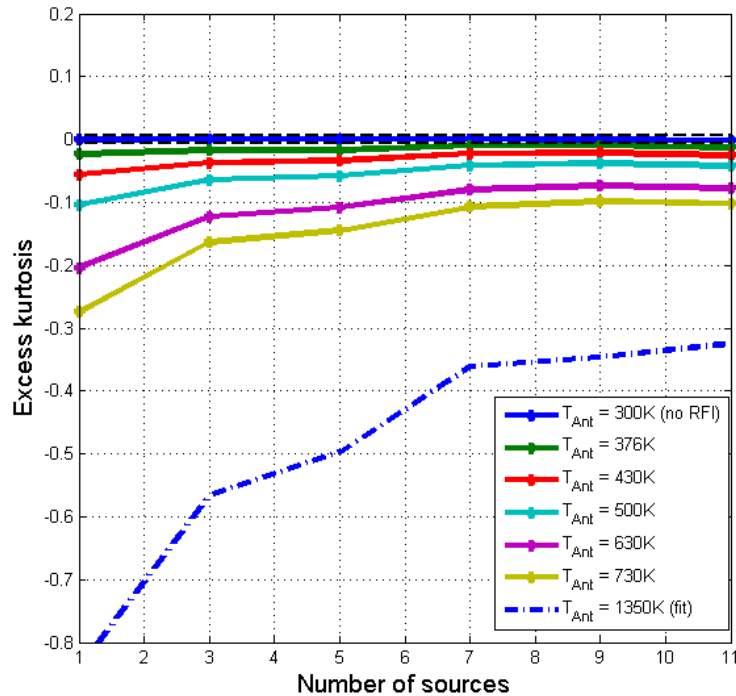


Fig. 4.9: Curves indicating kurtosis variation versus the number of RFI sources for different power levels. The solid lines represent mean kurtosis calculated from experimental data, the dashed curve is fit from the experimental data at 1350K antenna Tb with a 300K background.

## 4.6 Conclusion

The performance of the kurtosis detection algorithm was evaluated for conditions under which multiple RFI sources are present. A new RFI model was developed to replace the single pulsed-sinusoidal RFI model currently used for analysis of RFI detection algorithms. The new RFI model assumes an exponential distribution of RFI power and a bimodal distribution of the duty-cycles of individual RFI sources. Results indicate that the kurtosis algorithm is influenced by the central-limit theorem when enough sources are present. This will cause the kurtosis detection algorithm to miss certain high-powered RFI. The kurtosis algorithm is less sensitive if some of the RFI sources are high duty-cycle CW sources. The model results are verified using experimental lab data.

SMAP uses pulse-detect algorithm along with the kurtosis detection algorithm, and can easily detect high powered pulses missed by the kurtosis. Multiple low-powered Wi-Fi urban RFI sources around the noise-margin of a radiometer can be most detrimental since they may be undetectable by either algorithm.

## **Chapter 5**

### **Analysis of Radio Frequency Interference Detection Algorithms in the Angular Domain for SMOS**

#### **5.1 Introduction**

The European Space Agency's (ESA) Soil Moisture Ocean Salinity (SMOS) mission [63, 72] has been steadily providing global maps of brightness temperature (Tb) since soon after its launch in November, 2009. SMOS is responsible for retrieving measurements of sea-surface salinity (SSS) and soil moisture at 1.4 GHz (the 21-cm hydrogen line) (or L-band). Even though Tb measurements are made in a protected part of the spectrum, various airborne campaigns [40-41, 59] have observed Radio Frequency Interference (RFI) signals corrupting Tb measurements at L-band. Initial SMOS measurements have also observed large amounts of RFI.

Due to the unique nature of SMOS hardware, these conventional RFI detection techniques such as temporal subsampling or spectral subbanding can't be used for SMOS. SMOS measures Tb over a single 24MHz passband centered at 1.413GHz and so it can not apply spectral subbanding RFI detection techniques. The temporal resolution of SMOS is not fine enough to apply a similar pulse-detection algorithm as is used by over-sampled sensors [49-50, 64].

Microwave Imaging Radiometer using Aperture Synthesis (MIRAS) is an interferometric radiometer used by SMOS for measuring Tb. Some RFI detection techniques specific to SMOS hardware have been developed, e.g. by [38], where unnatural 3<sup>rd</sup> and 4<sup>th</sup> Stokes outliers are flagged as RFI sources. Another algorithm developed for SMOS detects point source RFI by

applying a similar technique developed for SMOS to cancel Sun effects [73]. This chapter presents an RFI detection algorithm that takes advantage of unique signal processing properties of MIRAS. RFI mitigation and detection techniques can be applied at many different stages of the processing. This chapter examines and compares the detectability of different RFI algorithms at the L1a stage (Visibility domain), the spatial domain (Tb snapshot images) and the angular domain (Tb versus incidence angle).

In Section 2, we give details of the various SMOS signal domains in which the RFI detection algorithm can be applied, and present a new angular domain detection algorithm. A discussion of the differences in algorithm performance between domains is presented in Section 3. Section 4 presents representative results of the angular domain detection algorithm, before summarizing in Section 5.

## **5.2 SMOS RFI Detection Domains**

The SMOS mission makes interferometric passive microwave measurements of the incoming thermal emission. The measurements are related to the Fourier Transform of the spatial brightness temperature distribution, and are referred to as visibility measurements. A two-dimensional “snapshot” Tb image is derived from the visibility domain by taking an inverse Fourier Transform of the visibility measurements. SMOS has an effective image field of view of 1050 X 650 km<sup>2</sup> and a snapshot is taken every 1.2s [74]. This means SMOS observes a single grid-point on the earth with multiple snapshots at different incidence angles.

An RFI detection algorithm can in principle be applied at any phase of data processing. The three domains considered here: visibility, spatial and angular. Each is described below in greater detail.

### **5.2.1 Visibilities Domain**

The visibilities domain is contained in the L1a data set produced by the SMOS program. This data set contains spatial frequency information about the Tb image. For example, the zeroth visibility measurement can be considered to be the d.c. component (or mean) of the image over the field of view, weighted by the antenna element pattern.

An RFI detection algorithm based in the visibility domain of SMOS has been developed which would operate on successive time-domain samples of the zeroth visibility data [75]. The zeroth visibility data is similar to a conventional (non-interferometric) radiometer, measuring the power of the incoming emissions. The algorithm is essentially a temporal RFI detection algorithm, wherein samples are compared to their neighboring (in time) pixels. Any outliers or spikes that deviate from the expected smooth variation by more than a preselected threshold are flagged as being corrupted by RFI. Other visibilities might also be tested for the presence RFI, the following chapter only considers the zeroth visibility since the natural variability of the visibility with changing scenes will be higher compared to the mean (zeroth) visibility.

Such an algorithm has the advantage of detecting RFI very early in the signal processing flow. Visibility measurements for SMOS have a relatively low NE $\Delta$ T noise level of approximately 0.2K [76], which aids in RFI detection performance by reducing the false alarm rate. Large RFI sources inside and outside the alias-free Field of View (FOV) [77] can be immediately identified by the above algorithm. Another advantage of RFI detection in this domain is the fact that the algorithm can utilize the positive definite L2 norm property of the zeroth visibility RFI

perturbations [75]. That is, RFI is always positively biased. One limitation of RFI detection in the Visibility domain is the fact that highly spatially localized sources (isolated hot spots) will have a much lower signal amplitude in the visibility domain than in the spatial domain, because the d.c. visibility samples are an average over the entire image, including regions without any RFI.

### **5.2.2 Spatial Domain**

The next step in SMOS processing is to convert visibility measurements to Tb snapshots. This domain represents Tb values at individual grid point locations within the snapshot image field of view. A snapshot is taken every 1.2s. Since the Tb images are obtained after taking an inverse Fourier transform of the visibility measurement, the image contains aliased as well as alias-free Tb zones. The RFI detection algorithm operates in the alias free field of view only.

Different versions of a spatial RFI detection algorithm have been applied in the past for microwave radiometer measurements [34, 73]. The basic principle of such algorithms is to compare the deviation of a pixel under test with its neighboring pixels in the spatial domain. The algorithm generally involves some sort of moving spatial averaging window. If the pixel under test deviates considerably from the mean with respect to some threshold, then the pixel is flagged as being corrupted. The spatial domain algorithm is effective at flagging isolated Tb spikes.

Compared to the visibility domain, the noise level is higher (with an NE $\Delta$ T of approximately 5K) in the spatial domain due to error propagation through the inverse Fourier transform,. This represents an increase in noise, relative to the visibility domain, by a factor of  $\sim 25$ . The RFI power level will also increase as a result of the inverse Fourier transform. In this case, however, the increase will be by a factor of  $\sim 25^2$  if the RFI source is spatially localized because the inverse Fourier transform will coherently focus the visibility measurements at the spot in the image

where the RFI is located. This results in a higher signal-to-noise ratio, giving better detection performance. The main disadvantage of spatial detection algorithms is that natural geophysical variations within the spatial averaging window can cause RFI false alarms or missed-detections. Also due to the interferometric nature of the imaging, any strong RFI point sources suffer from Gibbs phenomenon. That is, in the Tb snapshot image a powerful RFI point source is surrounded by oscillating negative and positive annular rings. This results in RFI that can be negatively biased with respect to the mean neighbors. For this reason, spatial detection algorithms must be designed to detect both positively and negatively biased RFI pixels.

### **5.2.3 Angular Domain**

SMOS has the unique advantage of observing a single grid point on the earth over multiple incidence angles. As a result, an RFI detection algorithm can be applied in a domain that is one step further in the processing chain compared to the spatial domain. Detection of anomalous behavior in the Tb variation with respect to incidence angle is another method to aid in flagging RFI corrupted measurements [57]. The angular domain algorithm is a primary focus of this chapter.

Depending on the polarization being observed, Tb values tend to have a very specific dependence on incidence angle. This dependence is influenced by variables such as vegetation canopy, physical surface temperature, surface roughness, moisture content in the soil, salinity of water etc. Knowledge of this relationship aids in the inversion of such geophysical variables as soil-moisture and sea-surface salinity. The principle behind this new type of RFI detection algorithm is that if RFI is present in some but not all of the snapshots, a single geographic location that is contained in multiple images will exhibit outlier behavior due to RFI when Tb is viewed as a function of incidence angle.

RFI outliers detected in the angular domain have the same signal to noise ratio that exists in the spatial domain. Detection in the angular domain takes advantage of the fact that there exists a much more deterministic relationship between the sample under test and its neighboring samples at other incidence angles, relative to the relationship between a spatial sample and its neighboring pixels. This allows for better prediction of an estimated value for the sample under test, based on the Tb values of its neighboring incidence angles at the same location, which results in a more accurate detection threshold. Since the measurements are made at one grid point location, the detection statistics are not influenced by the spatial variability of neighboring pixels. One caveat with this method is that, over high incidence angles, the effective pixel footprint stretches and may be contaminated by neighboring spatial locations. In order to avoid such contamination, the angular domain algorithm operates only within a restricted range of incidence angles.

The angular domain algorithm is described in detail below.

#### **5.2.3.1 Algorithm description**

The algorithm is used whenever there are a sufficient number of samples versus incidence angle at a grid point. The default number of samples required for the algorithm to operate is 10. As a result, most samples at the edge or “wing” of the SMOS hexagonal alias-free snapshot cannot have this RFI algorithm applied to it, whereas there are more samples near the center of the image. Fig. 5.1 indicates the number of multiple incidence angle measurements made at each grid location in the image over a half orbit. As expected, most of the counts are in the center of the swath, with lesser measurement points made at the edges.

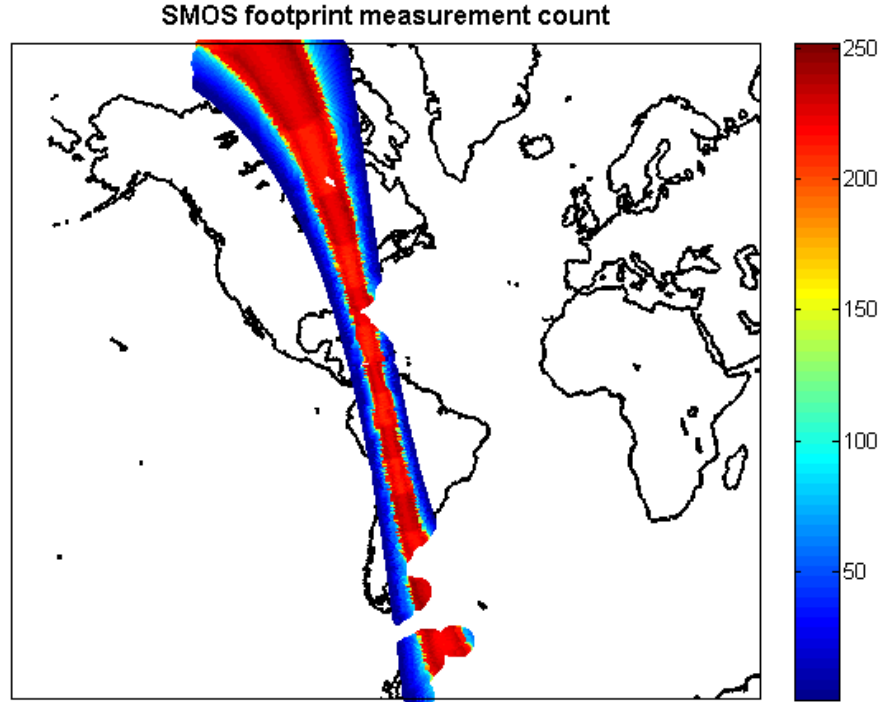


Fig. 5.1: SMOS semi-orbit map indicating the number of multiple measurements made at a single grid-location over various incidence angles

The algorithm first collects all samples versus incidence angle at a grid point and flags any sample above 330K or below 0K as containing RFI. These samples are discarded from subsequent processing. The remaining samples (which must number six or greater in order to continue) are then used to fit a third order polynomial to the dependence of Tb on incidence angle at that grid point.

In order to determine an RFI detection threshold, a cubic Tb relationship is estimated from the Tb measurements as given by

$$\hat{T}_i = c_0 + c_1\theta_i + c_2\theta_i^2 + c_3\theta_i^3 \quad (5.1)$$

where,  $\hat{T}_i$  is the brightness temperature estimate at the  $i^{th}$  incidence angle,  $\theta_i$  and  $c_n$  ( $n=0,1,2,3$ ) are the regression coefficients estimated from the measured Tb vector as shown below,

$$C = \begin{bmatrix} c_0 \\ c_1 \\ c_2 \\ c_3 \end{bmatrix} = (\Theta' \Theta)^{-1} \Theta' \begin{bmatrix} T_1 \\ \cdot \\ \cdot \\ \cdot \\ T_m \end{bmatrix} \quad (5.2)$$

where,

$$\Theta = \begin{bmatrix} 1 & \theta_1 & \theta_1^2 & \theta_1^3 \\ \cdot & \cdot & \cdot & \cdot \\ \cdot & \cdot & \cdot & \cdot \\ 1 & \theta_m & \theta_m^2 & \theta_m^3 \end{bmatrix}$$

and  $T_i$  is the measured Tb value at incidence angle  $\theta_i$ .

The cubic-fit is performed with all valid Tb measurement samples other than the sample under test. This way the fit is not impacted by any RFI corruption of the sample under test. Once the Tb estimate of the sample under test is obtained, detection is performed by comparing the absolute value of the difference between the estimated and original Tb with some threshold, or

$$f_i = \begin{cases} 0 & \text{if } |\hat{T}_i - T_i| < 3S \\ 1 & \text{if } |\hat{T}_i - T_i| \geq 3S \end{cases} \quad (5.3)$$

where  $f$  is the RFI flag (0 means no RFI, 1 means RFI), and  $3S$  is the detection threshold.  $S$  is defined as the smaller of the measurement NEAT and the RMS residual error in the cubic fit. If there is no RFI present in the Tb samples used to determine the cubic fit, its residual error tends

to be smaller than the NEAT and the residual error is a more conservative detection threshold. If there are RFI corrupted samples used in the cubic fit then its residual error is greater and the NEAT is a better threshold.

In addition to the above threshold test, if a majority of the samples at a grid point are above 330K, and the number of samples necessary for a fit is insufficient, then all remaining samples are flagged as being corrupted by RFI. There is also a residual error metric with each flag that gives an indication of the confidence in the cubic fit and hence the trust in the detectability for that particular sample under test.

### **5.3 Domain Comparison**

SMOS can apply RFI detection algorithms at various stages of the processing tree. The three main domains considered here are Visibility (L1a), Spatial and Angular (L1c). There are advantages and disadvantages to applying RFI algorithms at these different stages. The following section discusses these.

#### **5.3.1 Visibility Domain versus Spatial Domain**

Detection using the zeroth visibility will be compared to detection with a single Tb snapshot in the spatial domain. Comparisons will be based on two factors, signal strength of RFI in the two domains, as well as noise-increase going from one domain to another.

The zeroth visibility or the reference radiometer of MIRAS uses an antenna element with a real aperture. MIRAS as a whole synthesizes an effective aperture area that is larger than that of each individual element. Based on the Friis transmission formula [78], the power of an incoming RFI point source ( $P_r$ ) is linearly proportional to the effective aperture of the receiver ( $A_r$ ). MIRAS

has a larger aperture ( $\sim 7\text{m}$  diameter) than the reference radiometer ( $< 9\text{cm}$  radius), and hence the signal strength of the RFI seen by the interferometer is stronger.

Another means of quantifying RFI signal strength is with respect to spatial resolutions. SMOS pixels have a spatial resolution of approximately  $50 \times 50 \text{ km}^2$  (depending somewhat on incidence angle), whereas the zeroth visibility reference antenna observes an area of approximately  $\pi(1500^2) \text{ km}^2$ . The observed strength of the RFI source will be higher in the spatial domain, relative to the visibility domain, by a factor of  $\sim 2800$  ( $= \pi * (1500)^2 / 50^2$ ). This factor can also be viewed as the ratio between the actual gain of the reference radiometer's antenna and the gain of the effective antenna that is formed by Fourier synthesis.

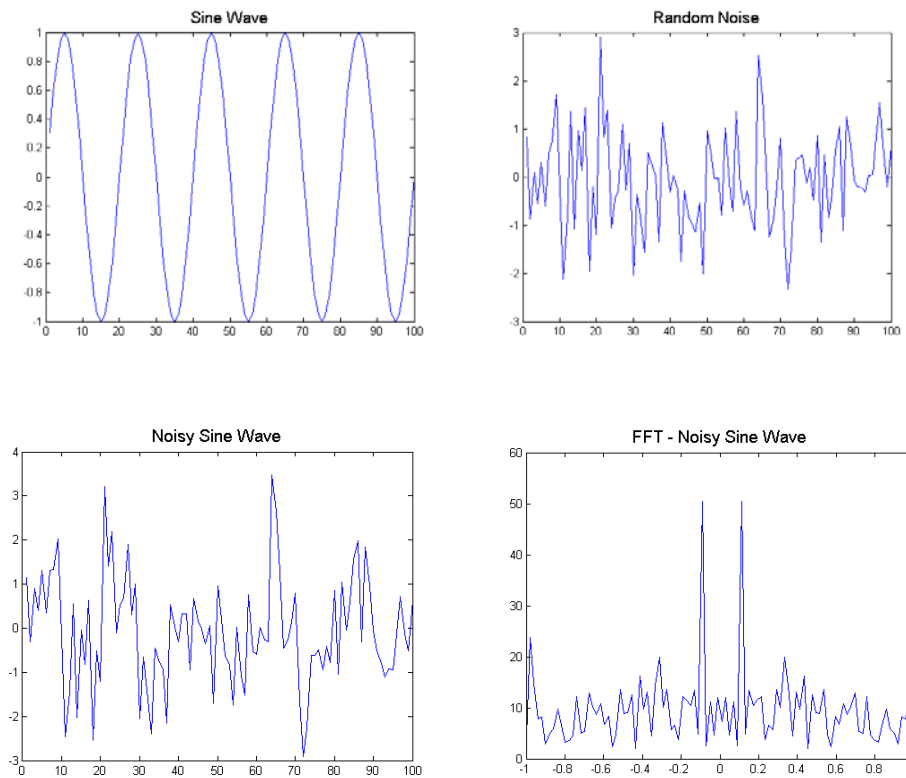


Fig. 5.2: Illustration of (a) Sinusoidal wave in time domain (b) Gaussian noise in time domain (c) combined signals in time domain, representing an indistinguishable noisy sinusoidal wave, and (d) combined signals in frequency domain, with clear peaks distinguishable from the noise floor.

RFI detectability in these two domains can also be understood in terms of the concept of sparsity. A sparse representation effectively means an efficient representation of a vector. For example, a single tone sinusoidal wave has a sparse representation in the frequency domain. In the frequency domain only one principle component (its frequency) is needed to describe the signal, while the rest of the values are zero. In the time domain, all the time domain samples are required to fully describe the sinusoidal wave and hence it is not an efficient representation. A sparse representation is an efficient signal model [79], with only a few principle components required to describe the signal. As an illustration, Fig. 5.2 represents a sinusoidal wave added to Gaussian noise. While it is difficult to distinguish the noisy sinusoidal wave in the time-domain, it is much easier to detect it in the frequency domain by the two clear peaks above the background noise floor.

The same principle applies with the SMOS visibility and spatial domains. Single point source RFI has a more sparse representation in the spatial domain relative to the visibility domain. A single principle component is required to describe a point source in the spatial domain, whereas in the visibility domain all  $N$  visibility elements (or unique antenna pairs) are required to describe the same point source. The RFI signal power increases by a factor of  $N$  when going from the visibility domain to the spatial domain. For SMOS, this value is approximately 2346 [80]. Similar to the previous results, RFI signal strength is  $\sim 2346$  times stronger in the spatial domain.

Noise also increases when going from the visibility domain to the spatial domain. The visibility domain has an RMS noise level of approximately  $0.2K$ . Noise increases by a factor of  $N^{1/2}$  in the spatial domain due to error magnification by the image reconstruction algorithm. In terms of SMOS, this results in an NE $\Delta T$  of approximately  $5K (=0.2K*(2346)^{1/2}/2)$ . The factor of 2 in the

denominator is due to the required double sided RFI threshold in the Tb domain without the positive definite L2 norm constraint on RFI perturbations that was possible in the visibility domain. Based on an increase by a factor of N in RFI signal strength and a factor of  $N^{1/2}$  in noise-level, the overall signal to noise ratio (SNR) of RFI increases by a factor of  $N^{1/2}$  when going from the visibility to the spatial domain.

Applying a  $3\sigma$  (SNR=3) detection threshold, we note that the minimum detectable RFI strength in the visibility domain occurs if the zeroth visibility ( $V_0$ ) is above 0.6K. This corresponds to a point source Tb of 1380K. The spatial domain can detect an RFI signal above 15K in strength, which corresponds to  $V_0$  of 0.005K.

Fig. 5.3 provides two RFI scenarios in which the algorithm performance of the two domains will differ. Fig. 5.3a shows a clear RFI spot of an approximate signal strength of 1500K (after removing thermal background). This RFI point source is equivalent to  $V_0$  of 0.65K in the visibility domain, which is just above the detection threshold and would be detectable by both algorithms. Fig. 5.3b shows a clear RFI spot of around 150K. This RFI spot is easily detectable in the spatial domain, but amounts to only 0.065K in the zeroth visibility, placing it well below the noise floor and undetectable.

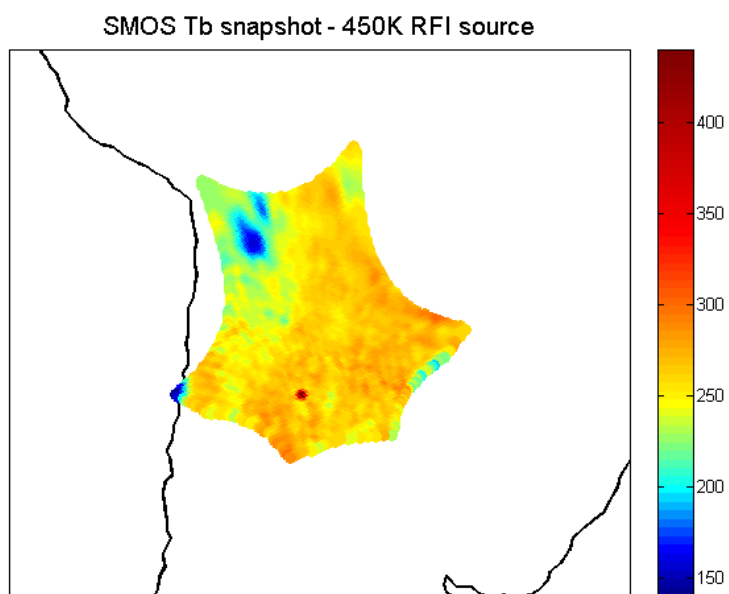
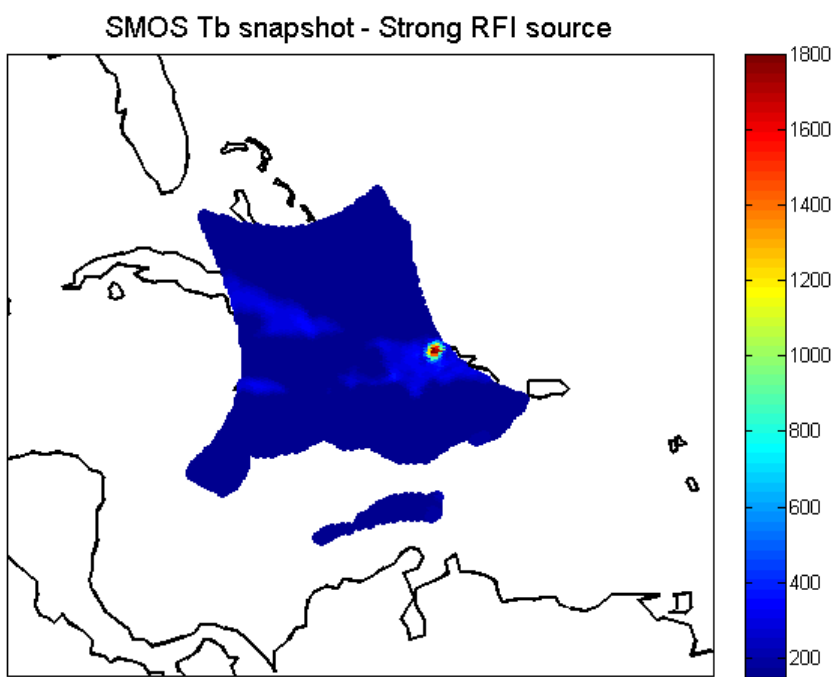


Fig. 5.3: Two SMOS snapshots contaminated by single point source RFIs (a) RFI Tb = 1500K (b) RFI Tb = 150K

The visibility domain does have a unique advantage, as the number of RFI point sources increase, the relative performance of the visibility domain algorithm improves relative to the spatial domain, since all the sources will add together in the zeroth visibility measurements.

### **5.3.2 Angular Domain versus Spatial Domain**

Signal and noise considerations in the angular domain are the same as in the spatial domain, since the angular domain operates on  $T_b$ 's obtained from different snapshot images. The SNR of RFI is the same in both domains. However, the angular domain presents an advantage over the spatial domain because of the smooth dependence of  $T_b$  on incidence angle and, hence, the ability to accurately estimate what the  $T_b$  of a sample under test should be from its neighboring samples. This permits a more accurate estimation of the expected value of the sample under test. The expected value is used to set the detection threshold for RFI. The detection threshold in both spatial and angular domains is given by the allowed deviation from the expected value of a sample under test. If the expected value is incorrectly predicted then the threshold will be incorrectly set, which can result in false alarms or missed detects. In addition, in the case of the spatial domain the allowed deviation of a sample under test from its expected value needs to be wider since spatial variations in  $T_b$  can be much larger without the presence of RFI due to the potential natural spatial variability of the scene.

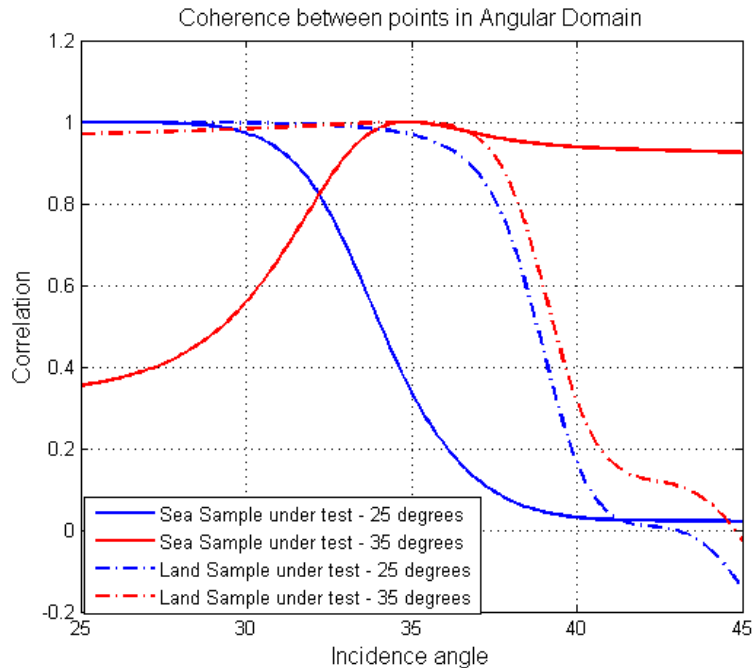


Fig. 5.4: Correlation statistics between an angular domain sample and its neighboring pixels based on two SMOS half-orbits. The blue-curve represents correlation between a sample under test at 25° incidence angle and the red-curve represents a sample under test at 35° incidence angle. The dashed line represents land statistics and solid line represents sea statistics.

The degree to which the expected value of a sample under test can be reliably estimated from its neighbors can be quantified by considering the autocorrelation of the samples. Examples are shown in Fig. 5.4 and Fig. 5.5 for samples in both the spatial and angular domains, derived empirically from a half orbit of SMOS observations.

In case of the angular domain, each sample is correlated to the next sample based on the geophysical relationship between Tb and incidence angles. Correlation between samples in the spatial domain is more or less random (e.g. forest land next lake) and any correlation is introduced by the antenna pattern of SMOS. Fig. 5.4 shows the correlation relationship between an angular domain sample and its neighbors. This relationship is derived from one half-orbit of

SMOS over land, and one half orbit over water. The two colored curves in the figure explain the correlation between a sample at the edge fitted with the help of samples ahead of it, and a sample in the middle fitted with correlated samples before and after it. In order to calculate auto-correlation statistics, a large population of Tb versus incidence angle measurements was used. These measurements were then fit with a cubic function to obtain Tb values at uniform incidence angles. The autocorrelation was then calculated from this large population of individual cubic fits based on their corresponding measurements. Samples show high correlation with values within 10 degrees that drops off as incidence angle difference increases.

Fig. 5.5 shows the correlation statistics in the spatial domain. Similar to Fig. 5.4, a large population set of a Tb samples and its neighboring pixels were collected and quadratically fit. Autocorrelation statistics are calculated from the population of fits obtained from observations.

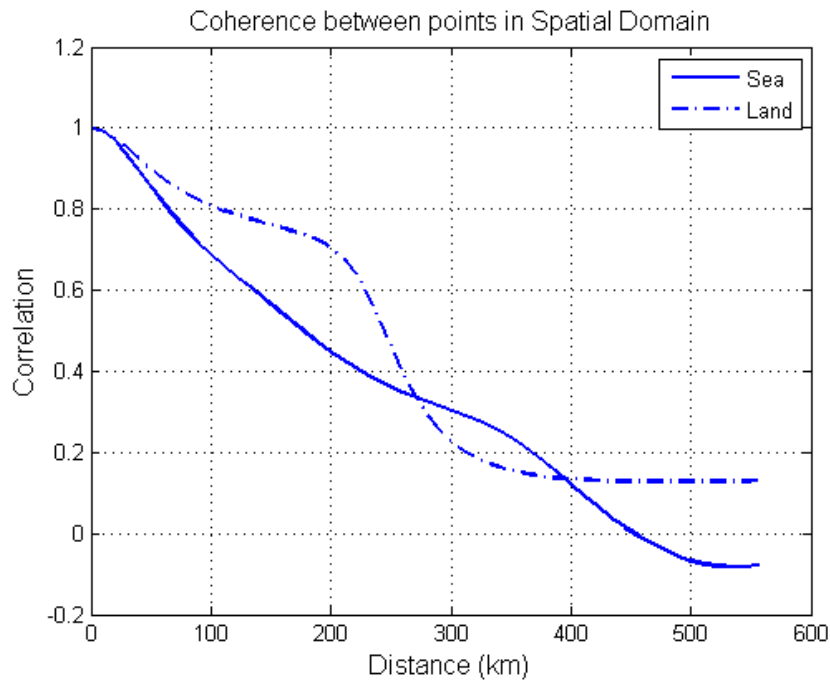


Fig. 5.5: Correlation statistics between a spatial domain sample and its neighboring pixels based on two SMOS half-orbits. The dashed line represents land statistics and solid line represents sea statistics.

Fig. 5.5 shows less of a correlation in the spatial domain compared to the angular domain. As a result, coherence is worse in the spatial domain, leading to a noisier fit, threshold and higher false-alarms and missed-detects.

It should be noted that the spatial fit is performed by calculating the mean, that is, zeroth order, which has lesser unexplained variance compared to a third order fit performed in the angular domain.

## **5.4 Angular Domain Results**

The performance of the angular domain RFI detection algorithm described in Section 5.2.3.1 is demonstrated by several representative examples of overpasses by SMOS of highly localized, un-physically strong “hot spots” in the Tb image. These are likely caused by RFI sources, although precise ground truth assessment of this assumption is not readily available.

### **5.4.1 RFI Detection**

Fig. 5.6a shows a SMOS snapshot of H-pol Tb over South America which includes a clear RFI outlier of ~450K. Fig. 5.6b shows samples at the location of the RFI point (RFI sample circled) when viewed in the angular domain. All samples colored red in Fig. 5.6b are flagged as RFI; all blue samples are assumed to be RFI-free; the green curve represents a fit. Note that both low and high level RFI are flagged by the algorithm.

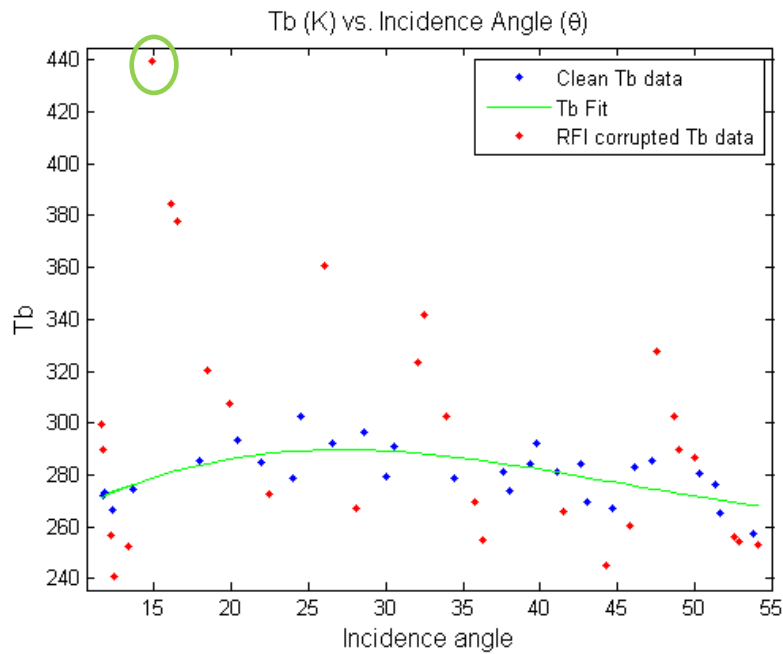
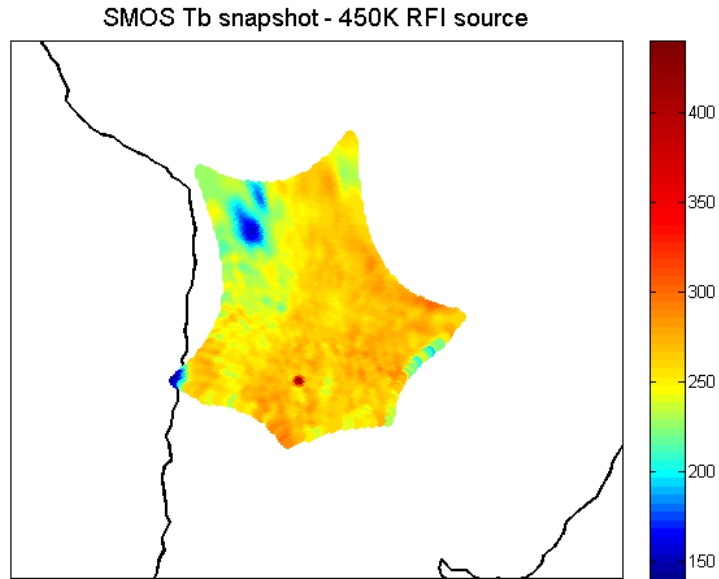


Fig. 5.6: (a) SMOS H-pol Tb snapshot with a clear RFI spot at 450K (bright red) (b) Angular domain representation of the same RFI pixel with flagged RFI Tbs (red), RFI-free Tbs (blue) and cubic fit (green). The circled sample in (b) is the same pixel as the red hot spot in (a)

Fig. 5.7 illustrates a key advantage of the angular domain detector. As observed in the circled region of the snapshot image (Fig. 5.7a), an RFI source is indistinguishable from its neighboring

pixels due to its low power and the high spatial variability of the natural emission. In the angular domain image (Fig. 5.7b), on the other hand, an outlying RFI corrupted sample is clearly evident, as indicated by the red dot.

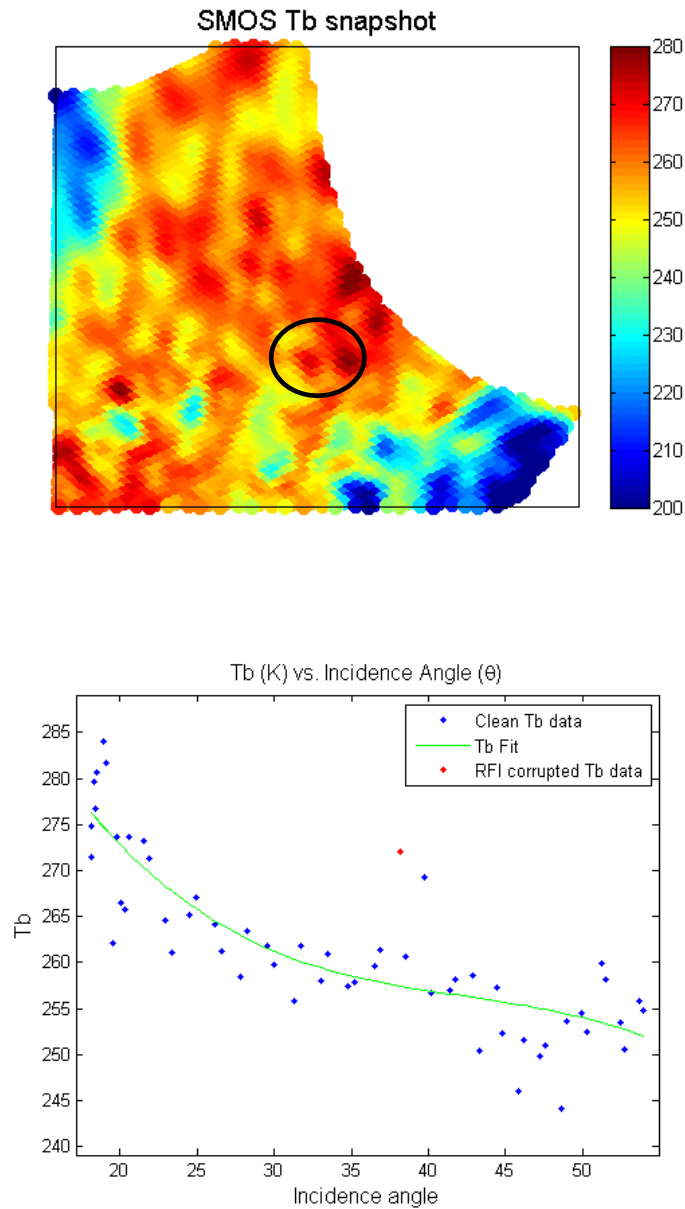


Fig. 5.7: (a) SMOS H-pol Tb snapshot with an indistinct RFI spot within the circle (b) Angular domain representation of the same RFI pixel with flagged RFI Tb (red), RFI-free Tbs (blue) and cubic fit (green).

### 5.4.2 False-Alarm Sensitivity

The angular domain algorithm operates on a single grid point location and is not influenced by any of its neighboring pixels in the snapshot domain. This helps in avoiding false alarms such as the misinterpretation of an island, surrounded by lower Tb water as RFI. Fig. 5.8 gives an example of a lake at cold Tbs surrounded by hotter land. Since RFI can be positively or negatively biased with SMOS, a pixel in the lake might also be falsely identified as RFI in the spatial domain algorithm. As can be seen in Fig. 5.8b, most of the samples are identified as RFI-free by the angular domain algorithm. One sample, near 10 deg incidence angle, is flagged as RFI contaminated. However, it is positively biased in a lake which is cooler than its neighboring pixels. Such an RFI pixel might be hard to detect in the spatial domain.

The false alarm rate (FAR) of the angular domain algorithm can be estimate by considering Tb samples to be a normally distributed random variable with a standard deviation of  $NE\Delta T$ . The expected Tb value of a sample under test (the value of the cubic fit at the incidence angle of the sample under test) can also be considered to be a normally distributed random variable, with a standard deviation ( $\sigma_{MSE}$ ) given by the mean squared error of the fit. The FAR then follows as

$$\begin{aligned}
 FAR &= E\left[\frac{1}{2}\left(1-\operatorname{erf}\left(\frac{z-c}{\sqrt{2}}\right)\right)+\frac{1}{2}\left(1-\operatorname{erf}\left(\frac{z+c}{\sqrt{2}}\right)\right)\right] \\
 &= 1-\operatorname{erf}\left(\frac{z}{\sqrt{2(1+\sigma_{MSE})}}\right)
 \end{aligned} \tag{5.4}$$

where,  $z=3$  and  $c\sim N(0, \sigma_{MSE})$ . Eqn. (5.4) suggests that the FAR will depend on the goodness of the cubic fit. If the fit is perfect (i.e.  $\sigma_{MSE}=0$ ), then the FAR is identical to a normal Gaussian threshold detector. The FAR value calculated for each pixel flagged as RFI can be used as a confidence factor in the detection result. It should be noted though that the MSE might be large

due to the presence of a persistent RFI source (present in multiple incidence angle samples at the same location), thus impacting the cubic fit.

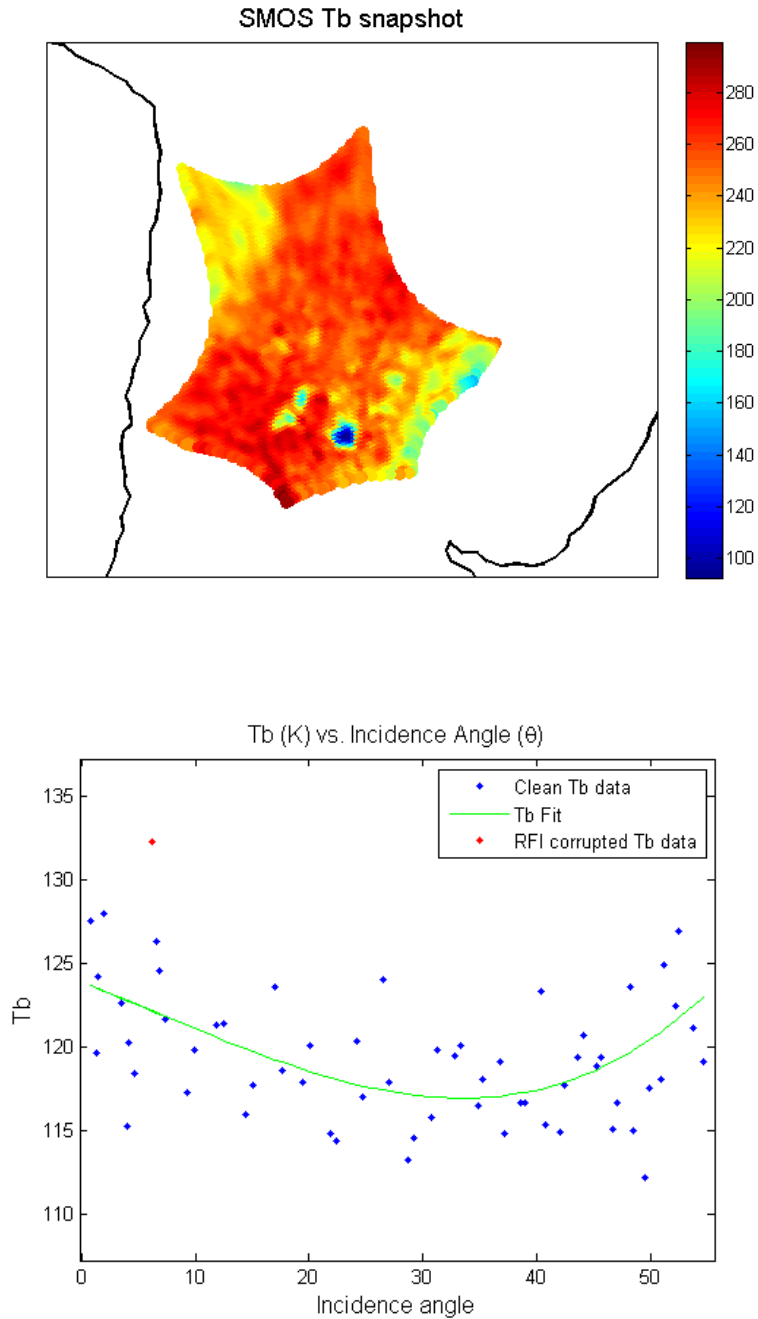


Fig. 5.8: (a) SMOS H-pol Tb snapshot with a low Tb lake surrounded by high Tb land; (b) Angular domain representation of the same lake pixel with flagged RFI Tbs (red), RFI-free Tbs (blue) and cubic fit (green).

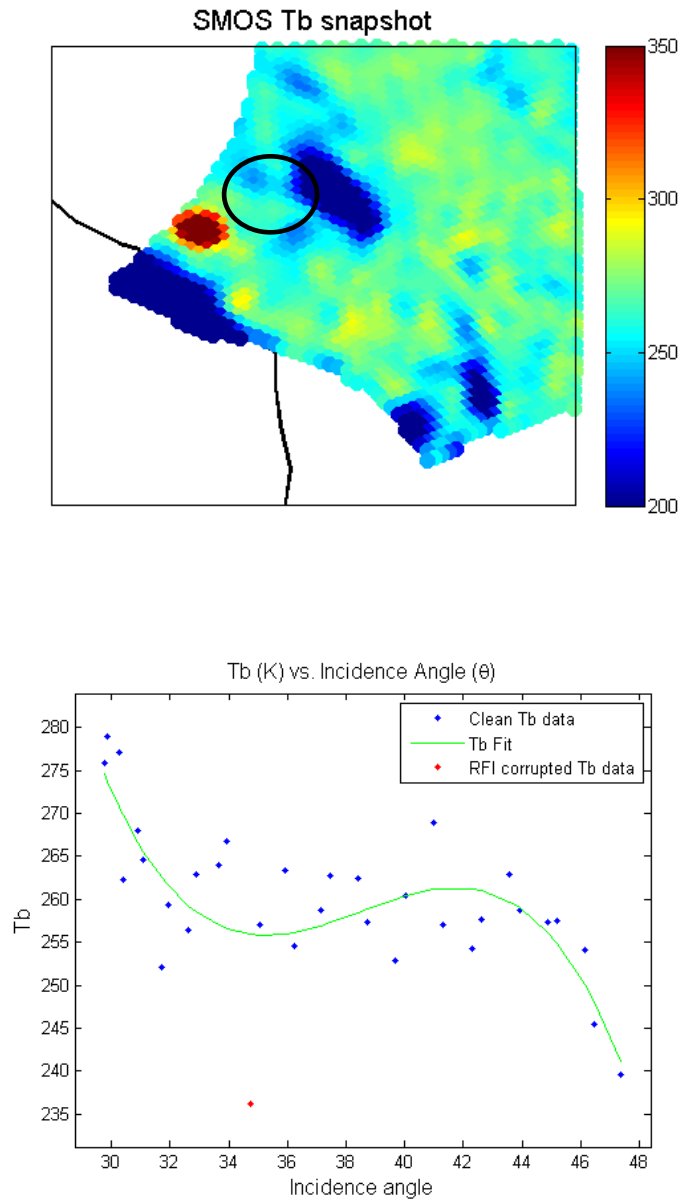


Fig. 5.9: (a) SMOS H-pol Tb snapshot with a negatively biased RFI region (circle) (b) Angular domain representation of one of the pixels in cold RFI region with flagged RFI Tbs (red), RFI-free Tbs (blue) and cubic fit (green).

### 5.4.3 Negatively Biased RFI

The angular domain algorithm also detects and flags negatively biased RFI values. These Tb values are generally cooler than their surrounding spatial pixels or incidence angle

measurements. As noted above, the reason for negatively biased Tb values is likely Gibbs ringing and the actual RFI source is probably not located at the pixel at which the negatively biased Tb is detected. This is hard to confirm with SMOS data due to multiple positively and negatively biased RFI sources present in any snapshot image.

As an example, the circled region in Fig. 5.9a shows an unusually cold Tb region next to a lake and a very bright RFI hotspot to its west. The angular domain plot in Fig. 5.9b, shows the anomalous negatively biased RFI spot, which is clearly an outlier.

#### **5.4.4 RFI snapshot**

The angular domain detection algorithm permits RFI to be detected at much lower levels than algorithms based in the spatial domain. With the angular domain algorithm, snapshot images can be generated of low level RFI. Existing RFI algorithms in use by SMOS, which operate in the spatial domain [73] have generally indicated that the North American continent to is relatively RFI free. While this may well be true for high level RFI, it does not appear to be the case for low level RFI. Fig. 5.10 shows one example of Tb snapshot over the eastern United States, together with the corresponding RFI snapshot generated using the angular domain detection algorithm. Red pixels indicate possible RFI sources and green represents RFI-free locations. Fig. 5.10 shows that the United States might not be as RFI free as previously believed. Note that the locations with RFI indicated in the RFI snapshot are not obviously contaminated (i.e. unnaturally bright) in the Tb snapshot image.

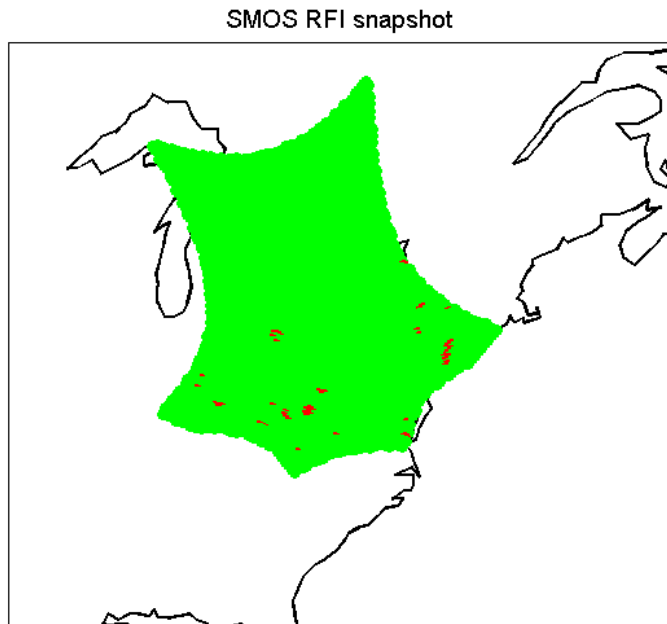
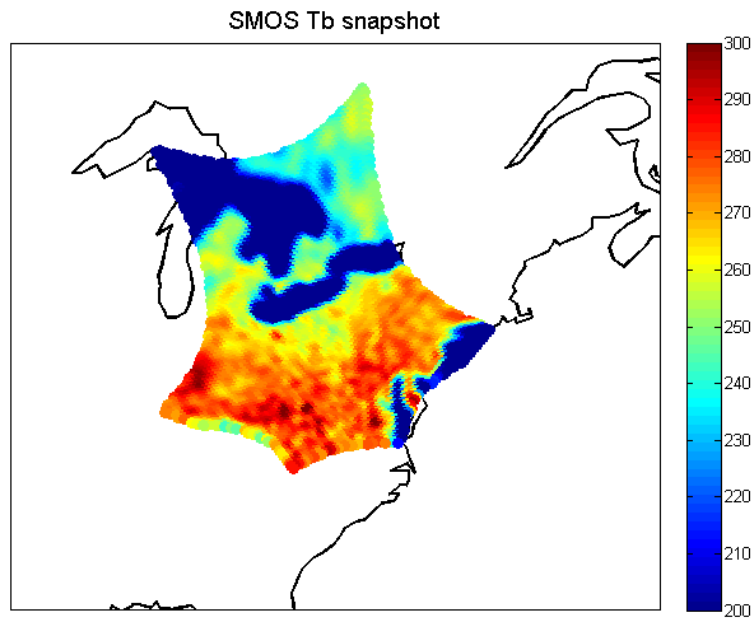


Fig. 5.10: (a) SMOS H-pol Tb snapshot over the eastern United States at 10:50:36 UTC on 8<sup>th</sup> July, 2010 (b) SMOS RFI snapshot at the same time over eastern United States. (red = RFI present, green = RFI free)

### 5.4.5 Algorithm Performance

In general, the absence of reliable RFI “ground truth” makes it very difficult to quantitatively assess the detectability statistics of an RFI algorithm. Comparisons of histograms of Tb samples, containing flagged and unflagged samples, give some information about the behavior of the algorithm. Fig. 5.11 shows Tb histograms accumulated over a single half orbit. The blue curve is derived from all of the Tb data; the green curve is derived only from Tb data classified as RFI free. The two curves have generally similar shapes since a large percentage of data is RFI free. The bi-modal distribution of the histogram is a result of the large TB difference between land and water.

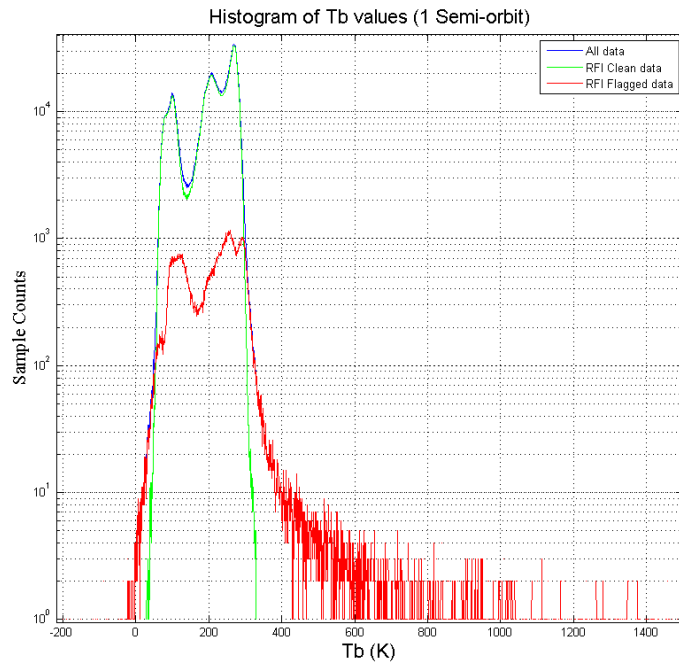


Fig. 5.11: Histogram of Tb values over a single half orbit, sweeping from the south to north pole between 17°W and 95°W approximately, measured on 8<sup>th</sup> July, 2010 from 10:10 to 11:05 UTC. (Blue = All Tb data, Green = RFI free Tb data, Red = RFI corrupted Tb data)

The red curve indicates Tb data classified as containing RFI by the angular domain detection algorithm. Two things are noteworthy. (1) The algorithm immediately discards extremely high,

or extremely low outlier Tb samples since the algorithm uses a hard threshold for initial detection; and (2) Most of the RFI detected between 50K and 300K has similar characteristics to the clean Tb data. This suggests that the algorithm is able to detect low-level RFI corrupted samples as well.

## **5.5 Summary and Discussion**

The interferometric nature of SMOS allows for RFI detection algorithms to operate in a number of signal domains. RFI detection can be applied in the early L1a data processing stage, in the Visibility domain, where temporal samples of zeroth visibility are monitored for outliers. Converting to spatial Tbs from visibilities allows for the detection of RFI “hot spots” by comparing a pixel with its neighboring (in space) pixels. A third detection domain is available because SMOS measures the Tb at a single location over multiple incidence angles. Tb has a specific geophysical relationship with incidence angle, and an angular domain RFI detection algorithm has been implemented which checks for deviations of the Tbs from the Tb-incidence angle variations as explained by the cubic fit.

The noise level of Tbs increases by a factor of approximately 25 (from 0.2K to 5K) when going from the visibility to the spatial domain. The power of a single-point RFI source, on the other hand, is enhanced by a factor of ~2300 when going from the visibility to the spatial domain. Thus, it is easier to detect RFI in the spatial domain due to a higher RFI SNR. The angular domain has the same SNR as the spatial domain. The angular domain algorithm has an advantage over the spatial domain algorithm in that there is a more deterministic relationship between a sample under test and its neighbors in the angular domain. This relationship allows a more accurate prediction of the expected value of a sample under test from its neighbors, thus aiding in detection and false alarm statistics.

The algorithm identifies positively biased as well as negatively biased RFI points. Low-level (near NE $\Delta$ T) RFI is more easily detected. RFI snapshots, made by applying the angular domain algorithm to regional SMOS images, indicate RFI at locations previously considered to be relatively RFI free. Histogram comparisons of Tb data flagged and unflagged for RFI suggest that other, aside from some strong outlier (high and low) Tb values, most of the RFI flagged is low-level.

### **Appendix: Coherence impact on mean-squared error (MSE) of fit**

The mean-square error (MSE) in the fit is dependent on the covariance (or correlation) statistics of the signal. In both detection domains, the sample under test is estimated using a fit applied on incidence angle values. For the spatial domain, these incidence angles are for different neighboring pixels in the same snapshot. For the angular domain, the incidence angles are for different snapshots but the same pixel. The MSE statistic of the fit can be found as follows,

$$\begin{aligned}
MSE &= E\left[(\hat{T} - T)(\hat{T} - T)^*\right] \\
&= E\left[(\Theta C - T)(\Theta C - T)^*\right] \\
&= E\left[\left(\Theta\left[(\Theta^* \Theta)^{-1} \Theta^* T\right] - T\right)\left(\Theta\left[(\Theta^* \Theta)^{-1} \Theta^* T\right] - T\right)^*\right] \\
&= E\left[(MT - T)(MT - T)^*\right] \\
&= (M - 1)E\left[TT^*\right](M - 1)^* \\
&= (M - 1)S_T(M - 1)^*
\end{aligned} \tag{A.1}$$

where,

$$M = \Theta(\Theta^* \Theta)^{-1} \Theta^*$$

and,  $E[\cdot]$  is the expectation operator,  $T$  is the brightness temperature vector in the spatial domain or angular domain,  $C$  is the fit coefficient vector,  $\theta$  is the incidence angle matrix described in eqn. (5.2) and  $S_T$  is the covariance matrix.

Communication systems often obtain optimum systems based on the minimization of the trace of the MSE matrix (standard MSE) or determinant of the MSE (geometric MSE) [81]. For domain comparison purposes we will apply a similar principle and calculate the smaller geometric MSE (GMSE) between the spatial and angular domains. This can be calculated as follows,

$$\begin{aligned} \det(MSE) &= \det((M-1)S_T(M-1)^*) \\ &= (\det(M-1))^2 \det(S_T) \end{aligned} \quad (A.2)$$

where,  $\det(\cdot)$  represents determinant of the matrix. As noted in eqn. (A.2) the GMSE depends on the covariance matrix. In order to demonstrate the impact of correlation on determinant of covariance matrix, consider a covariance matrix with elements of the row represented by a Gaussian distribution. The peak of the distribution is at the diagonal element of the row. Each element of the covariance matrix can be represented as follows,

$$(S_T)_{ij} = e^{-(i-j)^2/2\sigma^2} \quad (A.3)$$

Where,  $S_T$  is the covariance matrix,  $i$  represents the row,  $j$  represents the column and  $\sigma$  represents the standard deviation (or number of adjacent samples across which correlation drops to ~66%). If  $\sigma$  is small or negligible, this represents a near-orthogonal matrix with eigenvalues around 1 and thus a determinant (product of eigenvalues for square matrix) near 1. For matrices with larger  $\sigma$  the non-orthogonality of the matrix increases resulting in a few small eigenvalues and thus smaller determinant. Fig. 5.12 represents the decreasing value of the determinant as standard deviation (correlation between adjacent samples) increases.

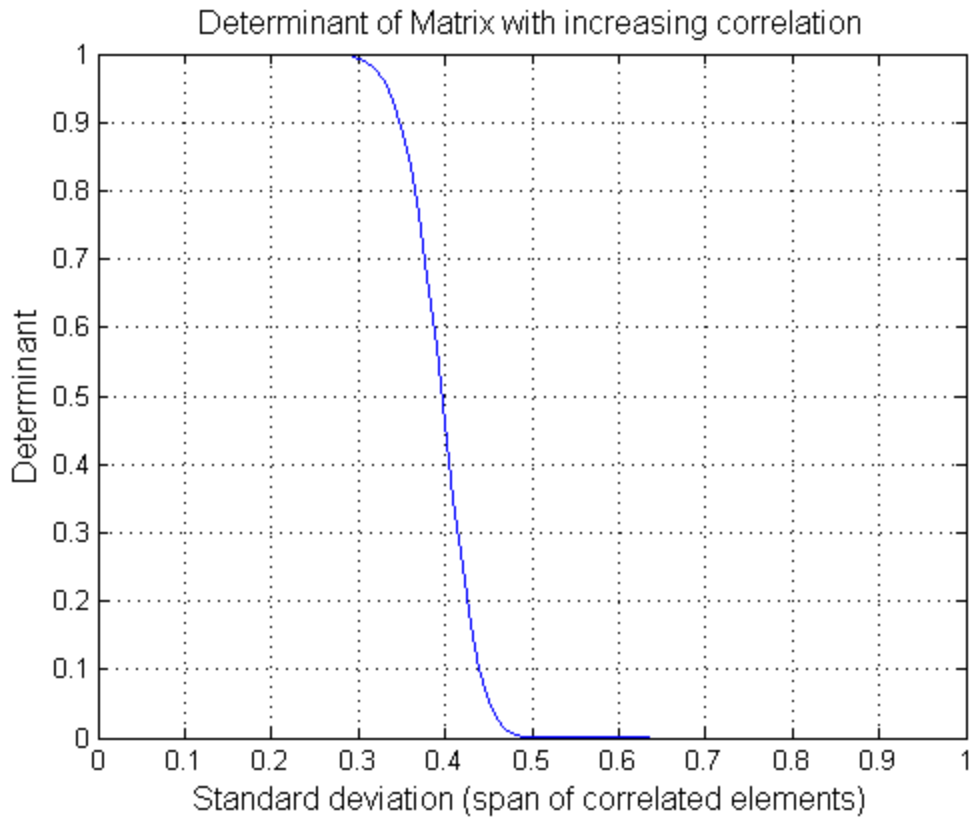


Fig. 5.12: Determinant of a covariance matrix with elements of the row represented as a Gaussian distribution with the mean around the diagonal matrix element.

As a result, GMSE is high if the covariance matrix is like an identity matrix, with little to no correlation between adjacent samples. GMSE is lower when there is correlation between adjacent samples. Thus the angular domain algorithm fit is lower than a spatial domain algorithm fit.

## **Chapter 6**

### **Conclusions**

#### **6.1 Brief Review**

Radio Frequency Interference (RFI) signals are man-made sources that are increasingly plaguing passive microwave remote sensing measurements. This RFI is insidious in nature, with some signals low power enough to go undetected but large enough to impact science measurements and resulting conclusions. With the launch of the European Space Agency (ESA) Soil Moisture and Ocean Salinity (SMOS) in November 2009 and the upcoming launches of the new NASA sea-surface salinity measuring Aquarius mission in June 2011 and soil-moisture measuring Soil Moisture Active Passive (SMAP) around 2015, active steps are being taken to detect and mitigate RFI at L-band.

An RFI detection algorithm was designed for the Aquarius mission. The algorithm was tested using a kurtosis detector-based form of RFI ground-truth to analyze its performance. The algorithm has been developed with several variable parameters to control the detection statistics (false-alarm rate and probability of detection). The parameters are allowed to be location dependant to control strictness of the algorithm based on amount of RFI expected.

The kurtosis statistical detection algorithm has been compared with the Aquarius pulse detection method based on the detection of pulsed-sinusoidal type RFI. The comparative study determines the feasibility of the kurtosis detector for the SMAP mission, as a primary RFI detection algorithm in terms of detectability and data bandwidth. The

kurtosis algorithm has superior detection capabilities for low duty-cycle radar type pulses, which are more prevalent according to analysis of field campaign data. The kurtosis algorithm can also detect spread-spectrum type communication signals, although at a somewhat reduced sensitivity.

The RFI algorithms have generally been optimized for performance with individual pulsed-sinusoidal RFI sources. A new RFI detection model is developed as a result of observations of anomalous behavior by the kurtosis detection algorithm during an RFI flight campaign. The new model takes into account multiple RFI sources within an antenna footprint. The performance of the kurtosis detection algorithm under such central-limit conditions is evaluated.

The SMOS mission has a unique hardware system, and conventional RFI detection techniques can not be directly applied. Instead, an RFI detection algorithm for SMOS is developed and applied in the angular domain. This algorithm compares brightness temperature values at various incidence angles for a particular grid location. This algorithm is compared and contrasted with algorithms in the visibility domain of SMOS, as well as the spatial domain. Initial results indicate that the SMOS RFI detection algorithm in the angular domain has a higher sensitivity and lower false-alarm rate than algorithms in the other two domains.

## 6.2 Contributions

- A “glitch” detector or pulse-detection algorithm specifically tuned to the Aquarius data characteristics was designed for RFI detection and mitigation [64, 82].

- The Aquarius mission will be implementing the RFI detection algorithm detailed in this thesis [64, 69].
- Better detection performance of the kurtosis detector compared to the pulse-detector algorithm for low duty-cycle pulsed sinusoidal RFI was confirmed using a new parameter AUC (Area Under the Receiver Operating Characteristic (ROC) Curve) [69, 83].
- The optimal number of sub-banding filters required for implementation of the kurtosis algorithm for RFI detection was presented[83].
- Reduced data bandwidth requirement of the kurtosis detection algorithm with respect to a pulse detection system was established[69].
- The low sensitivity of the kurtosis detector to spread-spectrum type communication signals was demonstrated[31, 46].
- The presence of RFI in the protected L-band was established based on various airborne field campaigns [32, 41, 56, 59].
- RFI characteristics of L-band over the continental USA was established, noting more pulsed-type RFI compared to continuous-wave RFI.
- A new RFI model was developed that takes into account multiple pulsed-sinusoidal sources [70, 84].

- Reduced sensitivity and increased missed-detects of the kurtosis detection algorithm under central-limit conditions of the new RFI model was established[84].
- A new type of RFI detection algorithm for the SMOS mission was developed that operates in the angular domain comparing brightness temperature values with respect to incidence angle at a single grid location.
- A comparative domain analysis of the different detection domains of SMOS was performed, establishing the higher sensitivity and lesser false-alarms rates of the algorithm in the angular domain compared to the visibility and spatial domain respectively.

### **6.3 Future Work**

The following represents a discussion of potential topics to be investigated in the future.

#### **6.3.1 Optimal RFI detection algorithm**

Various RFI detection techniques exist that operate in different domains. An optimal temporal and spatial resolution combined with a kurtosis detector can improve the RFI AUC considerably. Kurtosis detectability suffers if the temporal or spatial resolution is too fine since the noise level increases with a smaller bandwidth and fewer samples. On the other hand the performance of spectral and temporal algorithms improves for narrow-pulse or narrow-band sources due to a fine resolution. *What is the optimum point of operation that needs to be studied to balance out these competing yet complementary factors ?*

This study can be approached in two ways, (1) A theoretical study based on RFI models, or (2) Empirical study of a large population data set with extremely fine spatial and temporal resolution and higher order moment detection. The first approach aids in developing a statistically optimum scenario for RFI detection and is relatively easy to undertake. A disadvantage to this method is that a lot of assumptions need to be made about the nature of the interfering signal. Incorrect or inaccurate assumption would lead to false settings. The second approach is much harder and more expensive to implement. The above approach needs actual flight campaign data measuring at a very fine spatial and temporal resolution. Constructing such systems is not trivial, and such flight-campaigns are not cheap. The frequency, bandwidth, footprint, type of flight, time of flight etc also need to be taken into account before drawing optimum setting conclusions. Another obvious pitfall to the above technique is the lack of RFI ground-truth. The advantage is that by measuring higher order moments with a very high temporal and spectral resolution it is possible to combine and contrast various integration and spectral periods to detect RFI.

Finally, another important research question that needs to be tackled is: *what is the best combination of the different detection algorithms to create an optimum algorithm?* One possible technique is to combine results from three different algorithms (pulse detection, cross-frequency detection, kurtosis detection) in a weighted sense. The weights to these individual algorithms can be applied based on any of these following factors: NE $\Delta$ T sensitivity, noise margin, false-alarm rate, probability of detection etc. This is not a trivial research question and either some sort of ground-truth or accurate RFI model is needed to determine the optimum detection algorithm and resolution.

### **6.3.2 SMOS Angular domain algorithm improvement**

A future progression of the angular domain algorithm presented in Chapter 5 would be to utilize retrieved L2 soil moisture or sea salinity data. Applying a forward model emission algorithm, the measured Tbs should be compared with the modeled Tb instead of a cubic fit. This would aid in more accurate detection of RFI corrupted Tbs.

In order to implement such an algorithm, it is necessary to know all the secondary parameters that are applied into the forward model, such as sea-surface roughness, vegetation canopy, surface temperature, soil-type etc. The accuracy of the RFI detection algorithm is directly related to the accuracy of these secondary factors. Based on results from a proper forward model, the observed Tb values can be compared to the modeled Tb values to detect any outliers. An iterative method between the forward model and retrieval algorithm might aid in the detection of lower level RFI signals.

Possible issue that might occur with the following algorithm is the convergence of the retrieval algorithm. If the Tb signals versus incidence angle are corrupted enough by RFI, a retrieval algorithm might not be able to converge close to the actual soil-moisture value. This could result in an erroneous modeled Tb and RFI flagging. Impact of such scenarios, as well as improvement over the cubic-fit method must be quantified. Further performance analysis of this and other algorithms needs to be performed by combining detection statistics of all algorithms to assess probability of detection and false alarm rates.

A final problem with such an algorithm might be speed of computation. The algorithm might not be feasible for implementation in the official SMOS data processing chain if the computation time is too long.

### **6.3.3 SMOS RFI second-order effects**

The one-bit correlator used by the SMOS receiver pairs measure digital correlation values. The digital correlations are converted to analog correlations based on the Van-Vleck function [85] which assumes Gaussianity of the incoming thermal emissions. A single source RFI does not behave as a normal signal, and would upset the digital-analog mapping to obtain the visibility function. This in turn could produce erroneous Tb images based on a single RFI point.

The impact of such RFI on digital correlator mapping can be recalculated by using a pulsed-sinusoidal RFI model. SMOS has a fairly high resolution, and it can be expected that a single source exists within a pixel (unless above heavily populated areas). Based on the new digital-analog correlation map and the theoretical Van-Vleck one-bit map it is possible to calculate the impact of a single RFI point source on all visibility functions. It is expected that the Tb image produced after an inverse Fourier transform would have biased values at pixels other than the RFI pixel as well. It is possible that the eventual affect due to erroneous digital mapping is second order compared to a much more primary phenomenon such as Gibbs ringing.

### **6.3.4 Alternative RFI detection techniques**

Temporal detection algorithms suffer in performance if not optimally matched to the pulse width of the RFI. Spectral algorithms suffer when detecting wide-band RFI. The

kurtosis detector is affected by central-limit conditions and is less sensitive to CW sources. Similarly, the algorithm based on 3<sup>rd</sup> and 4<sup>th</sup> Stokes fails to pick up non-polarized RFI. In addition to these techniques, it is necessary to investigate and develop other implementable versions of detection algorithms.

A possible new technique of detecting low-level RFI is by calculating the lag-autocorrelation of the incoming digitized IF signal for each integration period. If the signal is RFI-free within the integration period then the normalized autocorrelation function should look similar to a sinc function with elements outside the  $1/B$  time period having little or no correlation ( $B$ =bandwidth of radiometer). If RFI elements are present then due to the sinusoidal nature considered, there should be some sort of correlation depending on the pulse-width of the individual RFI sources.

A lag-correlator should be relatively easy to implement in firmware. Fig. 6.1 shows a simple block-diagram implementing the auto-correlator. The design implements a few delay elements to operate on the digitized IF signal after the A/D converter. The delayed samples are then multiplied and accumulated with the original sample to calculate lag-autocorrelation value over each integration period. In order to initially experimentally verify this algorithm, a fast direct sampler ( $>1\text{GHz}$ ) with a large memory unit is required to obtain data before accumulation. This algorithm must be further investigated in terms of noise margins, number of samples, detectability statistics etc.

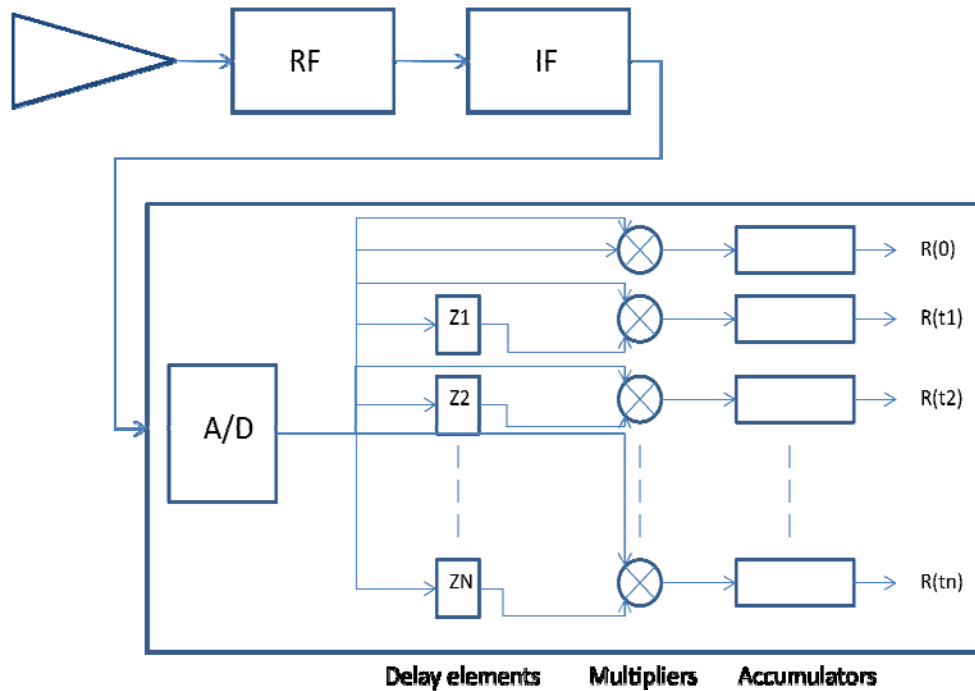


Fig. 6.1: Simplified Block diagram indicating implementation of a digital lag correlator

### 6.3.5 On-board RFI processing

With increasing restrictions on data bandwidth and the necessary spatial and temporal resolution requirements of an RFI detection algorithm, on-board RFI processing is something that should be further investigated. On-board processing would allow the data to be flagged in the firmware itself, allowing on-board data mitigation and require only down-linking the mitigated data along with the original counts. Efforts with respect to such systems are already underway in a joint project between Jet Propulsion Laboratory (JPL) and University of Michigan.

The implementation of such a system requires an on-board Real Time Operating System (RTOS) and a PC-104 for data packaging. Research needs to be done on an evaluation version to test the feasibility of such an implementation in terms of on-board calculation complexity, speed, resource usage etc.

There are a few potential issues that can occur with such an on-board system. RFI mitigation is performed by discarding corrupted (temporal/spatial) grids and combining the rest. This can affect the calibration from counts to brightness temperature of the radiometer. An on-board mitigation algorithm would also lose post-processing flexibility in controlling the strictness (false-alarm rate, detection probability) of the detection algorithm. The detection threshold would be set on-board which controls detectability of the algorithm. Possible solutions are to send house-keeping data keeping track of lost grids to aid calibration, and have the on-board system apply a few different strictness-levels of the detection algorithm, and send all the resultant counts down. Considering temporal and spectral integration, data bandwidth should still be conserved.

#### **6.3.6 Aquarius RFI detection algorithm parameter determination**

The Aquarius detection algorithm has four variable parameters that control the conservative nature of the algorithm. These parameters can be tuned based on the amount of RFI present. A less strict algorithm can be used when looking at relatively RFI free ocean surfaces, and stricter algorithm near the RFI-heavy coastal regions. RFI statistics from the already launched SMOS data can be used to determine the appropriate values of Aquarius algorithm parameters.

This study has two components to it, (a) Developing a SMOS RFI detection algorithm to collate RFI statistics across the Earth, and (b) To link RFI occurrence statistics to the Aquarius parameters via some metric. The RFI detection algorithm described in Chapter 5 can be used along with a spatial RFI detector to provide the necessary RFI statistics.

Linking occurrence statistics to determination of parameter values is not trivial. The parameters control the false-alarm rate of the algorithm. Scaling RFI occurrence proportionally to FAR the Aquarius algorithm parameters can be determined. Frequency of occurrence can directly influence the  $W_r$  range-window parameter that controls the number of samples discarded before and after a detected RFI sample. Similarly, if the expected RFI is continuous, then a larger window-size ( $W_s$ ) should be chosen to accurately calculate mean Tb. There are many such scenarios that can influence the parameter determination of Aquarius. One approach would be to classify SMOS RFI in terms of occurrence, frequency, power, neighboring pixels corruption etc., and combine these values to determine Aquarius parameters. SMOS has a finer pixel resolution than Aquarius, which will aid in determination of the parameters.

# **Appendix I**

## **Characterization of L-band RFI across the continental USA using a kurtosis detector**

### **I.1 Introduction**

The University of Michigan's Agile Digital Detector (ADD) was one of three radiometer back ends that were integrated with the JPL Passive/Active L/S Band (PALS) combined radar and radiometer [62] for flights on board a Twin Otter during 22 September through 19 October 2008. The other two back ends were the L-Band Interference Suppressing Radiometer [49] and the Analog Double Detector [52]. The Twin Otter campaign involved transit flights between Grand Junction, Colorado and Wilmington Delaware, numerous soil moisture science flights near Des Moines, Iowa and Choptank, Maryland, and several RFI-specific flights near New York City, Atlanta and elsewhere. RFI-related measurements were also made by ADD during all transit and science flights. Results of the analysis of ADD measurements to characterize the extent and properties of the RFI that was encountered during the campaign are presented here. Specific attention is paid to the differences between pulsed RFI (typically radar in origin) and continuous wave (typically communication signals), which can be distinguished by the kurtosis detector in ADD [32]. Attention is also paid to the performance of an Aquarius radiometer-like RFI detection and mitigation algorithm, which has been adapted for use by the PALS/ADD sensor from the baseline Level 1 Aquarius RFI flight algorithm described in Chapter 2.

The next section presents a brief description of the ADD hardware as well as detection algorithms involved for RFI mitigation. Section I.3 details the analysis results of measurements made during the Fall 2008 Twin Otter campaign with the JPL PALS instrument, before summarizing in section I.4.

## **I.2 Hardware and Detection Algorithms**

ADD is a radiometer back end digitization and digital signal processing subsystem. Its input signals are vertical and horizontal polarization IF versions of the pre-detected radiometer signals. The signals are synchronously digitized with 8-bit precision at slightly higher than the Nyquist rate given their bandwidth. The v- and h-pol signals are then passed through 8-channel digital subband filters, after which each subband is cross-correlated. The kurtosis of each individual v- and h-pol subband signal is also computed, for purposes of RFI detection. In addition, fullband versions of the v- and h-pol signals are also cross-correlated and each of their kurtosis values is also computed.

In the case of integration with PALS, the IF signal output by PALS is centered at 200 MHz and has a 24 MHz bandwidth. The maximum analog frequency of the version of ADD that was flown with PALS was less than 200 MHz, so an additional demodulation stage was added which mixed the IF signal from a 200 MHz carrier to a 27 MHz carrier. The 2<sup>nd</sup> IF signal was then digitized at 110 MHz.

The kurtosis detection consists of flagging samples for which the deviation of the kurtosis from its nominal RFI-free value is statistically significant. The threshold for significance is set at 3 times the standard error in individual estimates of the kurtosis (the so-called NEΔK). RFI so identified is further sub-divided into pulsed or CW depending on

whether its kurtosis is greater than or less than the RFI-free value, respectively. The peak detection algorithm is a direct adaptation of the one that is baselined for use by the Aquarius radiometer. The algorithm is essentially a local “glitch detector”, which derives a local expected value for each sample by averaging together nearby RFI-free samples and then flags that sample as contaminated by RFI if it differs significantly from that expected value. One important characteristic of a peak detection algorithm is the integration time of the raw samples on which it is based. For the ADD deployment with PALS reported here, that integration time is 4 ms. There are also a number of adjustable parameters in the algorithm which affect its false alarm rate and probability of detection. The values used here are consistent with those recommended for the baseline Aquarius algorithm in Chapter 2.

### **I.3 Campaign Results**

This section summarizes the RFI mitigation results obtained using each of the kurtosis and peak detection algorithms. The peak detection version, based solely on the Aquarius-like algorithm, is used to assess the performance of this type of an algorithm in case SMAP uses a back-end detection and sampling design similar to Aquarius.

A combination of the peak and kurtosis detection algorithms was used as a “ground truth” detection algorithm relative to which other types of detection algorithms were compared. Note that this “ground truth” should be expected to contain a small number of false alarms – samples flagged as containing RFI that are actually RFI-free.

The RFI has been classified into pulsed, continuous wave (CW) and “blind/false” RFI. Blind/false RFI is RFI that was detected by the peak detection algorithm but not by the

kurtosis algorithm. Some of it appears to be RFI with a 50% duty cycle with respect to the kurtosis integration time, to which the kurtosis algorithm is blind [31-32], and some of it is apparently the result of a false alarm by the peak detection algorithm.

In addition to the above types of RFI, residual RFI is also analyzed, which occurs if only the peak detection algorithm is used for mitigation. Each mitigation type is discussed in detail in the following subsections.

### I.3.1 Detected RFI

RFI is divided into the following sets:

$$P = \{x_i \mid \kappa(x_i) > (3 + 3\sigma_k)\} \quad (\text{I.1})$$

$$C = \{x_i \mid \kappa(x_i) < (3 - 3\sigma_k)\} \quad (\text{I.2})$$

$$P_k = \{x_i \mid \rho(x_i) = 1\} \quad (\text{I.3})$$

where

$$\begin{aligned} \kappa(x_i) &= \text{Kurtosis of } x_i \\ \sigma_k &= \text{std.dev of kurtosis} \\ \rho(x_i) &= \text{Peak Det flag} \end{aligned}$$

$x_i$  represents the individual ADD thermal emission samples integrated over a 4ms period,  $P$  represents, pulsed-type RFI samples (duty cycle < 50%) when kurtosis is above 3,  $C$  represents continuous wave RFI samples (duty cycle > 50%) when kurtosis is below 3 and  $P_k$  represents samples flagged by the peak detection algorithm.

In order to mitigate all types of RFI, the following detection set is applied

$$A = P \cup C \cup P_k \quad (I.4)$$

In general, the magnitude and frequency of occurrence of RFI will depend on the integration time over which individual samples are formed. In the case of the ADD-PALS data, three different periods of integration are considered: 30sec, 11min and full-flight (approximately 5 hours in each case). A 30 sec integration roughly corresponds to the time required for the aircraft forward motion to equal the average ground footprint diameter. Aircraft forward motion over 11 min roughly corresponds to the expected ground footprint diameter of the radiometer on the SMAP mission. Over a ~5 hour integration time, the ADD-PALS footprint will sweep out approximately the same total area as that of the instantaneous SMAP radiometer footprint. Using the three integration times, we get the curves shown in Fig. I.1, aggregated over 16days. The Complimentary Cumulative Distribution Function (CCDF) in Fig. I.1 represents the fraction of time during which the brightness temperature contribution of RFI ( $T_{RFI}$ ) is above a certain value. In other words, the curves represent the amount of a particular type of RFI generally found during the mission.  $T_{RFI}$  is given as a function of the set  $A$ , i.e.  $T(A) = T_{RFI}$ .

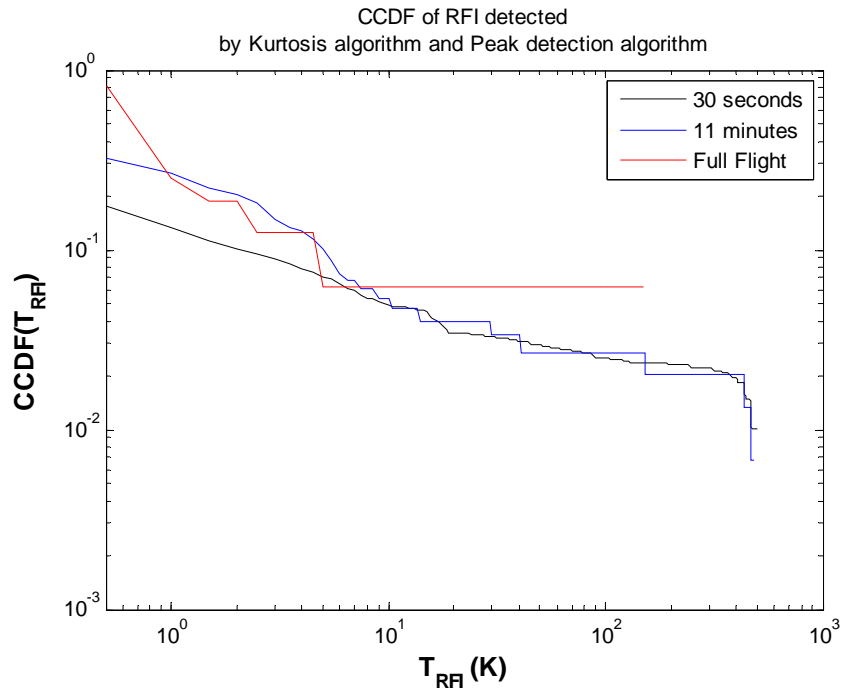


Fig. I.1: CCDF of brightness temperature contribution of all types of RFI detected using the kurtosis and peak detection algorithms

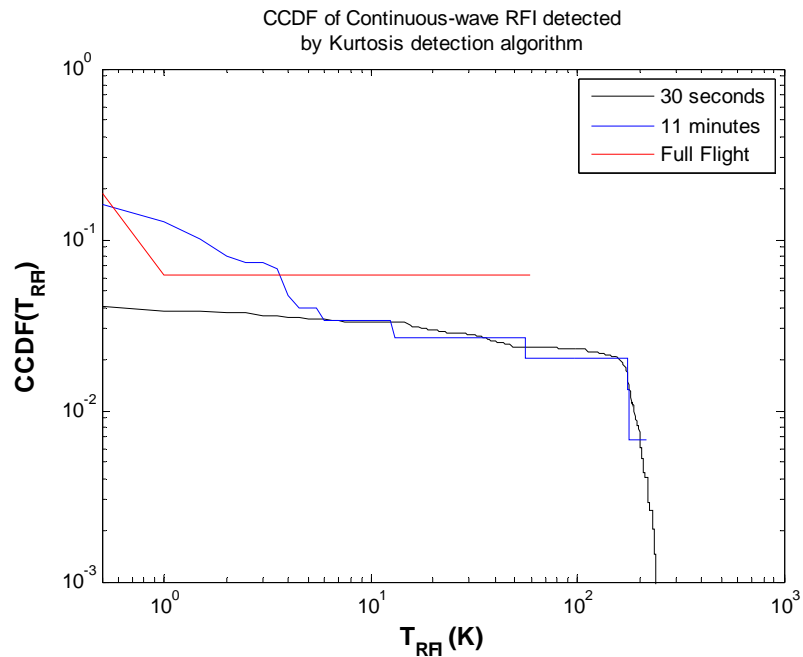


Fig. I.2: CCDF of brightness temperature contribution of continuous wave RFI detected using the kurtosis detection algorithm

$T_{RFI}$  due to just continuous wave ( $C$ ) and just pulsed-type ( $P$ ) RFI is shown in Fig. I.2 and Fig. I.3 respectively. Note that there is considerably more pulsed-type of RFI than CW. However, there is still significant contribution from CW type RFI, with equivalent brightness temperatures as large as 300K.

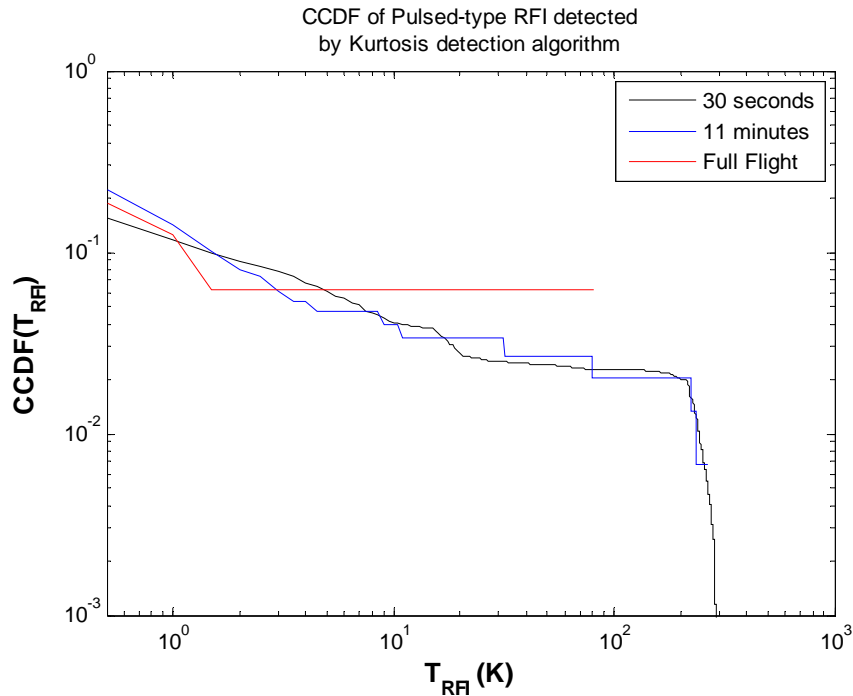


Fig. I.3: CCDF of brightness temperature contribution of pulsed type RFI detected using the kurtosis detection algorithm

### I.3.2 Blind-type RFI and Residual-type RFI

Comparing the kurtosis detection algorithm to “ground truth” we get undetected RFI corrupted Tb samples as well. These undetected samples are called blind/false RFI. Blind/false RFI is RFI that was detected by the peak detection algorithm but not by the kurtosis algorithm. Some of it could be RFI with a 50% duty cycle with respect to the kurtosis integration time or multiple-source RFI, to which the kurtosis algorithm is blind, and some of it is apparently the result of a false alarm by the peak detection algorithm. Fig. I.4 indicates the percentage of blind RFI present above some Tb power indicated by

the x-axis. As noted in the figure, a few high powered RFI sources are missed by the kurtosis algorithm. These sources are too high to be a peak-detection false alarm, and some sources do not behave like a 50% duty-cycle source when tested under combined integration periods [70]. This anomalous behavior is discussed in Chapter 4.

Residual type RFI represents brightness temperature contributions missed by the peak detection algorithm. This type of RFI is important to characterize to understand the amount of RFI corrupting thermal measurements when using only base-line detection algorithms. Such residual RFI ( $R$ ) is calculated by taking the difference between total RFI contribution ( $A$ ); obtained using peak detection and kurtosis;

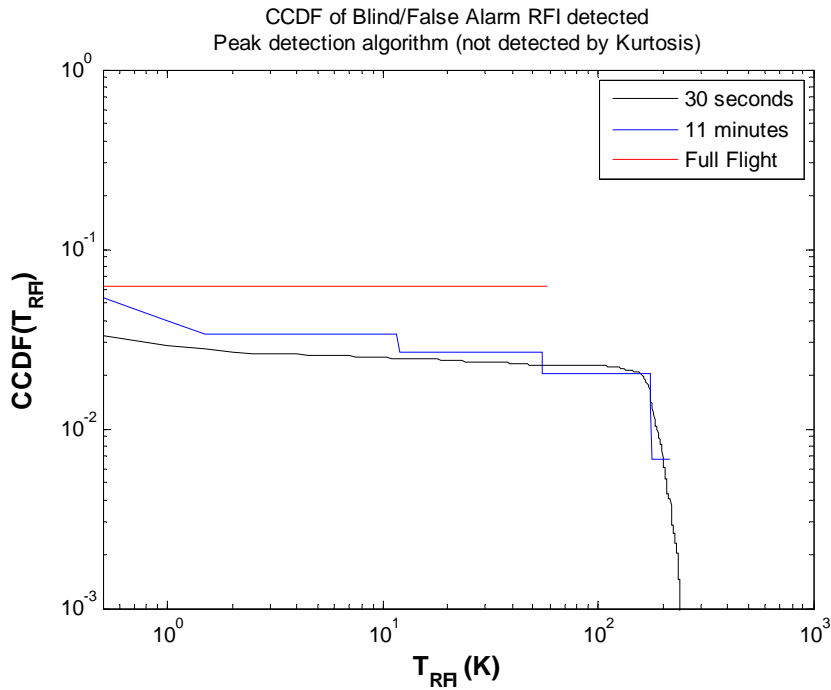


Fig. I.4: CCDF of brightness temperature contribution of blind RFI, i.e. RFI detected using the peak detection algorithm but not detected by Kurtosis

with the RFI contribution from just the peak detection algorithm ( $P_k$ ). The residual RFI brightness temperature is determined using

$$T(R) = T(A) - T(P_k) \quad (I.5)$$

Fig. I.5 shows the residual type RFI. As can be seen, significant amounts of residual RFI still remain even after the peak detection algorithm.

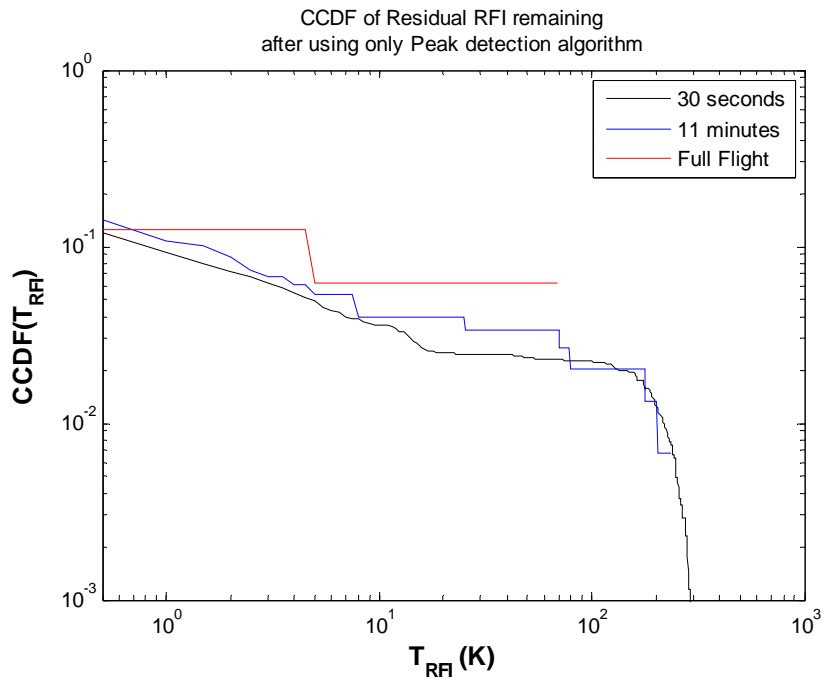


Fig. I.5: CCDF of residual RFI detected using only the peak detection algorithm

Finally, Fig. I.6, compares the relative contributions of all types of RFI for a common 11min integration period. As can be seen from the figure, pulsed-type RFI is the most common type of RFI observed during the missions. Also note that, with peak-detection algorithm only, a significant amount of RFI still remains.

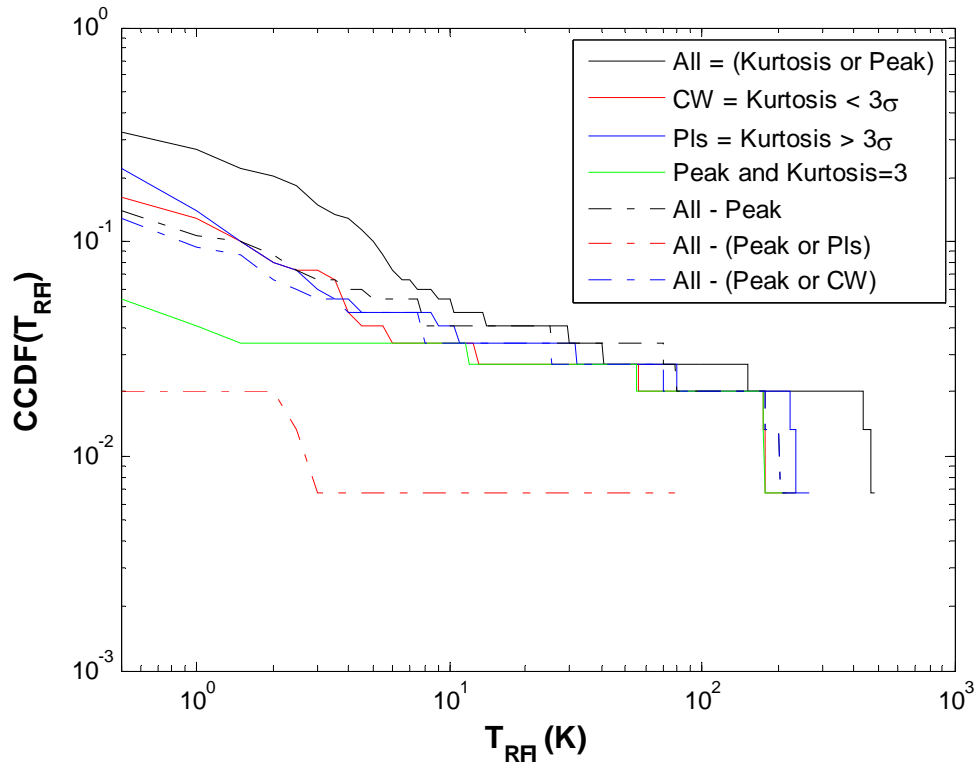


Fig. I.6: CCDF of detected and residual types of RFI brightness temperature contribution for a 11 min integration period

#### I.4 Conclusion

The extent and properties of RFI are characterized using flight campaign measurements made using ADD with JPL’s PALS instrument. Results indicate the presence of significant amounts of RFI, with approximately 2 to 3% of all detected RFI above a 100K threshold. Radar-like pulsed type RFI is more frequent than continuous wave RFI, although both types of RFI show significant brightness temperature contributions above 100K. Blind/false RFI is also present, but is very infrequent (less than 2% over 30sec integration time). The performance of the peak detection algorithm is also analyzed by observing residual RFI. Residual RFI is obtained by measuring mitigation differences between the peak detection algorithm and the “ground-truth” (obtained by combining

kurtosis and peak detection algorithms). The RFI remaining after application of the peak detection algorithm represents RFI missed by the baseline detection algorithm used for Aquarius. Results indicate that, while the peak detection algorithm detects most of the RFI, it still misses a significant portion of low-level RFI and some percentage of high level RFI (at and above the 100K level).

## **Appendix II**

### **Detectability of Radio Frequency Interference due to Spread Spectrum Communication Signals using the Kurtosis Algorithm**

#### **II.1 Introduction**

The performance of the detection algorithm has been characterized for RFI sources that have radar-like pulsed sinusoid properties [31]. The source of this RFI is primarily air-traffic control radars and early warning defense radars that operate near the L-Band region. As demonstrated in [31] the kurtosis algorithm has high sensitivity to pulsed-sinusoid RFI in most practical cases.

The performance of the detection algorithm for another major source of RFI, wide-band communication signals is discussed here. This type of RFI is expected to be dominant at urban centers. Specifically, spread-spectrum signals are becoming ubiquitous with the growing popularity of wireless technology. Low power RF devices with a long battery life using spread spectrum communications are becoming commonplace for applications such as Wireless Personal Area Network (WPAN) and identifying chips (RFID). Spread spectrum signals have noise-like spectral properties and would be difficult to detect using conventional threshold detection techniques.

In order to generate the spread-spectrum signals a commercial RF communication module based on the IEEE 802.15.4 standard called XBee is used. To evaluate its effect on a typical radiometer operation the signal is demodulated and coupled into a bench-top radiometer before feeding it into the Agile Digital Detector (ADD) used for measuring the histogram of the incoming signal [32]. ADD divides the incoming signal into eight frequency sub-bands to improve RFI detectability.

By varying the power level of the incoming RFI signal, it is found that the kurtosis algorithm is able to detect the presence of spread spectrum signals with a relatively high sensitivity. Analysis of the histogram of the spread spectrum signal suggests that, even though spread spectrum modems have noise-like power spectra, the probability distribution of their radiated amplitude is not the same as that of thermal noise. The kurtosis algorithm can reliably detect a single source of low-level spread spectrum RFI that is approximately three times the noise floor of the radiometer. This sensitivity threshold is less than that for low duty-cycle radar-like pulsed sinusoidal RFI signals.

The performance of the detection algorithm for pulsed sinusoidal RFI is summarized in Section II.2. Section II.3 describes the hardware setup used for the experiment and Section II.4 presents the results obtained by injecting spread-spectrum RFI into a radiometer noise signal.

## **II.2 Pulsed-sinusoidal RFI and Kurtosis**

The pulsed sinusoid is considered to be the typical type of RFI and kurtosis performance has been characterized with respect to such an interfering source [31, 44].

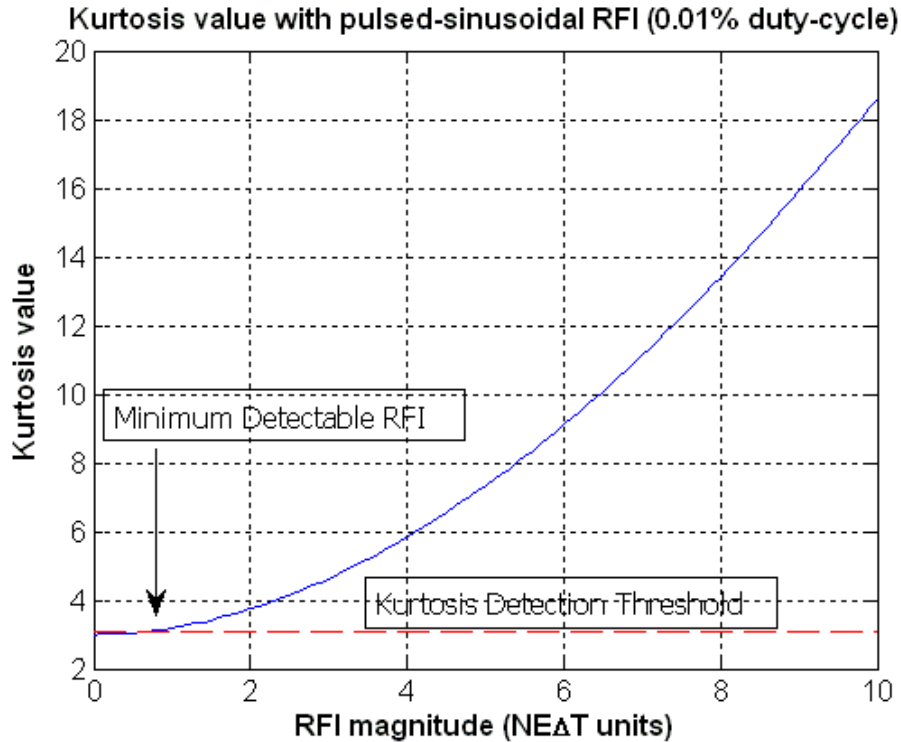


Fig. II.1: Plot indicating change in kurtosis as a function of the RFI magnitude for pulsed-sinusoid interference with a 0.01% duty cycle. The dashed line indicates the kurtosis  $3\sigma$  detection threshold

For pulsed sinusoids, the performance of the kurtosis algorithm depends on its duty cycle and amplitude. The kurtosis is below three if the incoming RFI is a continuous-wave (CW) signal and above three if the duty cycle is below 50%. The algorithm is extremely sensitive to RFI with a low duty cycle, and it has a blind-spot for sinusoids with a 50% duty cycle. Since radars typically operate at very low duty cycles, the kurtosis can detect low-level RFI near the NEAT level. Fig. II.1 indicates the minimum detectable RFI for a duty cycle of 0.01% and kurtosis threshold of three times the kurtosis standard deviation. As shown in Fig. II.1, the kurtosis algorithm can detect RFI with power levels as low as the NEAT level.

### II.3 XBee and ADD Hardware Setup

XBee is a commercial product developed for creating wireless networks with lower data rate, simple connectivity and battery operation in mind [86]. XBee operates using the IEEE 802.15.4 standard for wireless communication. We operate the XBee transceiver module in the 2.400-2.4835GHz range. The frequency scheme is shown in Fig. II.2. The device has 16 channels that are approximately 5MHz wide. It operates using the Direct Sequence Spread Spectrum (DSSS) technology using Offset Quadrature Phase-Shift Keying (O-QPSK).

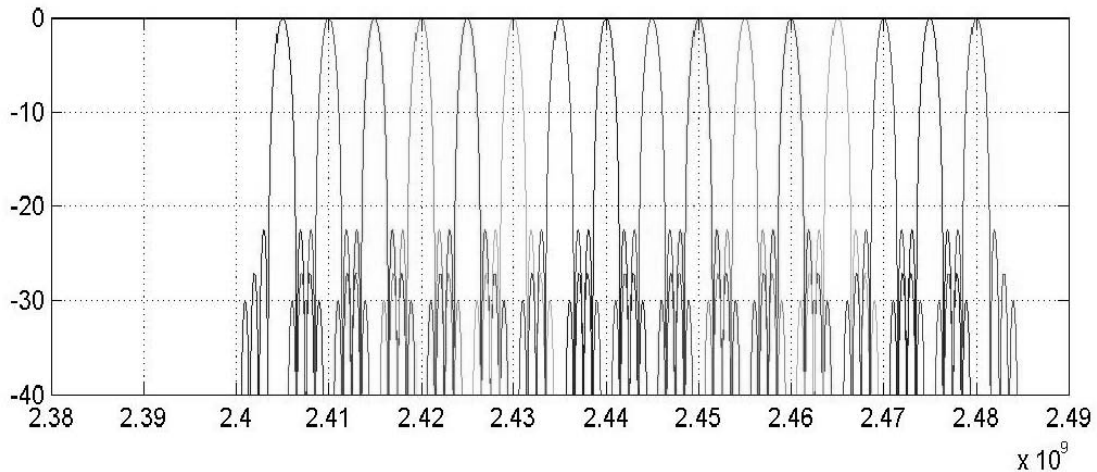


Fig. II.2: Frequency scheme of IEEE 802.15.4 communication standard [86]

The device is configured to operate at 2.410GHz. The signal from XBee is split, with half of it coupled into the demodulator and radiometer and the other half coupled to an antenna that transmits and receives data from another XBee transceiver in loop-back mode.

The output from XBee is demodulated down to a frequency near 25.5MHz and fed into ADD. ADD then digitizes the incoming signal at 110 MSa/sec before sending it to a bank of eight sub-band poly-phase filters that operate from over 15 to 39 MHz, with each sub-band 3MHz wide. The output of each sub-band is processed by totalizers that calculate the discrete pdf of the incoming signal every 36ms. The resulting XBee signal falls in sub-band 4, and it can be further swept between 15 to 39MHz by varying the LO frequency of the demodulator before ADD.

#### **II.4 Spread-Spectrum RFI and Kurtosis**

Spread-spectrum signals are generally below the noise threshold of a receiver and have noise-like qualities due to their low SNR. Analysis of the discrete pdf obtained from ADD indicates a non-normal probability distribution of spread spectrum signals. Fig. II.3 indicates the normalized histograms of clean 36ms period data and two 36ms period data corrupted with spread-spectrum RFI. The pdf of spread-spectrum RFI corrupted signals is generally wider at the base than clean data samples. Higher powered RFI have “bumps” at the outliers giving rise to a high kurtosis value. In this sense, the spread-spectrum RFI corrupted histogram is similar to those of pulsed-sinusoid RFI corrupted Gaussian noise.

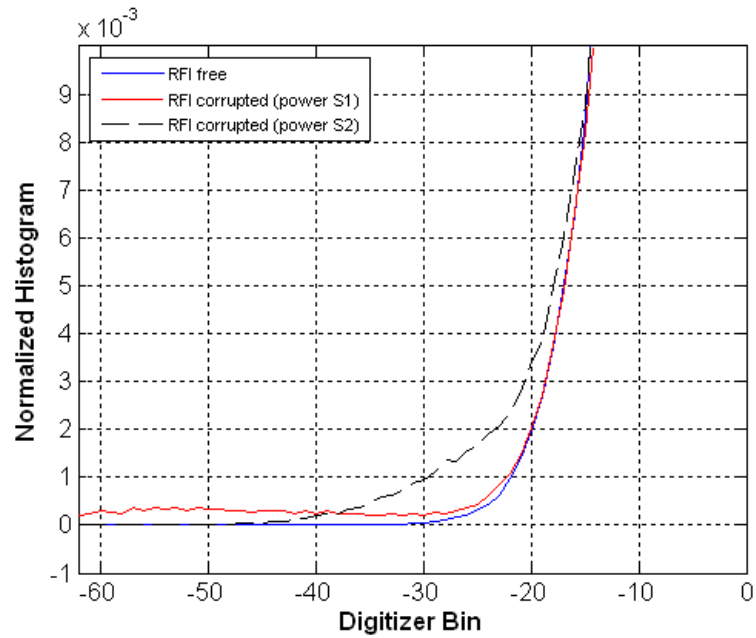
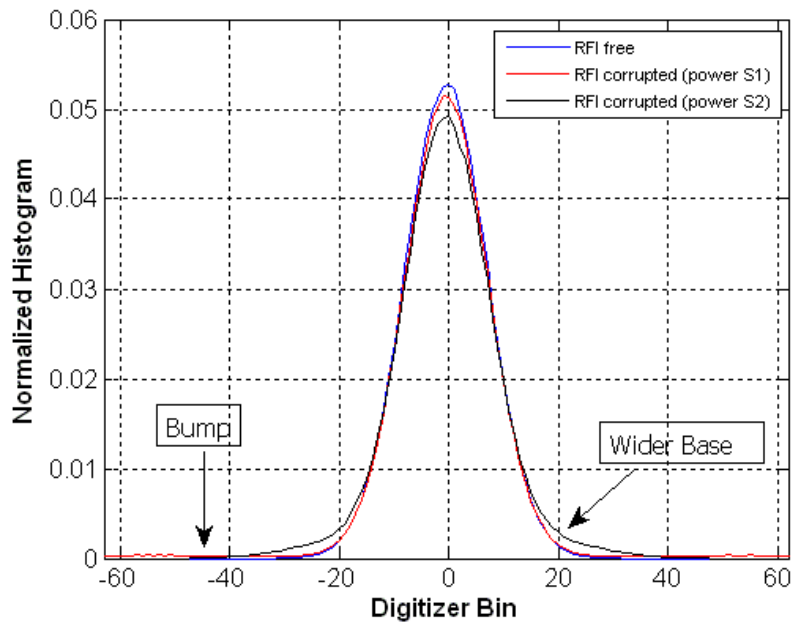


Fig. II.3: (a) Normalized histogram of the signal received by ADD for a clean sample (solid line), RFI corrupted sample with power S1 (dash-cross) and RFI corrupted sample with power S2(dashed) ( $S1 > S2$ )  
 (b) Histogram tail (zoomed) showing “bump” of RFI corrupted sample

The kurtosis also seems to perform well for lower-level RFI signals near the NE $\Delta$ T value. Fig. II.4 indicates the deviation of the kurtosis value with respect to RFI power in terms of NE $\Delta$ T units. The kurtosis has a monotonic dependence on the power of the spread spectrum signal. The dashed line in the figure indicates the kurtosis threshold similar to Fig. II.1. The kurtosis algorithm manages to detect RFI as low as 5 to 6 times the NE $\Delta$ T level.

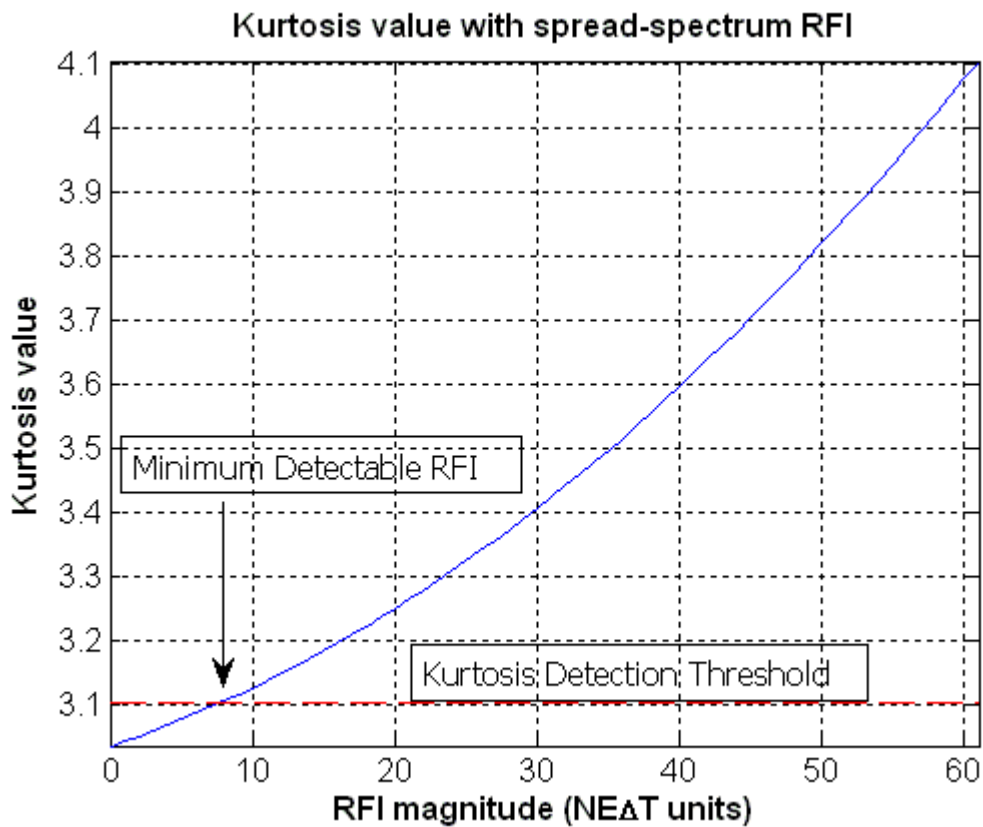


Fig. II.4: Plot indicating change in kurtosis as a function of the RFI magnitude for spread spectrum interference. The dashed line indicates the kurtosis  $3\sigma$  detection threshold

The above results are presented when the spread spectrum signal is centered in one of the sub-bands of ADD. Since the bandwidth of the signal is 5MHz and the sub-bands are

3MHz wide, a majority of the signal spectrum is within one sub-band. Fig. II.5 indicates kurtosis values when the signal spectrum is swept across the frequency sub-bands by changing the LO of the demodulator. As a result, the spectrum is divided amongst adjacent sub-bands. Kurtosis values are higher when the spectrum is offset within a sub-band compared to when the spectrum is centered for the same RFI power values. Detectability thus improves when the power spectrum of the RFI becomes less uniform.

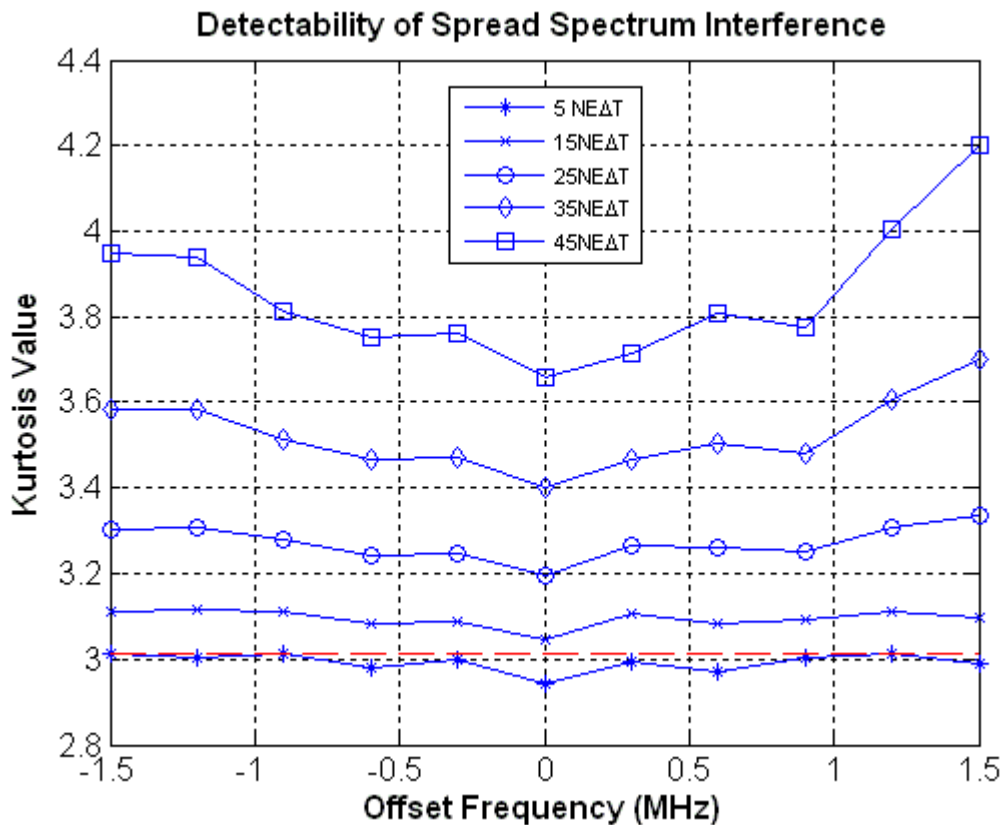


Fig. II.5: Kurtosis values when the spread spectrum signal is offset in frequency from the center of sub-band 4 of ADD. The straight line represents the kurtosis detection threshold

The solid line in Fig. II.5 indicates the detection threshold of the kurtosis algorithm. The signal is swept from -1.5MHz to +1.5MHz with respect to the original local oscillator frequency. At 0 MHz, the signal is centered in sub-band 4, at +/-1.5MHz the spread-spectrum signal is evenly divided between sub-bands 4/5 and 3/4, respectively.

## II.5 Conclusion and Discussion

RFI mitigation performance of the kurtosis detection algorithm has been previously analyzed for pulsed-sinusoidal radar-like RFI. In this paper we present results from a laboratory experiment investigating the detectability of wide-band spread-spectrum communication signals.

In order to generate such RFI signals a commercial product XBee was used that implements a popular protocol suite for WPANs. The XBee signal was coupled into a bench-top radiometer that demodulates the signal down from 2.4GHz to nearly 25.5MHz before it is fed into ADD. ADD is responsible for spectrally dividing the incoming signal and measuring the discrete pdfs, which are then used to calculate the kurtosis.

The discrete pdf obtained from ADD suggests that even though spread-spectrum signals have noise-like spectral properties, the probability distribution is non-Gaussian. This makes it possible to detect using the kurtosis algorithm. The algorithm can detect RFI at power levels near the NEAT level. The algorithm is somewhat less sensitive to spread-spectrum RFI compared to low duty-cycle radar-like RFI. Results indicate that the kurtosis was higher as the signal was swept across ADD sub-bands. This suggests that the kurtosis sensitivity increases as the wide-band or “spreading” properties of the signal decrease.

## References

- [1] M. Planck and M. Masius, *The theory of heat radiation*. Philadelphia: P. Blakiston's Son & Co., 1914.
- [2] G. Kirchoff, "Ueber den zusammenhang von emission und absorption von licht und warme," *Monatsberichte der Akademie der Wissenschaften zu Berlin*, vol. 1859, pp. 783-787, 1860.
- [3] J. E. Harries, "The greenhouse Earth: A view from space," *Quarterly journal of the Royal Meteorological Society*, vol. 122, pp. 799-799, 1996.
- [4] K. N. Liou, *An Introduction to Atmospheric Radiation*, 1980.
- [5] Rayleigh, "Dynamical theory of gases and radiation," *Nature, New biology*, vol. 72, pp. 54-56, 1905.
- [6] J. Jeans, "Partition of energy between matter and ether," *The Philosophical magazine*, vol. 10, pp. 91-98, 1905.
- [7] F. T. Ulaby, R. K. Moore, and A. K. Fung, *Microwave Remote Sensing: Active and Passive* vol. 1, 1981.
- [8] J. D. Kraus, M. E. Tiuri, and A. V. Raisanen, *Radio Astronomy*. Powell, Ohio: Cygnus-Quasar Books, 1986.
- [9] S. J. Keihm, M. A. Janssen, and C. S. Ruf, "TOPEX/Poseidon microwave radiometer (TMR). III. Wet troposphere range correction algorithm and pre-launch error budget," *Geoscience and Remote Sensing, IEEE Transactions on*, vol. 33, pp. 147-161, 1995.
- [10] T. J. Jackson, "Measuring Surface Soil-Moisture Using Passive Microwave Remote-Sensing .3.," *Hydrological Processes*, vol. 7, pp. 139-152, Apr-Jun 1993.
- [11] L. Klein and C. Swift, "An improved model for the dielectric constant of sea water at microwave frequencies," *Antennas and Propagation, IEEE Transactions on*, vol. 25, pp. 104-111, 1977.
- [12] H. J. C. Blume, B. M. Kendall, and J. C. Fedors, "Measurement of ocean temperature and salinity via microwave radiometry," *Boundary-Layer Meteorology*, vol. 13, pp. 295-308, 1978.
- [13] T. T. Wilheit, A. T. C. Chang, M. S. V. Rao, E. B. Rodgers, and J. S. Theon, "A satellite technique for quantitatively mapping rainfall rates over the oceans," *Journal of applied meteorology*, vol. 16, pp. 551-60, 1977.
- [14] T. Wilheit and M. G. Fowler, "Microwave radiometric determination of wind speed at the surface of the ocean during BESEX," *IEEE journal of oceanic engineering*, vol. 2, pp. 111-20, 1977.
- [15] D. M. Le Vine, G. S. E. Lagerloef, and S. E. Torrusio, "Aquarius and Remote Sensing of Sea Surface Salinity from Space," *Proceedings of the IEEE*, vol. 98, pp. 688-703, 2010.

- [16] S. H. Yueh, R. West, W. J. Wilson, F. K. Li, E. G. Njoku, and Y. Rahmat-Samii, "Error sources and feasibility for microwave remote sensing of ocean surface salinity," *Geoscience and Remote Sensing, IEEE Transactions on*, vol. 39, pp. 1049-1060, 2001.
- [17] W. H. Peake, "Interaction of electromagnetic waves with some natural surfaces," *IRE Transactions on Antennas propagation*, vol. 7, pp. S324-S329, 1959.
- [18] R. Barakat, "Some fluctuation problems associated with blackbody radiation," *Journal of the Optical Society of America*, vol. 56, pp. 1244-1247, 1966.
- [19] L. Mandel and E. Wolf, "Coherence properties of optical fields," *Reviews of modern physics*, vol. 37, pp. 231-287, 1965.
- [20] L. Jánossy, "On the classical fluctuation of a beam of light," *Il Nuovo Cimento (1855-1965)*, vol. 6, pp. 111-124, 1957.
- [21] M. v. Laue, "Fourier coefficients of natural radiation," *Annalen der Physik*, vol. 48, pp. 668-680, 1915.
- [22] M. v. Laue, "Probability theorem and radiation," *Annalen der Physik*, vol. 47, pp. 853-878, 1915.
- [23] A. Einstein, "Probability theorem and radiation," *Annalen der Physik*, vol. 47, pp. 879-885, 1915.
- [24] S. Varró, "Irreducible decomposition of Gaussian distributions and the spectrum of black-body radiation," *Physica scripta*, vol. 75, pp. 160-9, 2007.
- [25] M. G. Kendall, A. Stuart, J. K. Ord, S. F. Arnold, and A. O'Hagan, *Kendall's advanced theory of statistics*, 6th ed. London: Halsted Press, 1994.
- [26] N. Skou and D. M. Le Vine, *Microwave radiometer systems: design and analysis*: Artech House, Inc., 2006.
- [27] S. Weinreb, "Digital radiometer," *Proceedings of the Institute of Radio Engineers*, vol. 49, pp. 1099-1099, 1961.
- [28] M. A. Fischman and A. W. England, "Sensitivity of a 1.4 GHz direct-sampling digital radiometer," *Geoscience and Remote Sensing, IEEE Transactions on*, vol. 37, pp. 2172-2180, 1999.
- [29] M. A. Fischman and A. W. England, "An L-band direct sampling digital radiometer for STAR technology sensors," *2000 IEEE Aerospace Conference Proceedings*, vol. 5, pp. 129-39, 2000.
- [30] C. Ruf and S. Gross, "Digital radiometers for earth science," in *Microwave Symposium Digest (MTT), IEEE MTT-S International*, 2010, pp. 828-831.
- [31] R. D. De Roo, S. Misra, and C. S. Ruf, "Sensitivity of the kurtosis statistic as a detector of pulsed sinusoidal RFI," *Geoscience and Remote Sensing, IEEE transactions on*, vol. 45, pp. 1938-46, 2007.
- [32] C. S. Ruf, S. M. Gross, and S. Misra, "RFI detection and mitigation for microwave radiometry with an agile digital detector," *Geoscience and Remote Sensing, IEEE Transactions on*, vol. 44, pp. 694-706, 2006.
- [33] L. Li, E. G. Njoku, E. Im, P. S. Chang, and K. S. Germain, "A preliminary survey of radio-frequency interference over the U.S. in Aqua AMSR-E data," *Geoscience and Remote Sensing, IEEE Transactions on*, vol. 42, pp. 380-390, 2004.
- [34] E. G. Njoku, P. Ashcroft, T. K. Chan, and L. Li, "Global survey and statistics of radio-frequency interference in AMSR-E land observations," *Geoscience and Remote Sensing, IEEE Transactions on*, vol. 43, pp. 938-947, 2005.

- [35] L. Li, P. W. Gaiser, M. H. Bettenhausen, and W. Johnston, "WindSat radio-frequency interference signature and its identification over land and ocean," *Geoscience and Remote Sensing, IEEE Transactions on*, vol. 44, pp. 530-539, 2006.
- [36] S. W. Ellingson and J. T. Johnson, "A polarimetric survey of radio-frequency interference in C- and X-bands in the continental united states using WindSat radiometry," *Geoscience and Remote Sensing, IEEE Transactions on*, vol. 44, pp. 540-548, 2006.
- [37] E. G. Njoku, T. K. Chan, W. Crosson, and A. Limaye, "Evaluation of the AMSR-E data calibration over land," *Italian Journal of Remote Sensing*, vol. 30, pp. 15-33, 2004.
- [38] J. E. Balling, S. S. Sobjaerg, S. S. Kristensen, and N. Skou, "RFI and SMOS: Preparatory campaigns and first observations from space," *2010 11th Specialist Meeting on Microwave Radiometry and Remote Sensing of the Environment*, pp. 282-287, 2010.
- [39] D. M. Le Vine and M. Haken, "RFI at L-band in synthetic aperture radiometers," in *IEEE International Geoscience and Remote Sensing Symposium (IGARSS), Proceedings*, Toulouse, France, 2003, pp. 1742-1744.
- [40] D. M. Le Vine, "ESTAR experience with RFI at L-band and implications for future passive microwave remote sensing from space," in *IEEE International Geoscience and Remote Sensing Symposium (IGARSS), Proceedings 2002*, pp. 847-849 vol.2.
- [41] N. Skou, S. Misra, J. E. Balling, S. S. Kristensen, and S. S. Sobjaerg, "L-Band RFI as Experienced During Airborne Campaigns in Preparation for SMOS," *Geoscience and Remote Sensing, IEEE Transactions on*, vol. 48, pp. 1398-1407, 2010.
- [42] M. Younis, J. Maurer, J. Fortuny-Guasch, R. Schneider, W. Wiesbeck, and A. J. Gasiewski, "Interference from 24-GHz automotive radars to passive microwave earth remote sensing satellites," *Geoscience and Remote Sensing, IEEE Transactions on*, vol. 42, pp. 1387-1398, 2004.
- [43] S. Curry, M. Ahlers, H. Elliot, S. Gross, D. McKague, S. Misra, J. Puckett, and C. Ruf, "K-Band Radio frequency Interference Survey of Southeastern Michigan," in *IEEE International Geoscience and Remote Sensing Symposium (IGARSS), Proceedings*, 2010, pp. 2486-2489.
- [44] J. Piepmeier and F. Pellerano, "Mitigation of Terrestrial Radar Interference in L-Band Spaceborne Microwave Radiometers," in *IEEE International Geoscience and Remote Sensing Symposium (IGARSS), Proceedings*, 2006, pp. 2292-2296.
- [45] J. T. Johnson and L. C. Potter, "Performance Study of Algorithms for Detecting Pulsed Sinusoidal Interference in Microwave Radiometry," *Geoscience and Remote Sensing, IEEE Transactions on*, vol. 47, pp. 628-636, 2009.
- [46] S. Misra, C. Ruf, and R. Kroodsma, "Detectability of Radio Frequency Interference due to Spread Spectrum Communication Signals using the Kurtosis Algorithm," in *IEEE International Geoscience and Remote Sensing Symposium (IGARSS), Proceedings*, 2008, pp. II-335-II-338.
- [47] "Interference Criteria for Satellite Passive Remote Sensing," International Telecommunications Union, Geneva, Switzerland, ITU-R RS.1029-2, 2003.
- [48] A. J. Gasiewski, M. Klein, A. Yevgrafov, and V. Leuskiy, "Interference mitigation in passive microwave radiometry," in *IEEE International Geoscience and Remote Sensing Symposium (IGARSS), Proceedings*, 2002, pp. 1682-1684 vol.3.
- [49] J. T. Johnson, G. A. Hampson, and S. W. Ellingson, "Design and demonstration of an interference suppressing microwave radiometer," in *IEEE International Geoscience and Remote Sensing Symposium (IGARSS), Proceedings*, 2004, pp. 1683-1686 vol.3.

- [50] B. Guner, J. T. Johnson, and N. Niamsuwan, "Time and Frequency Blanking for Radio-Frequency Interference Mitigation in Microwave Radiometry," *Geoscience and Remote Sensing, IEEE Transactions on*, vol. 45, pp. 3672-3679, 2007.
- [51] B. Guner, N. Niamsuwan, and J. T. Johnson, "Performance study of a cross-frequency detection algorithm for pulsed sinusoidal RFI in microwave radiometry," *Geoscience and Remote Sensing, IEEE Transactions on*, vol. 48, pp. 2899-2908, 2010.
- [52] J. R. Piepmeier, P. N. Mohammed, and J. J. Knuble, "A Double Detector for RFI Mitigation in Microwave Radiometers," *Geoscience and Remote Sensing, IEEE Transactions on*, vol. 46, pp. 458-465, 2008.
- [53] R. D. De Roo and S. Misra, "Effectiveness of the Sixth Moment to Eliminate a Kurtosis Blind Spot in the Detection of Interference in a Radiometer," in *IEEE International Geoscience and Remote Sensing Symposium (IGARSS), Proceedings*, 2008, pp. II-331-II-334.
- [54] R. D. De Roo and S. Misra, "A Moment Ratio RFI Detection Algorithm That Can Detect Pulsed Sinusoids of Any Duty Cycle," *Geoscience and Remote Sensing Letters, IEEE*, vol. 7, pp. 606-610, 2010.
- [55] S. Misra, C. Ruf, and R. D. Roo, "Agile Digital Detector for RFI Mitigation," in *IEEE MicroRad, 2006*, 2006, pp. 66-69.
- [56] J. Park, J. T. Johnson, N. Majurec, N. Niamsuwan, J. R. Piepmeier, P. N. Mohammed, C. S. Ruf, S. Misra, S. H. Yueh, and S. J. Dinardo, "Airborne L-Band Radio Frequency Interference Observations From the SMAPVEX08 Campaign and Associated Flights," *Geoscience and Remote Sensing, IEEE Transactions on*, vol. PP, pp. 1-12, 2011.
- [57] N. Skou, J. E. Balling, S. S. Sobjarg, and S. S. Kristensen, "Surveys and analysis of RFI in the SMOS context," in *IEEE Geoscience and Remote Sensing Symposium (IGARSS), Proceedings*, 2010, pp. 2011-2014.
- [58] D. M. Le Vine, G. S. E. Lagerloef, F. R. Colomb, S. H. Yueh, and F. A. Pellerano, "Aquarius: An Instrument to Monitor Sea Surface Salinity From Space," *Geoscience and Remote Sensing, IEEE Transactions on*, vol. 45, pp. 2040-2050, 2007.
- [59] S. Misra, S. S. Kristensen, S. S. Sobjaerg, and N. Skou, "CoSMOS: Performance of kurtosis algorithm for radio frequency interference detection and mitigation," in *IEEE International Geoscience and Remote Sensing Symposium (IGARSS), Proceedings*, 2007, pp. 2714-2717.
- [60] Niamsuwan, "Examination of a simple pulse blanking technique for radio frequency interference mitigation," *Radio science*, vol. 40, p. RS5S03, 2005.
- [61] C. Ruf, S. Misra, S. Gross, and R. De Roo, "Detection of RFI by its Amplitude Probability Distribution," in *IEEE International Geoscience and Remote Sensing Symposium (IGARSS), Proceedings*, 2006, pp. 2289-2291.
- [62] W. J. Wilson, S. H. Yueh, S. J. Dinardo, S. L. Chazanoff, A. Kitiyakara, F. K. Li, and Y. Rahmat-Samii, "Passive active L- and S-band (PALS) microwave sensor for ocean salinity and soil moisture measurements," *Geoscience and Remote Sensing, IEEE Transactions on*, vol. 39, pp. 1039-1048, 2001.
- [63] Y. H. Kerr, P. Waldteufel, J. P. Wigneron, J. Martinuzzi, J. Font, and M. Berger, "Soil moisture retrieval from space: the Soil Moisture and Ocean Salinity (SMOS) mission," *Geoscience and Remote Sensing, IEEE Transactions on*, vol. 39, pp. 1729-1735, 2001.

- [64] S. Misra and C. S. Ruf, "Detection of Radio-Frequency Interference for the Aquarius Radiometer," *Geoscience and Remote Sensing, IEEE Transactions on*, vol. 46, pp. 3123-3128, 2008.
- [65] J. F. Kenney and E. S. Keeping, *Mathematics of statistics*, 3d ed. New York,: Van Nostrand company, 1954.
- [66] R. D. De Roo and S. Misra, "A Demonstration of the Effects of Digitization on the Calculation of Kurtosis for the Detection of RFI in Microwave Radiometry," *Geoscience and Remote Sensing, IEEE Transactions on*, vol. 46, pp. 3129-3136, 2008.
- [67] G. A. Hampson, S. W. Ellingson, and J. T. Johnson, "Design and demonstration of an interference suppressing microwave radiometer," in *IEEE Aerospace Conference, Proceedings*, 2004, pp. 993-999.
- [68] N. Niamsuwan, B. Guner, and J. Johnson, "Observations of an ARSR System in Canton, MI with the L-band Interference Suppressing Radiometer," in *IEEE International Geoscience and Remote Sensing Symposium (IGARSS), Proceedings*, 2006, pp. 2285-2288.
- [69] S. Misra, P. N. Mohammed, B. Guner, C. S. Ruf, J. R. Piepmeier, and J. T. Johnson, "Microwave radiometer radio-frequency interference detection algorithms: A comparative study," *Geoscience and Remote Sensing, IEEE transactions on*, vol. 47, pp. 3742-3754, 2009.
- [70] S. Misra and C. Ruf, "Inversion algorithm for estimating radio frequency interference characteristics based on kurtosis measurements," in *IEEE International Geoscience and Remote Sensing Symposium (IGARSS), Proceedings*, 2009, pp. II-162-II-165.
- [71] S. O. Rice, "Statistical Properties of a Sine Wave Plus Random Noise," *Bell System Technical Journal*, vol. 27, pp. 109-157, 1948.
- [72] Y. H. Kerr, P. Waldteufel, J. P. Wigneron, S. Delwart, F. Cabot, J. Boutin, M. J. Escorihuela, J. Font, N. Reul, C. Gruhier, S. E. Juglea, M. R. Drinkwater, A. Hahne, M. Martin-Neira, and S. Mecklenburg, "The SMOS Mission: New Tool for Monitoring Key Elements of the Global Water Cycle," *Proceedings of the IEEE*, vol. 98, pp. 666-687, 2010.
- [73] A. Camps, J. Gourrion, J. M. Tarongi, A. Gutierrez, J. Barbosa, and R. Castro, "RFI analysis in SMOS imagery," in *IEEE International Geoscience and Remote Sensing Symposium (IGARSS), Proceedings*, 2010, pp. 2007-2010.
- [74] H. M. J. Barre, B. Duesmann, and Y. H. Kerr, "SMOS: The Mission and the System," *Geoscience and Remote Sensing, IEEE Transactions on*, vol. 46, pp. 587-593, 2008.
- [75] E. Anterrieu, *Personal Communication*, 2010.
- [76] ESA, "SMOS Calibration Validation and Retrieval Plan," April 2010.
- [77] A. Camps, I. Corbella, M. Vall-llossera, N. Duffo, F. Marcos, F. Martinez-Fadrique, and M. Greiner, "The SMOS end-to-end performance simulator: description and scientific applications," in *IEEE International Geoscience and Remote Sensing Symposium (IGARSS), Proceedings*, 2003, pp. 13-15 vol.1.
- [78] H. T. Friis, "A note on a simple transmission formula," *Proceedings of the IRE*, vol. 34, p. 254, 1946.
- [79] K. Huang and S. Aviyente, "Sparse representation for signal classification," *Advances in Neural Information Processing Systems*, 2006.
- [80] M. A. Brown, F. Torres, I. Corbella, and A. Colliander, "SMOS Calibration," *Geoscience and Remote Sensing, IEEE Transactions on*, vol. 46, pp. 646-658, 2008.

- [81] J. Yang and S. Roy, "Joint transmitter-receiver optimization for multi-input multi-output systems with decision feedback," *Information Theory, IEEE Transactions on*, vol. 40, pp. 1334-1347, 1994.
- [82] C. Ruf and S. Misra, "Detection of Radio Frequency Interference with the Aquarius Radiometer," in *IEEE International Geoscience and Remote Sensing Symposium (IGARSS), Proceedings*, 2007, pp. 2722-2725.
- [83] S. Misra and C. Ruf, "Comparison of Pulsed Sinusoid Radio Frequency Interference Detection Algorithms Using Time and Frequency Sub-Sampling," in *IEEE International Geoscience and Remote Sensing Symposium (IGARSS), Proceedings*, 2008, pp. II-153-II-156.
- [84] S. Misra, R. De Roo, and C. Ruf, "Evaluation of the kurtosis algorithm in detecting radio frequency interference from multiple sources," in *IEEE International Geoscience and Remote Sensing Symposium (IGARSS), Proceedings*, 2010, pp. 2019-2022.
- [85] J. H. Van Vleck and D. Middleton, "The spectrum of clipped noise," *Proceedings of the IEEE*, vol. 54, pp. 2-19, 1966.
- [86] "Demystifying 802.15.4 and ZigBee," MaxStream Inc.2006.